MODELING OF INTEGRATED MICROFLUIDICS-CMOS LAB-ON-CHIP TECHNOLOGY

by

Saul Caverhill-Godkewitsch

A thesis submitted to the Faculty of Graduate Studies and Research

in partial fulfillment of the requirements for the degree of

Master of Science

in

Biomedical Engineering

Department of Electrical and Computer Engineering

University of Alberta

ABSTRACT

The infrastructure necessary to support diagnostic and pathogen-detection processes does not exist in some regions of the world that need it most. Access to fast, inexpensive and portable diagnostic infrastructure could be a solution to this problem.

Next generation lab-on-chip (LOC) systems that integrate polymer microfluidics with CMOS circuit instrumentation can replace the need for costly and immobile conventional diagnostic laboratories. Portable DNA-based tests require three components: sample preparation (SP), amplification and detection. Finite element analysis allows for complicated engineering designs to be modeled to determine real-world behaviour, allowing key parameters to be explored prior to fabrication, saving time and money during prototyping.

The BioMEMS project group at the University of Alberta has been working on a series of integrated polymer microfluidic-CMOS platforms or "chips" as such LOC systems. Amplification is performed via the polymerase chain reaction (PCR) in our LOC platform. Significant updates to the SP and PCR modules of the three-step diagnostic process were required for the latest revision of the chip. By leveraging the power of Finite Element Analysis (FEA) modeling, an SP module capable of processing a 1 µL sample in minutes was designed and built. Similarly, PCR heaters were designed that generate $\pm 0.5\,^{\circ}\mathrm{C}$ uniformity at a target temperature of $95\,^{\circ}\mathrm{C}$ in the reaction chamber volume while enabling a 3-step PCR protocol of 35 cycles (4.19 seconds per cycle) in under two and a half minutes. These achievements are a step towards altering the current state of inaccessible point of care (POC) diagnostics.

ACKNOWLEDGEMENTS

First I must sincerely thank my supervisors Dr. Duncan Elliott, Dr. Chris Backhouse, and Dr. Dan Sameoto. Dr. Backhouse, thank you for accepting me into your research group and for motivating me from the get-go - you have a way with generating excitement in your students that is truly admirable.

Dr. Elliott, thank you for taking me on and finding common ground for research when Dr. Backhouse's path led him to the University of Waterloo. Your no-nonsense feedback, patience and adherence to good engineering habits have been priceless in my development.

Dr. Sameoto, thank you for lending your expertise and for providing constant reminders of practicality. Your hands-on approach, swift action on your to-do lists and unwavering energy demonstrated commitment to your students in a way that was immensely appreciated.

A special thank-you goes to my committee members Dr. Stevan Dubljevic and Dr. Venkata Dinavahi who graciously accepted a mid-summer defense date when they so easily could have declined. Thanks also to the staff at the ECE department and machine shop, and the NanoFab.

For providing daily comradery, technical support and some laughs along the way, heartfelt thanks are due to my collaborators and lab-mates: Andrew Hakman, John Koob, Russell Dodd, Ben Martin, Karl Jensen, Graham Banting, Eva Sant, Ayokunle Olanrewaju, Samira Movahedian, Shane Groendahl and Mohammad Behnam. Special thanks to Matthew Reynolds for fabricating the thermal devices in this thesis, Abdul Wasay for performing sample preparation experiments, David Sloan for offering technical insight and CMOS expertise, and Jose Martinez-Quijada for teaching me about thermal systems and working hand-in-hand with me on the thermal models that make up a portion of this thesis.

Thanks to all my funding partners, including the University of Alberta, Alberta Innovates Technology Futures, NSERC, Teledyne DALSA Semiconductor Inc. and CMC Microsystems.

Last, and certainly not least, *thank you* to my family and all of my friends. Your support in the good times and the bad has simply meant the world to me.

CONTENTS

LIST OF TABLES

LIST OF FIGURES

LIST OF ABBREVIATIONS

LOF	List of Figures
LOT	List of Tables
LOC	Lab on Chip
POC	Point of Care
CMOS	Complementary Metal-Oxide Semiconductor
FEA	Finite Element Analysis
FEM	Finite Element Modeling
SP	Sample Preparation
PCR	Polymerase Chain Reaction
CE	Capillary Electrophoresis
MCA	Melting Curve Analysis
RNA	Ribonucleic Acid
DNA	Deoxyribonucleic Acid
MDA	Multiple Displacement Amplification
RCA	Rolling Circle Amplification
NASBA	Nucleic Acid Sequence-Based Amplification
PMT	Photomultiplier Tube
CCD	Charge-Coupled Device
LIF	Laser Induced Fluorescence
SPE	Solid Phase Extraction
CS	Charge Switch
PCB	Printed Circuit Board

CHAPTER 1

INTRODUCTION AND MOTIVATION

The exciting research area of microfluidics and lab-on-chip (LOC) technology combines expertise in several disciplines including electrical and mechanical engineering, physics, chemistry and biology. Exploring the motivation for this field and some background context on glass and polymer microfabrication leads us into a discussion of the state of the art in microfluidic platforms, including some of their advantages, limitations, and tools for design. A brief review of LOC technology history presents the trend from glass-based microfluidics with external instrumentation to fully-integrated polymer-on-CMOS LOC devices.

1.1 The Limitations of Contemporary Diagnostics and Pathogen Detection

The cost of infrastructure, equipment and expertise to implement state of the art medical diagnostics is economically out-of-reach for many regions of the world. It is often these poverty-stricken regions, however, that are in the most dire need for such diagnostic capabilities. One specific example can highlight this issue: In 2008, malaria led to almost one million deaths world-wide. Most of the victims were children in Africa, where malaria is responsible for 20% of all childhood deaths, despite the disease being preventable and curable [2]. Six years later, the problem remains - in 2014 there were 430000 child deaths in Africa alone [3]. Indeed, addressing this lack of accessibility to fast, inexpensive, and portable point-of-care (POC) diagnostics is an important effort of interdisciplinary engineering [4].

With a myriad of applications in diverse industries such as health care, food and water quality, chemicals and pharmaceuticals, microfluidic technology offers compelling advantages over

conventional bulk analysis systems [5–7]. The minuscule volumes (μL down to nL) required by miniaturized fluidic systems lead to reductions in analysis time and reagent volumes while improving the limits of detection. High instrument costs are avoided, and the small volumes associated with microfluidics reduce reagent costs per test.

Lab-on-chip systems are being developed to replace the need for costly and immobile medical infrastructure by integrating several conventional laboratory functions into inexpensive, portable and user-friendly platforms. By exploiting recent advancements in microfluidic technologies and incorporating them with miniaturized methods for sample handling and detection, the LOC community is equipped to change the landscape of medical diagnostics in a fundamental way.

1.2 Lab-On-Chip Technology

As mentioned in section 1.1, LOC technologies have the potential to replace costly and immobile infrastructure by integrating the abilities of standard laboratory machines into inexpensive and portable platforms. In addition to the cost and convenience benefits of integration, gold-standard, conventional bulk-analysis systems can be improved upon significantly by making use of the technical benefits brought forward by the miniaturization of fluidic technologies [5–7]. Using only a fraction of the reagent volumes associated with bulk systems, miniaturized fluidic platforms reduce reagent cost and sample volumes. While cost is an issue in all industries, the health care perspective also strives to reduce the invasiveness of patient testing. Current diagnostic methods often require the extraction of many millilitres of blood from a patient for a single test. Microfluidic platforms could implement similar diagnostics with only a drop of blood, making them much less invasive than current diagnostic methods. Indeed, LOC technology can act as a solution to many of the major issues associated with contemporary diagnostics and pathogen detection.

1.3 Glass Microfluidic Platforms

Traditional microfluidic devices have relied on glass as the structural material for its general chemical inertness, biocompatibility and optical transparency. With such a well-characterized material, many demonstrations of integrated and semi-integrated systems have surfaced [6, 8, 9]. Despite these advancements, glass remains a difficult material to work with. Microfabrication of structural elements in glass requires the use of hydrofluoric acid - a highly corrosive and

severely poisonous substance. In addition to the danger associated with the chemicals required for microfabrication of structures in glass, the process is time consuming and expensive. Many complicated steps are required to complete the photolithography, etching and bonding needed to produce microfluidic chips in glass [10]. For a device which is, ideally, disposable, the significant effort required for glass processing can be avoided by making use of polymer fabrication techniques. Furthermore, the scaling of glass fluidic chip fabrication and production is a major challenge.

The microelectronics industry demonstrates that when small devices are fabricated in large numbers, costs are driven down considerably. These economies of scale can similarly be obtained by miniaturizing the fabrication of fluidic analysis systems to the micro scale. In order for large-scale production of integrated microfluidic devices to occur, the fabrication problems existing in traditional glass microfluidic technology must be addressed, or avoided.

1.4 Polymer Microfluidic Platforms

Glass has long been the structural material of choice in microfluidics. Despite its advantages, some groups have replaced glass with polymer substrates in their LOC demonstrations [11–13]. Improvements in fabrication methods for polymer LOC microfluidics could provide the platform necessary to demonstrate fully-integrated, low-cost and disposable diagnostic solutions. The trend of microfluidics towards polymer methods is well under-way, but several challenges still stand in the way of full-adoption of these alternative materials. Poor biocompatibility [14] and a lack of standard processing methods for polymers pose significant challenges to researchers and industry alike. It should be noted, however, that polymers exist which exhibit good biocompatibility under some conditions (such as polydimethylsiloxane (PDMS) and parylene) [15–20] and scalable manufacturing/fabrication methods. The demonstration of a process for porting existing glass-based designs to polymer methods would be a useful advancement for polymer microfabrication in general, and could yield reductions in fabrication time and cost while improving biocompatibility of microfluidic chips.

1.5 Polymer-CMOS Microfluidic Platforms

Despite the significant advances in manufacturability, biocompatibility and, ultimately, cost that polymer microfluidic platforms provide, there are still other major issues with LOC technology. The cost of external instrumentation required for operating many LOC devices is a significant barrier to widespread adoption, and contributes to the moniker "chip-in-a-lab". Indeed, integration of components is one of the most important focuses of LOC research and some fairly elegant solutions have been published that show moderate integration of fluidics and electronics [1, 6, 9, 21–25].

To truly drive the cost per test down to a number that is affordable in all regions of the world, economies of scale must be invoked. The microelectronics industry has made use of complementary metal-oxide semiconductor (CMOS) technology and its derivatives to drive component size and cost down for years.

The next generation of truly integrated LOC platforms must seamlessly integrate the fluidic and electronic parts. One option for an intimate fluidic/electronic interface is to utilize polymer-on-CMOS technology, wherein the fluidic layer is placed directly on top of passivated CMOS microelectronics.

Teledyne DALSA Semiconductor, Inc. (TDSI), an industry-leader in high-voltage CMOS and MEMS, acts as our industrial partner. TDSI has developed a microfluidics-on-CMOS process with an epoxy-based photoresist known as KMPR [26], manufactured by MicroChem Corp. Although this thesis will refer to KMPR as the working polymer, any polymer used as a functional fluidic layer on top of CMOS can be treated similarly. Canadian Microelectronics Corporation (CMC) Microsystems administers the fabrication schedule and application procedure for University research groups that wish to produce CMOS devices. The process our group utilizes is CMOSP8G/HighVoltage, which has an average prototype manufacturing turn-around time of 27 weeks. The KMPR polymer-on-CMOS cycle is less than once yearly. Because of this lengthy time scale, it is prudent to ensure that designs are as refined as possible before submitting for fabrication. It is with this motivation that finite element analysis (FEA) modeling is a great tool for producing designs that act predictably.

1.6 Finite Element Analysis

Finite element analysis is a technique for numerically approximating solutions to partial differential equations. Essentially, a geometry is split up into many small, finite pieces, each of which can be solved-for given a particular physics application. Those solutions are determined in relation to each other, and are taken together to make up the final model.

The FEA method allows for new designs to be modeled with the purpose of determining real-world behaviour. Materials, geometry, dimensions and other key quantities can all be explored to refine the design. By determining near-optimal solutions without doing any fabrication saves time and money during prototyping.

As lab-on-chip and other engineering fields continually require more and more complicated solutions, FEA will continue to grow as an important part of the design process.

1.7 Conclusions:

Introduction to LOC Technology and Motivation

After exploring the evolution of LOC technology and the motivation for doing research in this field, it is evident that the subject is moving at a rapid pace. With the importance of the FEA method established, more in-depth background of microfluidic and LOC platforms relevant to my particular areas of research (final-step sample concentration and robust thermal design) are explored in the next chapter.

CHAPTER 2

LOC BACKGROUND AND THE STATE OF THE ART

As discussed in chapter 1, the focus of the BioMEMS project is on the advancement of diagnostic and pathogen detection systems in the field of Lab-on-chip technology and microfluidic applications. Background information on the three components of molecular diagnostics (sample preparation, amplification and detection) yields perspective on the importance of doing research on two contemporary issues in LOC engineering. The two topics of sample preparation and robust thermal design are introduced, and are the focus of this work.

2.1 Lab-On-Chip Technology

The focus of the BioMEMS project has been to design LOC devices which can do nucleic acid-based diagnostics and pathogen detection [4, 6, 10, 27]. While many different methods exist for doing this procedure, three main steps are required: sample preparation, amplification and detection. Our lab has focused on one version of this three-step process from sample-to-answer. By combining three standard diagnostic functions (sample preparation (SP)), amplification (via the polymerase chain-reaction (PCR)), and detection (via capillary electrophoresis (CE) or melting curve analysis (MCA)) we can construct a miniaturized, inexpensive and truly portable diagnostic platform for genetic analysis.

2.1.1 Sample Preparation

Sample preparation is the first step in any nucleic acid-based test. In short, it is the extraction and separation of nucleic acids (includes genetic material such as ribonucleic acid (RNA) or deoxyribonucleic acid (DNA)) from a raw sample. Raw samples come in a myriad of forms, including saliva, urine, blood and tissue for diagnostics, water for water-quality testing, or various foodstuffs for food safety assays. Since sample preparation techniques are one of the focuses of this

thesis, an in-depth discussion of modern methods is included in section 3.1.

2.1.2 Amplification

The amount of genetic material in a raw sample is often too small to easily detect, so it is prudent to multiply the target sequence (or lack thereof) in order to demonstrate a reliable diagnostic answer. Various methods exist for sample amplification, such as loop-mediated isothermal amplification (LAMP) for DNA [28], or nucleic acid sequence-based amplification (NASBA) for RNA [29]. The most common method, however, is known as the polymerase chain reaction (PCR) [30]. PCR is a very efficient process for replicating a selected sequence of nucleotides on a target strand of DNA. This is the method of choice in the BioMEMS project. In short, PCR typically consists of repeating three steps:

1. Denaturation

   Reaction is heated to $\sim 95\,^{\circ}\mathrm{C}$ to "melt" the double-stranded DNA molecules into two individual strands.

2. Annealing

   Reaction is cooled to $\sim 56\,^{\circ}\mathrm{C}$ to allow primers (small pieces of DNA that match the target sequence of interest) to hybridize to the individual DNA strands.

3. Extension

   Reaction is heated back up to $\sim 72\,^{\circ}\mathrm{C}$ to encourage the polymerase enzyme to copy the DNA strands, starting from the primers which mark the location of interest. If every piece of DNA is successfully replicated during this phase, the quantity of the target DNA in the sample is doubled.

This process is repeated a number of times to ensure there is sufficient "PCR product" (the target of interest) for detection.

One of the most stunning recent demonstrations of PCR in a LOC device was developed by [1] in 2011; by making use of active cooling in addition to heating, they were able to reduce the PCR time from about an hour to just three minutes (30 cycles at 5.55 s per cycle). This is particularly striking since they were able to achieve such a short time while still using a rather large PCR volume of 5 µL. Other groups have designed complex systems that integrate PCR with the other

molecular diagnostics steps by including micro valves and pumps for manipulating fluids within a chip [6, 22, 31]. Yet another strategy was presented by [32] - discrete droplets of PCR mix (in oil to prevent evaporation) were manipulated between different temperature zones by an electrode array to accomplish the necessary thermal cycling of PCR. While many different methods exist for doing the thermal-cycling, it is clear that PCR is a mainstay of diagnostic applications in LOC devices.

2.1.3 Detection

Once the genetic analyte of interest has been sufficiently multiplied, detection of the target can begin. Various forms of optical detection make up the most common methods used for probing PCR product. In general, the analyte of interest is bound to a source of fluorescence which is detected using a photo-sensitive device such as a PMT (photomultiplier tube), CCD (charge-coupled device), or photodiode. Several groups, including ours, has achieved laser-induced fluorescence (LIF) of end-labeled PCR products on-chip [6, 33, 34]. A good review of such methods is described in [35]. In [36], an on-chip spectrometer was developed that could detect multiple emission wavelengths. Of course, LIF-type optical detection schemes often require bulky equipment and sensitive and expensive optics. Much more appropriate for the POC setting than microscopes and cameras, [37] demonstrates detection of fluorescent beads on CMOS.

2.2 BioMEMS System Chip ICKAALXX

For several years the BioMEMS project group has been developing a CMOS platform which integrates all of the necessary electronics for a LOC device into one package. This series of chips has been denoted ICKAALXX, where the XX characters are replaced by the revision number. The work in this thesis pertains to revision L12; the following section discusses two LOC applications that required implementation or improvement in the ICKAALXX series. Although the detailed workings of the L12 system chip is not the focus of this thesis, it is helpful to review the platform to give context to the work done here. Figure 2.1 displays three images of the L12 chip to give a sense of its physical scale and its technical complexity.

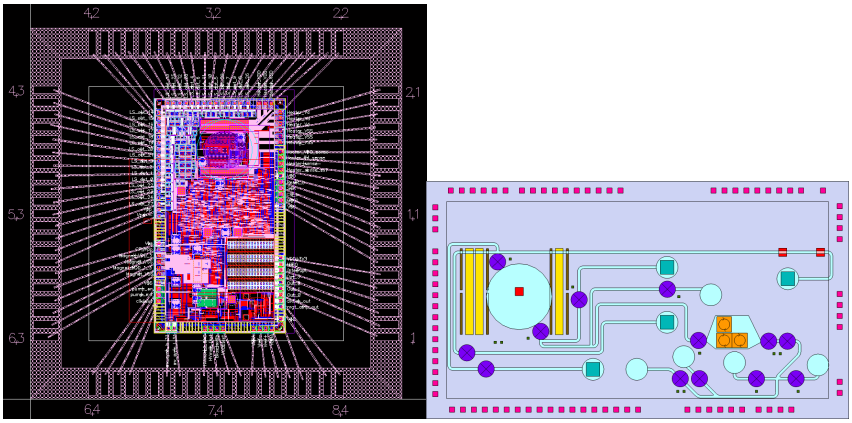

(a) (b)

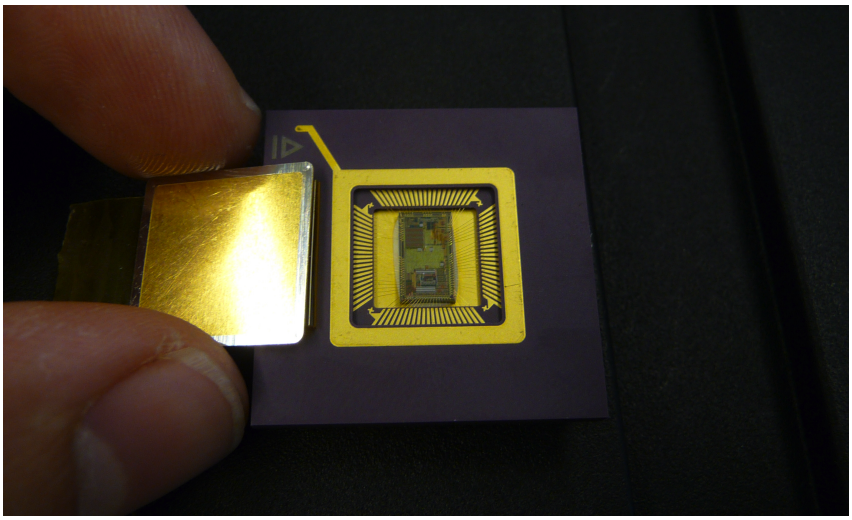

(c)

Figure 2.1: (a) CAD bonding layout for the L12 system chip. (b) Potential microfluidic layout for doing a full SP-PCR-CE test on L12. (c) Photograph of a packaged L12.

2.3 Two Contemporary Lab-on-Chip Issues

After reviewing a few the state of the art concepts in LOC technology in general and exploring the motivation for working on such problems, it is clear that there are many useful areas for research and development in the field. Two particular problems in DNA-based genetic LOC testing are identified (sample preparation and robust thermal systems) and possible solutions are developed herein. More in-depth reviews of these topics are covered in their respective chapters.

2.3.1 Sample Preparation

The first of the two topics on which this thesis is focused is sample preparation in a next-generation microfluidic platform. Traditional DNA SP methods applied to LOC technology suffer from drawbacks, such as the use of PCR-inhibiting reagents. Magnetic beads are used in many modern methods for DNA isolation that avoid the use of harsh reagents. The avoidance of PCR inhibitors in upstream processes is crucial for LOC applications where surface area to volume ratio is extremely high. Additional background is discussed in detail along with a proposed LOC solution in chapter 3.

2.3.2 Robust Thermal Systems

The second of the two topics of focus in this thesis is designing very rapid and thermally robust systems in a microfluidic-CMOS integrated microfluidic platform. Micro-heaters for PCR in LOC devices have many requirements, including low cost, high speed, and uniformity in the PCR volume temperature. Moreover, LOC heaters should be robust to changes in ambient conditions during operation. A flexible and deterministic design methodology for producing LOC heaters that show excellent heating selectivity and uniformity is discussed in chapter 4 along with its application to five heater designs.

2.4 Conclusions:

LOC Background and the State of the Art

By exploring background information on the three components of molecular diagnostics of interest to the BioMEMS project group (sample preparation, amplification and detection) a solid foundation in the importance of doing research in SP methods and thermal systems has been gained. Such background is important when designing the next-generation integrated microfluidics-CMOS LOC modules: sample preparation in chapter 3, and thermal systems in chapter 4.

CHAPTER 3

SAMPLE PREPARATION IN INTEGRATED MICROFLUIDICS-CMOS LOC TECHNOLOGY

To integrate the first step in the diagnostic process (SP) into a state of the art LOC system as described in section 1.5, FEM techniques are used in designing an electromagnetic system for trapping magnetic SP beads. Background information on sample preparation methods in general and in bead-specific applications is explored. The physics important in doing magnetic-based microfluidic SP on a CMOS-scale is investigated. FEM techniques are used to explore different topologies for achieving a system that is over-designed to ensure bead trapping ability. A CMOS test chip is manufactured and tested to ensure beads are rapidly trapped in a static droplet of water. A PCB device is constructed to act as a proxy for the CMOS electromagnet design, and it is used to quantitatively validate the FEA modeling/conservative design estimate method. Finally, a selected CMOS electromagnet coil design is added to the latest iteration of the BioMEMS project's full system chip, ICKAAL12.

3.1 Sample Preparation Methods

After briefly exploring the three components of molecular diagnostics (sample preparation, amplification and detection) that the BioMEMS project group focuses on, an understanding of the importance of the sample preparation step is clear. The recent demonstrations discussed in this chapter show clever ways to do POC testing. However, a gap in the literature is revealed; there has been little work in the way of doing on-chip SP for PCR applications, and the field is lacking in manufacturable solutions to the general problem of magnetic bead trapping. These conclusions set the stage for the purpose of this thesis chapter, which is to design, build and test a CMOS SP module that can be integrated with our existing system chips.

3.1.1 Standard Laboratory Sample Preparation Methods

As defined in section 2.1.1, SP for DNA-based molecular diagnostics consists of the isolation and purification of DNA from a raw sample. Many companies in the life sciences offer proprietary products and methods for doing SP. In general, to extract DNA from a raw sample, at least three main steps are required. First, since DNA resides inside cells (regardless of their type or origin), those cells must be broken open to release the DNA - this process is known as cell lysis. Second, the DNA must be selectively extracted and separated from cell debris. Finally, the DNA must be released for the next step in the process, amplification.

Extracting DNA from a raw sample can be a very labor-intensive and complicated process. The traditional method is known as phenol-chloroform extraction [38]. Phenol-chloroform and a chaotropic salt agent (denaturant) are added to the raw, aqueous sample. Since phenol-chloroform and water are immiscible, the solution must be mixed vigorously to create an emulsion of organic solvent droplets throughout the aqueous phase. Proteins are denatured and separate out into the phenol phase droplets, whereas the polarized DNA is drawn into the aqueous phase. Centrifugation of the sample then separates the organic solvent (phenol) phase from the aqueous phase, effectively isolating the DNA, which can be pipetted off the top of the separated solution. Chaotropic salts remain with the DNA, and must be removed since they inhibit PCR. Ethanol precipitation of DNA is done by adding sodium acetate and ethanol to the aqueous DNA solution, which causes the DNA to precipitate out of solution, and can be centrifuged into a pellet. The ethanol is then removed, the DNA washed, and the pellet can be re-suspended in any aqueous solution of choice. It takes well over an hour to complete the entire DNA extraction procedure.

It is evident that the traditional DNA SP method has many drawbacks, including protocol complexity, the use of PCR-inhibitors, moving parts (centrifuge) and long wait times. Newer solid-phase extraction (SPE) methods such as column-based purification have decreased the time required to do DNA isolation, but the use of PCR-inhibiting chaotropic salts is still required.

3.1.2 Magnetic Bead-Based Sample Preparation Methods

The trend of using micro-scale beads in sample preparation methods has steadily climbed over the past decade. With applications in DNA, RNA and protein isolation, many different types of magnetic sample preparation beads have become available. In general, these superparamagnetic beads range

in size from approximately 0.5 - 5 µm ([39–47]) and are made of highly permeable alloy cores which are surrounded by some type of polymer shell and then a functionalization of choice. The analyte of interest is bound by the specificity of the bead, and isolation is achieved by separating the magnetic beads from the sample solution.

The Dynabeads® brand sold by Life Technologies™ offers different surface functionalizations of these microspheres that allow for cell isolation, protein purification and DNA isolation [39]. Another Life Technologies™ brand, ChargeSwitch® (CS), produces beads that selectively bind and release DNA based on their surface charge, which is adjustable via pH [48]. Furthermore, the CS bead protocol is completely water-based - that is, it does not make use of harsh reagents including the organic solvents, alcohols and chaotropic salts that act as PCR-inhibitors downstream (as described in section 3.1.1). This is extremely important to LOC technology; there can be many competing effects at the micro-scale that inhibit successful results, and it is always desirable to make use of simplified and downstream-compatible processes whenever possible. Despite the clear benefits to using CS technology in LOC devices, more groups still work with Dynabeads® and various protein isolation methods than DNA-isolation applications.

With so many commercially available types of magnetic beads for a wide array of sample preparation requirements, it is no surprise that many LOC publications from the last decade have made use of these convenient off-the-shelf components.

3.2 Microfluidic Bead-Based Separation

One of the first demonstrations of magnetic beads in LOC devices was by Choi in year 2000, where a planar serpentine electromagnet was electroplated on a silicon wafer [49]. A permalloy was also electroplated around the copper serpentine traces (with insulation) to spread out the magnetic fields and allow for even distribution of magnetic beads. No bio-separation was performed with the device. In a subsequent paper [50], the same group utilized a planar spiral electromagnet to perform the same bead-trapping function. As in their first paper, bio-separation applications were envisioned but not performed. A different separation approach was taken by Tondra et al. in [51], where 0.46 µm beads were caused to take one of two paths in a “forked” channel by the application of an in-plane cross-channel gradient in the magnetic field. While these were all good physical demonstrations of electromagnets manipulating magnetic beads, they were all very labour intensive and required much fabrication work. In 2004, Ramadan et al. showed finite-element analysis (FEA) simulations of

three electromagnet topologies [52], chose the "best" option based on magnetic field produced, and then fabricated it for testing, but with no biological assay performed. Smistrup et al. then published simulation and qualitative experimental results in 2005 on the movement and capture efficiency of beads in a microchannel with integrated planar spiral coils [53]. In two subsequent papers in 2006 and 2007, Smistrup et al. published the fabrication scheme for their planar coils and a theoretical investigation of a magnetic bead separator that combined small permanent magnets and strategically placed soft magnetic structures [54, 55].

In one of the first attempts at a biological assay performed with a LOC device for magnetic separation of beads, Moser et al. built a hand-held instrument composed of small permanent magnets, soft magnetic probes and a large electromagnet [56]. The device was used to trap magnetic beads as a sample flows in a microchannel past the soft magnetic tips which produce a very large magnetic field gradient perpendicular to the direction of flow. The bead-analyte conjugates collect on one side of the channel and the bioassay is based on the size of the agglutinated particle plug. The higher the concentration of analyte, the more significant the agglutination takes place, so the tighter the plug becomes and the smaller it appears in the channel. While this agglutination procedure was a significant step forward in terms of actually attempting a biological assay with a magnetic bead-based LOC device, it is still a far cry from the complexity of doing DNA isolation with magnetic beads on chip, since no true biological sample was tested, and nothing had to be recovered from the test (which is the purpose of sample preparation).

Another unique method for sample detection with magnetic beads was shown by Florescu et al. in [40]. A CMOS device consisting of three parallel wire traces was fabricated and the surface of the chip was functionalized with antibodies specific to the analyte of interest. The sample was then washed over the chip, and the analytes of interest were bound to antibodies from the previous step. The middle of the three traces (the "concentration" conductor) is turned on, and functionalized magnetic beads are then placed onto the functionalized area, binding strongly to the analyte-antibody conjugate which is fixed to the surface of the chip. The concentration conductor is turned off, and the two "washing" conductors are turned on, which reside on either side of the concentration conductor. Any beads that are not bound to the analyte-antibody conjugate are pulled away from the middle trace to either side. The number of beads that remain on the middle trace (in spite of the applied field) is proportional to the concentration of the analyte of interest. Again, this publication was a step forward in the collection and detection of a protein analyte of interest, but has less impact when

considering the isolation of DNA.

Dupont et al. fabricated a silicon chip for integrating magnetic manipulation and optical detection [37]. Magnetic beads were fluorescently labeled and functionalized with specificity for a cancer biomarker antibody (protein-based preparation and detection). Ramadan and Gijs demonstrated a system for sample washing and concentration of magnetic beads in 2010 [42]. Under continuous flow of sample through a microchannel, a rotating array of permanent magnets allowed for periodic trapping and releasing of beads. One trap/release event was cited as one wash cycle, and the purification efficiency of trapping magnetic beads from a sample was recorded to be about 83% at a flow rate of $0.5\,\mu\mathrm{L\,min^{-1}}$. As in all the previously mentioned demonstrations, the bioassay in [42] was protein-based.

Finally, one recent demonstration by Fulcrand et al. showed very good spatial manipulation of magnetic microbeads [43]. Square spiral coils were miniaturized to approximately $100\,\mu\mathrm{m}$ on a side and were fabricated on a polymer (SU-8) base, and beads were able to be held against a flow rate just under $1\,\mu\mathrm{l\,min^{-1}}$. While no bioassay was performed, this demonstration showed precise manipulation of bead batches, although the fabrication process was fairly complex, as it involved electroplating.

3.3 CMOS Magnetic Bead Sample Preparation

As mentioned in section 3.2, a useful development would be the design of a generic magnetic bead sample preparation module that conforms to the idea of the next generation of truly integrated LOC platforms. Ideally, the system would integrate the fluidic and electronic pieces that make up the diagnostic process. As discussed in section 1.5, one option for achieving this scenario is to use polymer-on-CMOS technology. This is the central focus of this chapter, and all other explored platforms act as prototyping methods to support this development process in various ways. The significant gap in the literature for manufacturable solutions to the problem of magnetic bead manipulation means that there is space for this research to take place. Many improvements can be made over the existing platforms described in section 3.2 through miniaturization. Furthermore, there has been much less work in the context of doing DNA sample preparation for downstream PCR.

The small working volumes associated with CMOS-scale diagnostics require that, for bead-based SP, the CMOS module be paired with off-chip infrastructure that enables the reduction of

macro-scale fluid volumes down to something that is reasonable for on-chip (CMOS) processing (the off-chip first-step SP infrastructure will be design work for others). Once on chip, the final SP concentration step enables the direct elution of concentrated sample into the PCR chamber, maximizing the amount of sample to be processed and avoiding a common point for contamination. Final concentration and direct elution to the PCR chamber are important design functions that cannot be achieved with off-chip sample preparation alone; since CMOS is used in our other PCR-CE diagnostic functions, it is a logical progression to add SP to the process for a full three-step SP-PCR-CE protocol.

Based on the state of the art reviewed in sections 2.1 - 3.2 in addition to the evolution of LOC technology as described in section 1.3 - 1.5, it was proposed that a magnetic bead-based SP module be brought up to the level of development that already exists in our system chips for on-CMOS PCR and CE/MCA. This platform could be used for techniques which use beads that are for methods other than DNA processing - it is applicable to any bead that is magnetically sensitive. Due to the DNA-SP gap in the literature, and the BioMEMS project team's focus on the three diagnostic steps of SP, PCR and CE/MCA, the project will be focused on the development of a solution that works with magnetic beads, such those described in section 3.1.2.

Glass-based microfluidic systems designed previously as part of the BioMEMS project made it apparent that it is easy to "blow" beads away from a "trapping" region of a regular channel by increasing the flow rate beyond the holding capacity of the magnetic system. In these earlier experiments, an external, mechanically-operated permanent magnet was being used to trap magnetically susceptible beads. Polymer-based valves were used as a peristaltic pump (which can also be implemented in a polymer-on-CMOS system), and only by experimental trial-and-error were acceptable flow rates determined. Valve slew rate is examined in section 3.5.1 to learn from these previous issues and consider their impact during the design phase.

These issues and others are explored in subsequent sections; a review of the physics associated with doing magnetic bead isolation is presented in the next section.

3.4 Physics of Magnetic Bead Isolation

3.4.1 Magnetic Theory

Magnetic flux density (B), measured in Tesla (T) is a quantity describing the number of magnetic field lines per unit area. Homogeneous magnetic fields have a constant flux density over a given region. Conversely, inhomogeneous magnetic fields present a gradient in the magnetic flux density over a given region. Magnetic gradients are required for applying magnetic force, so some kind of magnetic inhomogeneity is necessary in the system.

The magnetic permeability of a material (μ) describes the ability of that material to support within itself a certain magnetic flux density. Related to the magnetic permeability of a material is the quantity known as magnetic susceptibility (χ). The two properties are related as shown in equations 3.1 and 3.2.

$$\mu_r = \frac{\mu}{\mu_0} \tag{3.1}$$

$$\chi_v = \mu_r - 1 \tag{3.2}$$

It should be noted that χ_v is the dimensionless *volume magnetic susceptibility*, which differs from both the *mass* ($\mathrm{m^3\,kg^{-1}}$) and *molar* ($\mathrm{m^3\,mol^{-1}}$) susceptibilities by certain factors. The mass susceptibility is adjusted for material density ($\chi_{mass} = \chi_v/\rho$), and the molar susceptibility by the density and molar mass ($\chi_{mol} = M\chi_v/\rho$), where ρ is the density in $\mathrm{kg\,m^{-3}}$ and M is the molar mass in $\mathrm{kg\,mol^{-1}}$. Furthermore, these three susceptibilities are sometimes quoted in CGS units, which differ from SI units by a factor of $(4\pi)^{-1}$. Throughout this work, SI units will be maintained and the volume magnetic susceptibility will be used, unless otherwise noted.

The magnetic susceptibility can be used to identify a material's magnetic classification as ferromagnetic, paramagnetic or diamagnetic. Ferromagnetic materials present susceptibility values $\chi_v \gg 0$, and are highly attracted to externally applied magnetic fields. Even when the field is removed, the material will retain some magnetic properties. Iron and nickel are two common examples of this classification. Paramagnetic materials have $\chi_v > 0$ and are also attracted to field maxima, though less strongly than ferromagnetic materials. When the external field is removed, the materials does not retain the magnetic properties. Two such materials are oxygen ($\chi_{v,O_2} = 1.8 \times 10^{-6}$) and platinum ($\chi_{v,Pt} = 2.7 \times 10^{-4}$ - fairly small values compared to the susceptibilities

of the iron oxides FeO ($\chi_{v,FeO} = 0.0072$) and Fe_3O_4 ($\chi_{v,Fe_3O_4} = 1.2 - 19$). Diamagnetic materials have susceptibility values of $\chi_v < 0$ and are repelled by magnetic field maxima. As in paramagnetic materials, diamagnetic materials retain no magnetic properties upon removal of the external field. The majority of materials are characterized as weakly diamagnetic, including water ($\chi_{v,H_2O} = -9.0 \times 10^{-6}$) and silica ($SiO_2$) ($\chi_{v,SiO_2} = -1.6 \times 10^{-5}$). Also included in the diamagnetic group are biological components such as cells, protein and DNA. There is an additional special case known as superparamagnetism. Superparamagnetic particles exhibit positive susceptibility when placed in a magnetic field, but display no remanent magnetization once the external magnetic field is removed. Superparamagnetic behaviour is characterized by a relaxation time τ, which describes the time required for the particles to reach zero magnetization when the external field is removed. The relaxation time is expressed as: $\tau = \tau_0 exp(^{KV}/_{\kappa_B T})$, where τ_0 is the characteristic time 10^{-9} s, K is the anisotropy energy, V is the particle volume, κ_B is the Boltzmann constant, and T is the temperature [57].

3.4.2 Magnetic Force on a Particle

As discussed in section 3.4.1 above, an inhomogeneous magnetic field is required to impart a magnetic force on a superparamagnetic particle. This force is described by equation 3.3, up to the point of magnetic saturation [58].

$$\vec{F_m} = \frac{V\chi_v}{\mu_0}(\vec{B}\cdot\nabla)\vec{B} \tag{3.3}$$

V is the volume of the particle, χ_v is the volume magnetic susceptibility, μ_0 is the permeability of free space, and $(\vec{B}\cdot\nabla)$ is the convective operator [59] of the magnetic flux density $\vec{B}$. This equation can be expanded to what is shown in equation 3.4, and then rearranged in its cartesian components $\hat{i}$, $\hat{j}$, and $\hat{k}$. These components are shown together in equation 3.5.

$$\vec{F_m} = \frac{V\chi_v}{\mu_0}\left(B_x\frac{\partial}{\partial_x}+B_y\frac{\partial}{\partial_y}+B_z\frac{\partial}{\partial_z}\right)\left(B_x\hat{i}+B_y\hat{j}+B_z\hat{k}\right) \tag{3.4}$$

$$\begin{aligned}\vec{F_m} = \frac{V\chi_v}{\mu_0}\Bigg[&B_x\left(\frac{\partial B_x\hat{i}}{\partial_x}+\frac{\partial B_y\hat{j}}{\partial_x}+\frac{\partial B_z\hat{k}}{\partial_x}\right)+\cdots\\&\cdots+B_y\left(\frac{\partial B_x\hat{i}}{\partial_y}+\frac{\partial B_y\hat{j}}{\partial_y}+\frac{\partial B_z\hat{k}}{\partial_y}\right)+\cdots\\&\cdots+B_z\left(\frac{\partial B_x\hat{i}}{\partial_z}+\frac{\partial B_y\hat{j}}{\partial_z}+\frac{\partial B_z\hat{k}}{\partial_z}\right)\Bigg]\end{aligned}$$

$$\begin{aligned}\vec{F_m} = \frac{V\chi_v}{\mu_0}&\left(B_x\frac{\partial B_x}{\partial_x}+B_y\frac{\partial B_x}{\partial_y}+B_z\frac{\partial B_x}{\partial_z}\right)\hat{i}+\cdots\\&\cdots+\left(B_x\frac{\partial B_y}{\partial_x}+B_y\frac{\partial B_y}{\partial_y}+B_z\frac{\partial B_y}{\partial_z}\right)\hat{j}+\cdots\\&\cdots+\left(B_x\frac{\partial B_z}{\partial_x}+B_y\frac{\partial B_z}{\partial_y}+B_z\frac{\partial B_z}{\partial_z}\right)\hat{k}\end{aligned} \tag{3.5}$$

Alternatively, this equation can be shown separately as equations 3.6 to 3.8. This is useful since we can make conservative estimates of the force required to oppose fluid drag from flow, which is in one direction only.

$$\vec{F_{mx}} = \frac{V\chi_v}{\mu_0}\left(B_x\frac{\partial B_x}{\partial_x}+B_y\frac{\partial B_x}{\partial_y}+B_z\frac{\partial B_x}{\partial_z}\right)\hat{i} \tag{3.6}$$

$$\vec{F_{my}} = \frac{V\chi_v}{\mu_0}\left(B_x\frac{\partial B_y}{\partial_x}+B_y\frac{\partial B_y}{\partial_y}+B_z\frac{\partial B_y}{\partial_z}\right)\hat{j} \tag{3.7}$$

$$\vec{F_{mz}} = \frac{V\chi_v}{\mu_0}\left(B_x\frac{\partial B_z}{\partial_x}+B_y\frac{\partial B_z}{\partial_y}+B_z\frac{\partial B_z}{\partial_z}\right)\hat{k} \tag{3.8}$$

From the equations above we can see that the force on a particle depends on properties of the particle itself, and on properties of the magnetic field. More specifically, the force is dependent on both the magnitude and gradient of the magnetic field. If the magnetic field is homogeneous, that is, there exists no gradient in the flux density, then the $(\vec{B}\cdot\nabla)$ term goes to zero and the force is also zero.

If the particle is subjected to a magnetic field sufficient for saturation, then the particle's magnetization levels-off, reaching a constant value of $\vec{M_s}$. At saturation, the force the particle experiences can be simplified to:

$$\vec{F_m} = \frac{V\chi_v}{\mu_0}(\vec{B_s}\cdot\nabla)\vec{B} \tag{3.9}$$

$$= V(\vec{M_s}\cdot\nabla)\vec{B} \tag{3.10}$$

Or, separated into cartesian equations:

$$\vec{F_{mx}} = V\left(\vec{M_{s,x}}\frac{\partial B_x}{\partial_x} + \vec{M_{s,y}}\frac{\partial B_x}{\partial_y} + \vec{M_{s,z}}\frac{\partial B_x}{\partial_z}\right)\hat{i} \tag{3.11}$$

$$\vec{F_{my}} = V\left(\vec{M_{s,x}}\frac{\partial B_y}{\partial_x} + \vec{M_{s,y}}\frac{\partial B_y}{\partial_y} + \vec{M_{s,z}}\frac{\partial B_y}{\partial_z}\right)\hat{j} \tag{3.12}$$

$$\vec{F_{mz}} = V\left(\vec{M_{s,x}}\frac{\partial B_z}{\partial_x} + \vec{M_{s,y}}\frac{\partial B_z}{\partial_y} + \vec{M_{s,z}}\frac{\partial B_z}{\partial_z}\right)\hat{k} \tag{3.13}$$

These equations are included for completeness; for the planar electromagnets presented here, equation 3.3 is utilized for magnetic force calculations since the fields generated by these designs are not high enough to saturate the beads. As an example, refer to figure 3.1, which shows that the magnetic flux density generated by a 5-turn planar spiral electromagnet is less than 0.01 T. Although there is considerable disagreement in the literature on the saturation field value for various magnetic beads, all values presented in table 3.2 of section 3.5 are greater than 0.01 T (the lowest saturating field explicitly reported in those publications is 0.62 T for the M-450 Dynabead, and a BH curve for the MyOne Dynabead [60] shows a saturation value around 0.05 T).

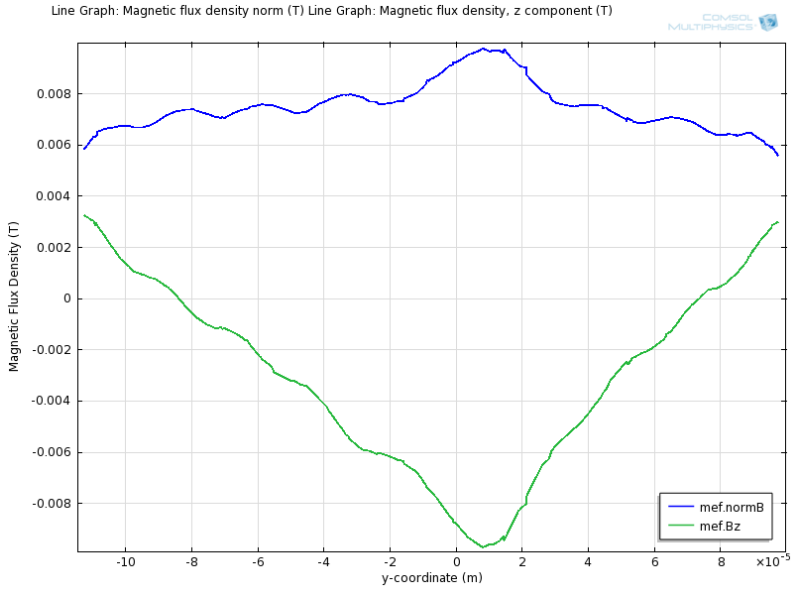

Figure 3.1: 1D plot of the magnetic flux density norm ($\vec{B}$) and z-direction field ($\vec{B}_z$) generated by a 5-turn square spiral electromagnet.

3.4.3 The Use of Electromagnets and Alternatives

As discussed in section 1.5, the next generation of LOC systems in our group are being built on CMOS platforms. Modern examples of electromagnetic designs were presented in section 3.2 Although it is difficult to build an electromagnet that produces as much field strength as even a small neodymium iron boron (NdFeB) magnet, building an electromagnet in a CMOS platform for bead trapping has several distinct advantages. Firstly electromagnets generally exhibit massive gradients, which contribute to the force magnitude on a magnetic particle, as demonstrated by equation 3.3. As with any electromagnet, the field is adjustable, which introduces selectivity. The electromagnet can be turned on and off, allowing for manipulation of magnetic beads in ways that permanent magnets can only achieve if they are mounted with moving parts, which complicate packaging and introduce the possibility for mechanical failures. In an integrated circuit (IC), an electromagnet could be constructed within 10 µm of a microfluidic channel, yielding high resolution of trapping. That is, spatially, an electromagnet can manipulate beads with much better precision than a permanent magnet. The ability to selectively trap and release beads introduces the option to cascade stages of preparation volume. A bulk sample (1 mL for example) could be progressively reduced in stages by

alternately trapping and releasing beads into smaller buffer volumes until the desired PCR chamber volume (less than a microlitre) is reached. This kind of cascading reduction in volume is not possible with fixed CS structures such as channels or posts.

Electromagnets are not without their disadvantages, however. Field strength is significantly lower than with permanent magnets, and Joule-heating of the electromagnetic elements may render them too hot to be used for sample preparation applications, unless adequate heat-sinking is provided.

With ample heat-sinking options in CMOS packaging and the ability to minimize the distance between the electromagnet and the target fluidics, our system chip platform should support the requirements of an on-chip sample-preparation module.

3.4.4 Equating the Forces Acting on the Microbeads

When considering the forces acting on a magnetic bead in a microchannel, we can approximate the system to that of two parallel plates, since the planar direction perpendicular to flow is not impactful. We wish to be able to draw beads downwards out of the fluid flow, and we also wish to hold them against the drag imposed by that fluid flow by acting with a magnetic force acting the opposite direction. For the example calculations of this section, the microchannel will be assumed to be 10 µm in height, 200 µm in width and 10 mm in length.

3.4.4.1 Vertical Forces and Settling Time

Microfluidic systems generally operate in fluid flow regime that is characterized by a very low Reynolds number. As long as the Reynolds number governing a system is much less than one, $(Re < 0.1)$, then Stokes' law for the drag force exerted on a spherical object by a viscous fluid holds true.

$$Re = \frac{\rho v_{rel} D_H}{\mu} \tag{3.14}$$

Where Re is the Reynolds number, ρ is the density of the fluid medium, v_{rel} is the relative velocity of the fluid (this quantity is referred to as the "relative velocity" to distinguish it from other common fluid flow rate terms), D_H is the hydraulic diameter where for a spherical object

$D_H = D_{sphere}$, and μ is the dynamic viscosity of fluid medium. Using the values provided in table 3.1 below, equation 3.14 shows that the system is well within the laminar flow regime: leaving v unsolved-for, $Re = (0.998\,\mathrm{s\,m^{-1}})(v_{rel}\,\mathrm{m\,s^{-1}})$. Thus, Stokes' law holds as long as the fluid relative velocity (i.e., in this case, the velocity of the bead with respect to the fluid) does not exceed $1\times10^{-1}\,\mathrm{m\,s^{-1}}$. That is, $Re \leq (0.998\,\mathrm{s\,m^{-1}})(1\times10^{-1}\,\mathrm{m\,s^{-1}}) = 0.1$.

$$\vec{F}_d = 6\pi\mu v_{rel} r \tag{3.15}$$

Where $\vec{F}_d$ is the Stokes' drag force, μ is the dynamic viscosity of the fluid medium, v_{rel} is the relative velocity of the fluid to the bead, and r is the radius of the particle. Also acting on the bead is gravity:

$$\vec{F}_g = mg \tag{3.16}$$

Where $\vec{F}_g$ is the force due to gravity, g is the acceleration due to gravity, and m is the mass of the particle. Finally, we also have buoyancy acting on the magnetic bead, which can be described as:

$$\vec{F}_b = \frac{4}{3}\pi r^3 \rho_f g \tag{3.17}$$

Where $\vec{F}_b$ is the buoyancy force acting on the spherical particle, r is again the radius of the particle, ρ_f is again the density of fluid medium, and g is again acceleration due to gravity. Using these equations, we can come up with an expression for the settling velocity of the 1 µm diameter CS beads (see figure 3.2). Equating 3.15, 3.16 and 3.17:

$$\vec{F}_g = \vec{F}_d + \vec{F}_b$$

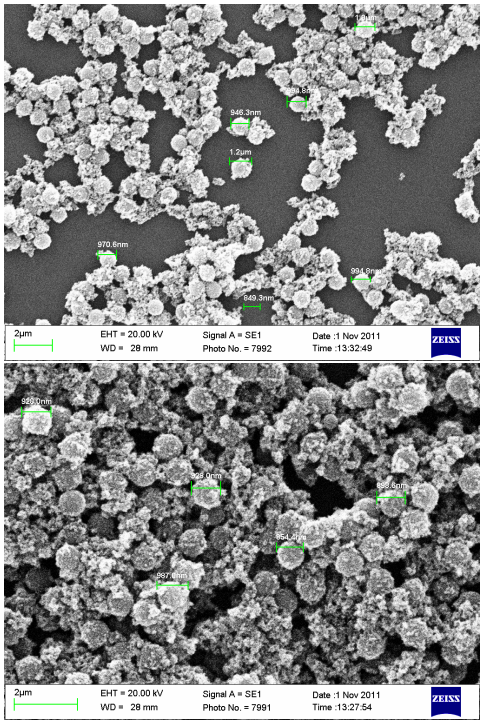

Figure 3.2: Scanning electron micrograph of a sample of ChargeSwitch beads. The SEM images confirmed the 1 µm bead diameter quoted by the manufacturer.

After substituting the expressions for each of the force terms, rearranging and solving for the settling velocity v_s, we arrive to the expression:

$$v_s = \frac{2r^2 g\left(\rho_b - \rho_f\right)}{9\mu} \tag{3.18}$$

The settling velocity is an important quantity in doing microbead-based assays. Settling velocity is also known as the terminal velocity, and it describes the maximum velocity of a falling particle when acceleration is zero since drag and buoyancy equal the force due to gravity, as per 3.18. In the context of our microfluidic platform, if the force due to gravity on our magnetic CS beads is sufficient to pull those particles downwards into the range of the magnetic field produced by the electromagnet in a reasonable amount of time, then the channel has little restriction on height. However, if it turns out that the settling time for those beads to reach a region of the channel that contains electromagnetic forces is longer than it takes for the bead to pass through the channel, then

no sample preparation will take place at all. This condition would place a height restriction on our channel dimensions.

It is assumed for this calculation that the particle reaches its terminal velocity instantaneously. As a first case, consider that $\vec{F_{my}} = 0$.

Table 3.1: Parameters, values and descriptions necessary for settling velocity calculations.

Parameter	Value	Description
r	$0.5\,\mu\text{m}$	Radius of particle
g	$9.81\,\text{m}\,\text{s}^{-1}$	Acceleration due to gravity
ρ_b	$1700\,\text{kg}\,\text{m}^{-3}$	Density of magnetic bead
ρ_f	$1000\,\text{kg}\,\text{m}^{-3}$	Density of fluid medium (water)
μ	$1.002 \times 10^{-3}\,\text{N}\,\text{s}\,\text{m}^{-2}$	Dynamic viscosity of medium (water)
m	$8.9 \times 10^{-16}\,\text{kg}$	Mass of a single magnetic bead

Given the values listed in table 3.1, $v_s = 3.8 \times 10^{-7}\,\text{m}\,\text{s}^{-1}$. If a bead was dropping at this rate, it would take 43 minutes for the bead to drop one millimetre. This is unacceptably slow if we plan on flushing the sample through the device in less than ten minutes (the shorter the time, the better). We can conclude that $\vec{F_{my}}$ must be considered in order to have a bead of this size drop out of the flow and into the area in which $\vec{F_{mx}}$ can hold the bead against flow. Consider a second case in which $\vec{F_{my}}$ is non-zero. In this case, we add the acceleration of the particle due to electromagnetic force:

$$\vec{F_{my}} = ma_{m,y} \tag{3.19}$$

Including the additional downwards magnetic force term (as shown in figure 3.3) in the expression for equating forces yields:

$$\vec{F_g} + \vec{F_{my}} = \vec{F_d} + \vec{F_b} \tag{3.20}$$

$$mg + ma_{m,y} = \frac{4}{3}\pi r^3 \rho_f g + 6\pi\mu v_{rel} r \tag{3.21}$$

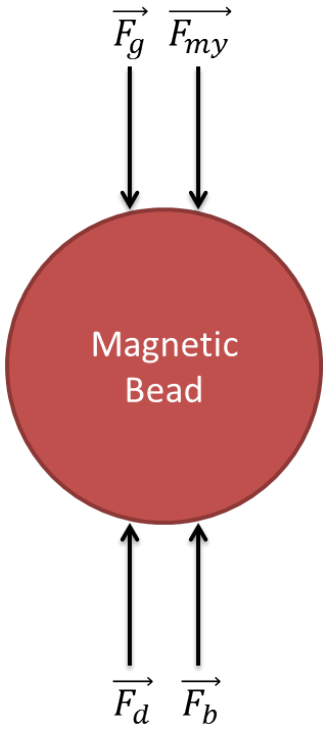

Figure 3.3: Free body diagram of a bead in free-fall.

Dividing both sides by $\frac{4}{3}\pi r^3$ and recalling that $\rho_b = {}^{m}/_{\frac{4}{3}\pi r^3}$, rearranging for the settling velocity shows:

$$v_s = \frac{2r^2\left(\rho_b\left(g + a_{my}\right) - \rho_f g\right)}{9\mu} \tag{3.22}$$

The terms within the brackets in equation 3.22 show that the value for a_{my} will have a significant effect on v_s if it dominates g. In fact, for $a_{m,y}$ to dominate g, it should be at least one order of magnitude greater than g to make a useful contribution to the settling velocity. Since g is on the order 10^1, a_{my} should be on the order 10^2. As per table 3.1, m is close to the order of 10^{-15}, so $\vec{F_{my}}$ should be on the order 10^{-13} to yield a_{my} on 10^2, as per equation 3.19.

Letting the parameters in equation 3.22 have values as in table 3.1 and $\vec{F_{my}} = 1 \times 10^{-13}\,\mathrm{N}$, then $v_s = 1.1 \times 10^{-5}\,\mathrm{m\,s^{-1}}$, or $11\,\mu\mathrm{m\,s^{-1}}$. Of course, the bead will continue to accelerate towards the electromagnets as $\vec{F_{my}}$ increases, but as a conservative estimate, the above calculations serve to demonstrate the need for, at the very least, tenths of pN in force to draw the beads out of solution. Channel height in microfluidic design can now be adjusted with the constraint that the channel

ceiling location demonstrates a force greater or equal to $\vec{F_{my}} = 0.1\,\text{pN}$.

3.4.4.2 Horizontal Forces

Continuing with the parallel plate approximation, there are two forces acting on the bead horizontally. It was discussed in 3.4.4.1 that Stokes' law holds for the relative velocity in free fall, but it is important to check that it also holds for the horizontal, against-flow, channel case. In this calculation we reference the shape of the channel cross section instead of the shape of the bead. Recall that the example channel for these calculations is 10 µm in height, 200 µm in width and 10 mm in length. The hydraulic diameter becomes $D_H = \frac{2WH}{W+H}$, where W and H are the channel width and height. Similar to before, we find that the Reynolds number is small as long as the system is operated below a certain maximum relative velocity (in this case, the relative velocity is the referencing the fluid velocity with respect to the channel walls): again leaving v unsolved-for and using the same parameters, $Re = (19.0\,\text{s}\,\text{m}^{-1})(v_{rel}\,\text{m}\,\text{s}^{-1})$. Thus, Stokes' law holds as long as the fluid relative velocity does not exceed $5.3 \times 10^{-3}\,\text{m}\,\text{s}^{-1}$. That is, $Re \leq (19.0\,\text{s}\,\text{m}^{-1})(5.3 \times 10^{-3}\,\text{m}\,\text{s}^{-1}) = 0.1$. Therefore, the drag force (equation 3.15) due to fluid flow acts on the bead. In the other direction, opposing flow, is the magnetic force required to hold the bead against that flow. In the simplest, most conservative case, we can equate the drag force on a particle to the magnetic force in the opposite direction, $\vec{F_{mx}} = \vec{F_d}$. The force required to hold a bead against a chosen maximum velocity can be approximated by rearranging the expression, or conversely, given an achievable force term in the direction opposing flow, a maximum velocity can be determined. This method ignores the contribution of friction, which contributes to holding the bead in place, working in favour of keeping the beads immobilized.

3.4.5 Pressure and Microchannel Flow

As in the previous section, the microchannel will be assumed to be 10 µm in height, 200 µm in width and 10 mm in length for sample calculations.

3.4.5.1 Pressure and the Non-Circular Factor

It is important to consider pressure gradients and their effect on fluid velocity in microfluidics. The pressure in a long channel can be described as:

$$\Delta P = \frac{32\mu L\lambda_{NC}}{D_H^2} v_{avg} \tag{3.23}$$

Where ΔP is the pressure difference between the two ends of a long channel, μ is the dynamic viscosity of fluid medium, L is the length of the channel, λ_{NC} is the non-circular coefficient (since the channel is rectangular), D_H is the hydraulic diameter and v_{avg} is the average relative velocity in channel; $v_{avg} = {}^{v_{vol}}/_{WH}$. Using the width ($W = 200\,\mu m$) and height ($H = 10\,\mu m$) of the channel, the non-circular factor (as described in [61]) is:

$$\begin{aligned} \lambda_{NC} &= \frac{3/2}{(1-(0.351)^{H}/_{W})^2(1+{}^{H}/_{W})^2} \\ \lambda_{NC} &= 1.4096 \end{aligned} \tag{3.24}$$

3.4.5.2 Couette and Poiseuille Flow

Couette flow is a well-known approximation that describes the laminar flow of a viscous fluid between parallel plates, which can describe our system relatively well, since the width of the channels are roughly an order of magnitude greater than the height. The system can be simplified further by noting symmetry of the channel.

In this case, two parallel plates (infinite in their planes) are separated by a distance h. The bottom plate is fixed, and the top plate moves at the maximum velocity of the fluid. The average (v_{avg}), volumetric (v_{vol}) and maximum relative (v_{max}) fluid velocities are related as follows:

$$v_{avg} = \frac{v_{vol}}{WH} = \frac{h^2}{12\mu}\left(-\frac{dp^*}{dx}\right) = \frac{2}{3}v_{max} \tag{3.25}$$

Neglecting any pressure gradient in the channel, the Navier-Stokes equation becomes $\frac{\partial^2 v_{max}}{\partial y} = 0$. Applying the boundary conditions imposed on the plates stated above, $v(0) = 0$, $v(h) = v_{max}$, then an expression for the fluid velocity with respect to height in the channel can be written as:

$$v(y) = v_{max}\frac{y}{h} \tag{3.26}$$

Plane Poiseuille flow takes Couette flow a step further by introducing the effect of a pressure gradient in the channel on the fluid velocity with respect to height. In this case, including the pressure gradient yields the Navier-Stokes equation to become $\frac{\partial^2 v_{max}}{\partial y} = \frac{\Delta P}{\mu}$. Two fixed plates separated by a distance h make up the theoretical channel, and the zero-slip boundary conditions at the channel floor $(v(0) = 0)$ and ceiling $(v(h) = 0)$ yields the plane Poiseuille equation for fluid velocity:

$$v(y) \quad = \quad v_{max}\frac{y}{h} + \frac{\Delta P}{2\mu}(y^2 - hy) \tag{3.27}$$

Finally, the y location for the spherical bead is defined for its center. If a 1 µm diameter bead was resting on the channel floor, for example, its y-location would be defined as 0.5 µm since that is the bead's radius, and the height of its center above the floor. This definition is upheld for all velocity calculations.

3.5 Design Considerations

Section 3.4 introduced all of the forces necessary to consider when designing a bead-based SP module. One important point to consider is brought up by equation 3.27: the relative velocity of the fluid is much faster in the middle of the channel than at the roof or floor. Beads will be pinned to the floor by the magnetic trap, placing them in a region of slow relative fluid velocity. Using the v found here, one could calculate the bare minimum force required to hold the beads against that flow. However, we are interested in producing a conservative design for several reasons. Firstly, it would be useful to have a generic platform that can accommodate magnetic beads of different sizes and susceptibilities. Table 3.2 summarizes a literature review of the susceptibilities of various magnetic beads for sample preparation reported to date. Note that none of the values for a 1 µm diameter bead are reported to be less than 0.75. Thus a value of $\chi_v = 0.5$ is a good conservative estimate for magnetic susceptibility of the CS beads used in this work given the field range that is expected.

It is desirable to have the highest v_{avg} possible to minimize the time required to complete the SP step. Another, one goal of our system chip is to use integrated polymer-on-CMOS electrostatic valves, which can induce a very high transient flow rate if their slew rate is high, due to the non-

Table 3.2: Literature review of susceptibility values for magnetic beads for sample preparation. Saturating field values are listed where available.

Bead Diameter [μm]	χ_v	**Saturating Field** [T]	**Magnetization at Saturation** (M_s)	**Source**
1 (Unknown)	1.377	1.1 T	40000 A m^{-1}	[42]
1 (Dynabead – MyOne)	1.5	N/A	N/A	[54]
1 (Dynabead – MyOne)	N/A	$\sim$ 0.05 T	N/A	[60]
1 (Dynabead – MyOne)	1.38	N/A	N/A	[44]
2.8 (Dynabead – M-270)	0.84	N/A	N/A	
2.8 (Dynabead – M-270)	0.17	N/A	N/A	[43]
2.8 (Dynabead – Oligo (dT)25)	0.192	N/A	N/A	[45]
4.5 (Dynabead – M-450)	0.25	1.2 T, 0.72 T	N/A	[46]
4.5 (Dynabead – M-450)	0.25	1.77 T, 1.12 T, 0.62 T	N/A	[62, 63]
4.5 (Dynabead – M-450)	0.8	N/A	N/A	[41]
8.5 (Bangs Labs. Inc., UMC4F)	0.2	N/A	N/A	[47]
Bulk magnetite (Fe_3O_4)	70	N/A	N/A	[64]

negligible valve throw volume. It is necessary to ensure beads are not "blown" away by the high transient fluid flow rate, so steps to mitigate this problem are taken. Given a conservative estimate for the maximum tolerable relative flow rate of fluid against a trapped bead, the minimum time for valve actuation can be calculated. This concept is explored further in section 3.5.1, after a useful value for the relative flow rate is found. To ensure a maximum holding force generated by the magnetic system, all steps in the design process were taken with conservative values. In particular, the v_{avg} quantity was used in calculating the against-flow force requirements.

Typical working volumes in gold-standard diagnostic and pathogen-detection processes is in the range of tens to hundreds of microlitres. In LOC microfluidics, working volumes can be as low as the nanolitre range. It is assumed in this work that the total volume of sample to be processed in the microfluidics-on-CMOS portion of the LOC is about 1 μL. This volume is not a significant departure from our previous work [6, 10], in which a PCR volume of 600 nL was successfully amplified in a PDMS-on-glass genetic analysis platform. Keeping the total test time down is important, but approximately 10 min is acceptable for the SP step, since this is less than a typical doctor's appointment. Given these quantities, the volumetric flow rate is 0.1 μL min^{-1}. The volumetric flow rate can be maintained at a high value if the channel is widened to reduce the local relative flow rate in an SP chamber. With an SP chamber width of 500 μm and the same height as the channel (10 μm),

the average relative flow rate $v_{avg} = \frac{v_{vol}}{WH}$ would be $333\,\mu m\,s^{-1}$. This v_{avg} corresponds to a holding force of 3.14 pN, from equation 3.15.

Although it is not necessary to calculate the exact dimensions of the SP module at this point, it serves as a good reality-check to calculate how long this SP module would have to be to ensure that the beads do not just flow past the magnetic trapping zone. From section 3.4.4.1 we know that a conservative estimate for a bead to be drawn from the top of the channel to the floor would be 2 s, assuming the design rule of $\vec{F_{my}} = 0.1$ pN at the top of the channel is achieved. If left unimpeded, a bead would travel 666 µm along the channel in this amount of time, given $v_{avg} = 167\,\mu m\,s^{-1}$. Therefore, a conservative approximation for the module length would be roughly that distance, if the $\vec{F_{my}}$ is as low as 0.1 pN.

In summary, we need to achieve a minimum of $\vec{F_{my}}$ on the order of 10^{-1} at the top of the channel and $\vec{F_{mx}}$ on the order of 10^{0} to oppose flow.

3.5.1 Valve Slew Rate

The valve design to be used in the microfluidic-CMOS integrated system has a displacement when actuated. Therefore, when in use for pumping or sealing off a microfluidic section, these valves cause pulsatile flow. A high valve slew rate can produce high relative flow rates which may (undesirably) dislodge trapped beads. By calculating the induced relative flow rate from the minimum actuation time of one of the electrostatic valves, it can be determined whether additional damping measures must be taken.

3.5.1.1 Valve Actuation Induced Flow Rate and Fluid Drag Force

The relative flow rate induced by an electrostatic valve actuation and its associated fluid drag force can be calculated as follows:

1. An electrostatic valve of given radius and KMPR feature height has a given throw volume.

   - Valve radius: $r = 150\,\mu m = 150 \times 10^{-6}\,m$
   - Polymer valve feature height: $h = 2\,\mu m = 2 \times 10^{-6}\,m$
   - Valve throw volume:

     $V_{valve} = \pi r^2 h = (\pi)(150 \times 10^{-6}\,m)^2(2 \times 10^{-6}\,m) = 1.4137 \times 10^{-13}\,m^3 = 0.14137\,nL$

2. We can expect the mechanical properties of the valve to limit the frequency to around 10 Hz [65].

3. Given the approximate mechanically damped frequency of the valve, calculate the $\vec{V_{rel}}$ produced by the full valve throw.

   - $t = 1/f = 1/10\,\text{Hz} = 0.1\,\text{s}$
   - $\vec{V_{rel}} = \frac{V_{valve}}{(w_{chamber})(h_{chamber})(t)} = \frac{1.4137 \times 10^{-13}\,\text{m}^3}{(800 \times 10^{-6}\,\text{m}^3)(10 \times 10^{-6}\text{m}^3)(0.1\text{s})} = 177\,\mu\text{m}\,\text{s}^{-1}$

4. Calculate the fluid drag force on a 0.5 µm bead exposed to that relative flow rate. If that force is on the order of what is achievable with the CMOS electromagnets, then electronic limiting of slew rate is required.

   - From equation 3.15, $\vec{F_{rel}} = 1.67\,\text{pN}$.

The fluid drag force on a bead exposed to the relative flow rate due to an electrostatic valve closing (damped only by natural mechanical properties) is on the same order (10^0) as the target magnetic force we are trying to achieve to oppose flow. Therefore electronic limiting of the valve actuation slew rate should be included on the system chip.

3.5.1.2 Strategies for Reducing Pulsatile Flow

As mentioned in section 3.3, our earlier work showed problems in dislodging beads due to the pulsatile flow produced by valve actuation. In the present designs, this issue is being corrected by the electronic limiting of valve slew rate described above. Additionally, some of the concepts below may help in reducing any problems introduced by pulsatile flow produced by electrostatic valves:

1. Natural mechanical damping of the valve due to the presence of an incompressible fluid.

2. Flexing of the SP chamber roof may mitigate some of the pressure produced by valve actuation.

3. Using a smaller diameter valve reduces the throw volume, in turn diminishing the high transient relative flow rate.

4. Branching of the chamber inlet and outlet would allow for dissipation of the pulsatile flow across multiple channels.

5. Use designs with a permanent magnet (not part of this work), which yields significant increases in $\vec{V_{rel,max}}$ and can withstand a higher valve slew rate.

6. Adjusting the frequency of the valve actuation (in addition to slew rate) to allow for bead "settling" before the next pump cycle.

3.6 Analytical Calculations of Simple Magnetic Fields

3.6.1 Straight Conductor

A commonly cited example for electromagnetic discussions is the case of an infinitely long, straight conductor with a circular cross section. Take, for example, one such conductor of radius r which carries a steady current I. The magnetic flux density outside the conductor can be calculated analytically. Figure 3.4 displays the cross section of this conductor. The field inside and outside the conductor can be determined by applying Ampere's circuital law with the enclosures labeled C_1 and C_2 in the diagram, as follows. Cylindrical coordinates facilitate the derivation.

1. Inside:

   - $B_1 = B_{\phi 1}\hat{\phi}$ and $dl = r_1 d\phi\hat{\phi}$
   - $\oint B_1 dl = \int_0 B_{\phi 1} r_1 d\phi\hat{\phi} = 2\phi r_1 B_{\phi 1}\hat{\phi}$
   - The current passing through the area enclosed by C_1: $I_1 = \frac{\pi r_1^2}{\pi r_c^2} I = \left(\frac{r_1}{r_c}\right)^2 I$.
   - Applying Ampere's circuital law: $B_1 = B_{\phi 1}\hat{\phi} = \frac{\mu_0 r_1 I}{2\pi r_c^2}\hat{\phi}$, when $r_1 \leq r_c$. μ_0 is the permeability of free space.

2. Outside: This case is similar to the inside case, but now the enclosure C_2 includes all of the current, I.

   - $\oint B_2 dl = 2\pi r_2 B_{\phi 2}\hat{\phi}$
   - The current passing through the area enclosed by C_2 is I.
   - Applying Ampere's circuital law: $B_2 = B_{\phi 2}\hat{\phi} = \frac{\mu_0 I}{2\pi r_2}\hat{\phi}$, when $r_2 \geq r_c$.

Thus, the magnitude of B increases linearly with r_1 on $[0, r_c]$ (inside the conductor), and decreases inversely with $r_2 \geq r_c$ (outside the conductor).

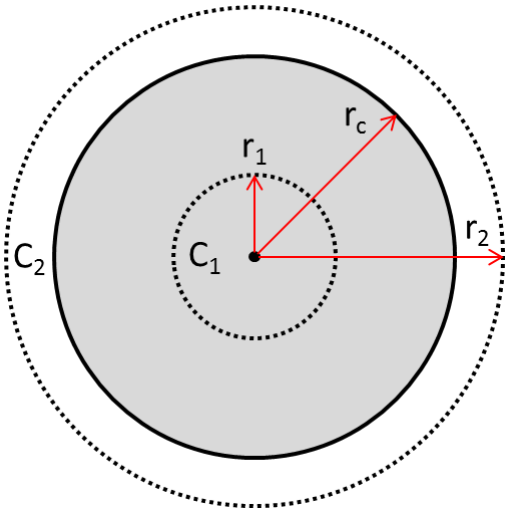

Figure 3.4: Cross section of the straight, infinitely long conductor of radius r_c. Two additional circles of radius r_1 and r_2 are shown, which are used in applying Ampere's circuital law.

When two long, straight, parallel conductors such as the one in the example above are placed closely side by side, there is an interaction between their magnetic fields. If the current is running in the same direction in each of the two conductors, then their fields are additive at a distance roughly greater than their radius, and the flux density is increased. If the conductors pass current in opposite directions, then there is some cancellation of flux density beyond this distance (an associated concentration of field between the conductors occurs). However, because the fields are reversed when current passes in opposite directions, there will be an associated increase in the field gradient between the conductors. This represents a tradeoff for a given application - field strength can be increased at the expense of gradient, or vice versa. Both of these options have merits and will be discussed further.

3.6.2 Square Loop Conductor

Another interesting example of analytical electromagnetism is the planar square loop, shown in figure 3.5. The field produced by this loop can be determined by combining the fields generated by the four segments that make up the square. Building from the result in section 3.6.1, the B field produced by a finite length segment of a straight conductor is $\frac{\mu_0 IL}{2\pi r\sqrt{L^2+r^2}}\hat{\phi}$ where L is the segment length and r is the distance from the segment center. Setting $L = r = w/2$, then $\vec{B} = \frac{2\sqrt{2}\mu_0 I}{\pi w}\hat{z}$. It

is notable that cancellation effects cause the field to be solely in the z-direction at the center of the loop. As with the straight conductor, this configuration has merits for microbead-based trapping, and is explored further.

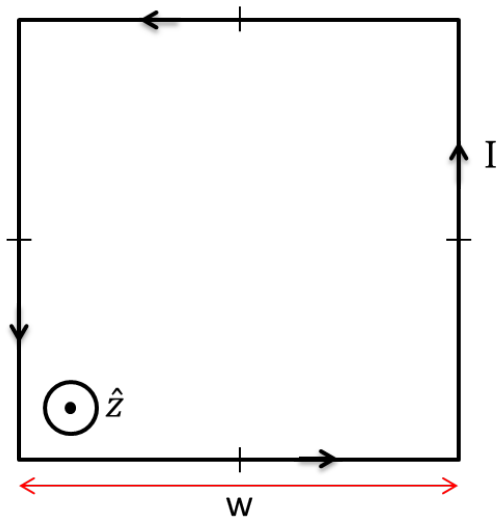

Figure 3.5: A square loop conductor of side length w. At the center of the loop, all the field lines run in the $\hat{z}$ direction.

3.7 Simulation Results and Discussion of CMOS-Scale Electromagnets

As discussed in section 3.2, there are many different topologies that can be explored for doing magnetic bead trapping for on-chip sample-preparation. Some designs work to maximize the magnetic flux density produced, whereas others take advantage of an increase in field gradient at the expense of flux density cancellation. Both of these strategies have merit, since the equation governing the force on a magnetizable object is affected by both quantities (refer to equation 3.3 section 3.4.2). The models investigated in this section were done to evaluate and optimize an electromagnet design for the CMOS bead-trapping application.

The TDSI manufacturing process used in producing the polymer on top of the CMOS system chips has a cross section containing four polymer layers, as shown in figure 3.6. The uppermost metal layer in the CMOS is labeled “Metal 3”, and its top surface is located directly beneath the 1 µm

passivation layer of SiN that protects the top surface of the CMOS. The closest channel possible to Metal 3, which will make up the electromagnet, would be fabricated in KMPR layer 2 (KMPR2). In contrast to the example calculations of the preceding sections which assumed a microchannel with a height dimension of 20 µm, a channel or chamber in KMPR2 would range 10 µm in height from $z = 3 - 13$ µm above Metal 3 (1 µm passivation + 2 µm KMPR followed by 10 µm of space until the channel ceiling). Thus, we are looking for maximum force term values in the region of 3 µm to 13 µm.

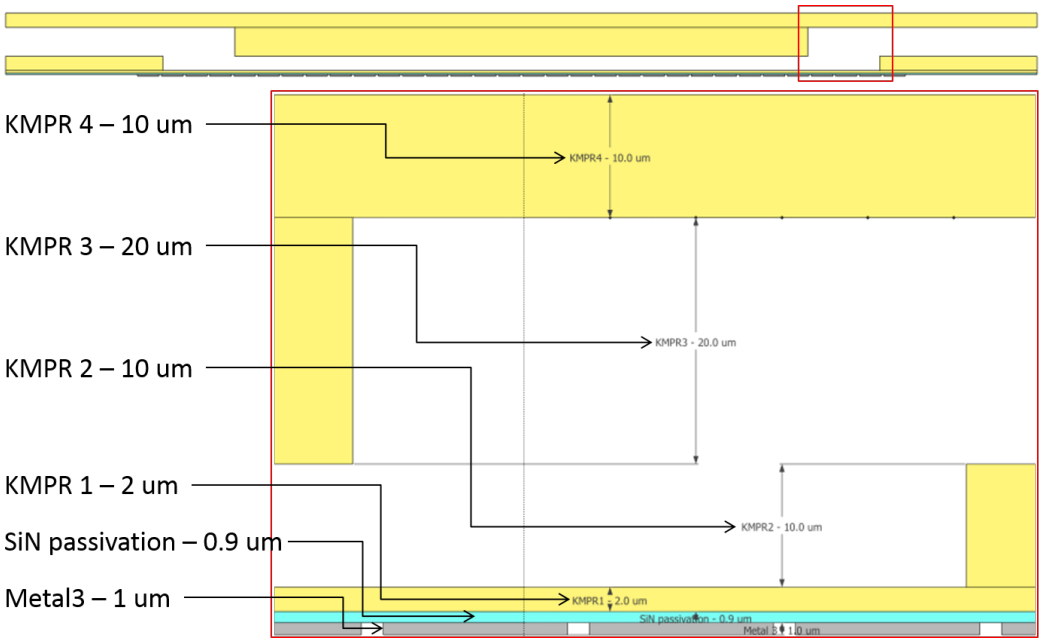

Figure 3.6: Potential TDSI KMPR-on-CMOS cross section. KMPR layers 1-4 are 2, 10, 20, and 10 µm in thickness, respectively. The silicon nitride passivation layer is $0.9 - 1$ µm in thickness and the Metal 3 layer is 1 µm thick.

The CMOSP8G Metal 3 layer has a ten-year lifetime limit for current density of $2 \times 10^9\,\mathrm{A\,m^{-2}}$. As the future of this project is in disposable units, we can justify a current density ten-times the ten year lifetime limit, or $2 \times 10^{10}\,\mathrm{A\,m^{-2}}$. Mean time to failure (MTTF) of a current-carrying conductor due to electromigration is inversely dependent on current density per Black's equation (MTTF $= \frac{A}{J^n} e^{\frac{E_a}{\kappa T}}$, where A is a constant, J is the current density, n is a parameter that can be experimentally determined, E_a is the activation energy, κ is the Boltzmann constant, and T is the absolute temperature). In a practical sense, these devices must only survive the lifetime of a PCR test.

Since we wish to complete this step in the diagnostic process as quickly as possible, this current density will be used throughout the design process. The HV bond pads in the CMOSP8G process are specified for a maximum of 300 mA. Additionally, in-house wire bonding is limited by the fusing current to roughly 400 mA. For this reason, all designs will conform to a track width of 15 µm to maximize current density and stay within the 300 mA threshold.

It is useful to set up an orientation when considering forces on the magnetic beads. For these models, the superior-inferior direction is z, and the transverse plane (xy) is where the microfluidic channels reside. Unless otherwise noted, the beads were defined as flowing along the$x$ axis, so that the main force term of interest was $\vec{F_{mx}}$ (to oppose flow directly). The $\vec{F_{mz}}$ force term is of interest in that it must achieve the minimum requirement of $\vec{F_{mz}} = 10^{-1}$ pN set out in section 3.5. The total magnetic force magnitude $\vec{F_{mm}}$ can also be plotted. This is typically what is quoted in literature, and so is investigated, but breaking the forces into their constituent parts is useful for a final comparison of the topologies.

3.7.1 Topologies

Four topologies were investigated. Although the ultimate goal for this work was to implement the design in CMOS, the design work was to also provide designs for in-house fabrication, if it was necessary. Therefore, designs which are made up of only one layer were preferable to more those that make use of two or more. The explored topologies are titled “meander”, “omega”, “serpentine” and “spiral”. Top-down views of examples of the four designs are shown in figure 3.7. Brief introductions to each are given here, and what led to the investigation of each is explored in section 3.7.3 below.

A meandering pattern like that shown in figure 3.7 was discussed in [52] as being one of the best options for doing manipulation of magnetic beads in lab-on-chip devices. This served as the starting point for the SP module topology exploration. Results from this design suggested that a new topology should be considered which produced extra locations of high magnetic gradient. One way to accomplish this was to introduce the “omega” shape, which includes additional switch-backs where current flowing in opposite directions generates a high field gradient. After investigating the omega design it was clear that the trends were pointing to a simple serpentine design for maximizing

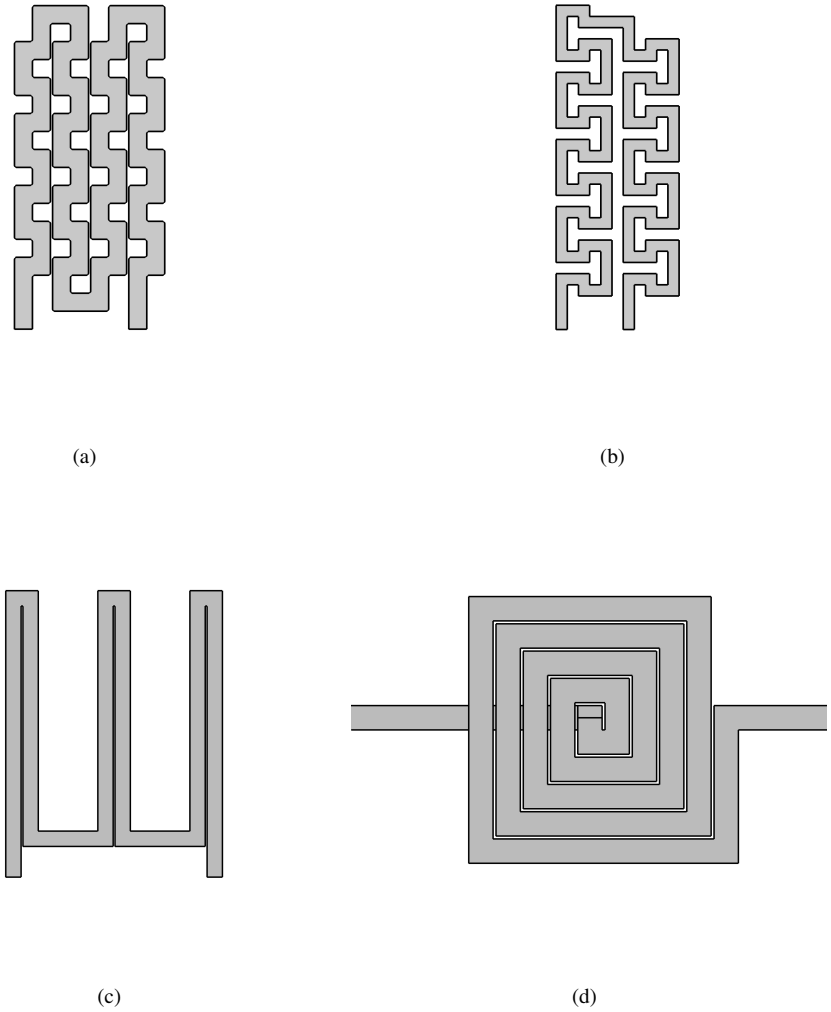

Figure 3.7: Four planar electromagnetic topologies. (a) Meander, (b) omega, (c) serpentine "pair", (d) 5-turn spiral. The four topologies here are not shown to scale to each other.

$\vec{F_{mx}}$ in one particular direction, so it was explored next. Finally, the square spiral design is known to be an excellent generator of magnetic fields, so it was explored as well.

3.7.2 Factors and Response Variables

In general, the experimental factors for these simulations were made up of dimensions for the characteristic units of each design (e.g., the dimensions of the square loop for the meander pattern). The metal track width was maintained at 15 µm. The response variables of the experiment were chosen to be the values of interest, $\vec{F_{mx}}$ or $\vec{F_{my}}$, and $\vec{F_{mz}}$. Since the main goal is to oppose flow with $\vec{F_{mx}}$ and $\vec{F_{mm}}$ is typically quoted in literature, these results are shown here. It was established that $\vec{F_{mz}}$ must reach a minimum of 0.1 pN, so this quantity is used in the final comparison table at the end of the chapter.

Finally, the two heights of interest are explored, 3 and 13 µm. A summary and comparison of the results is found in section 3.7.4.

3.7.3 Results and Discussion

3.7.3.1 Meander

The geometrical factor in this design is termed pattern's "gap" (G) size. A diagram (figure 3.8) shows which dimension is referred to as the gap in a simplified square-loop case. The gap size level was varied from 7.5 µm to 30 µm.

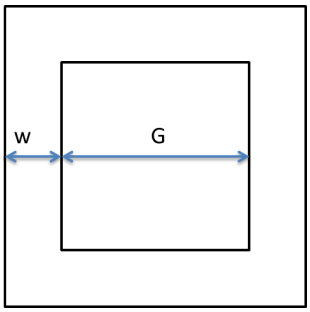

Figure 3.8: "Mesh" topology characteristic dimensions. Gap size (G) - the characteristic dimension of the meander pattern electromagnet. Also shown on the figure is the track width (w).

The 2D colour plot in 3.9 shows $\vec{F_{mx}}$ at the height of where the channel floor resides (3 µm), displaying locations of high x-direction force. The colour-map format clearly indicates the locations that one can expect the beads to be trapped.

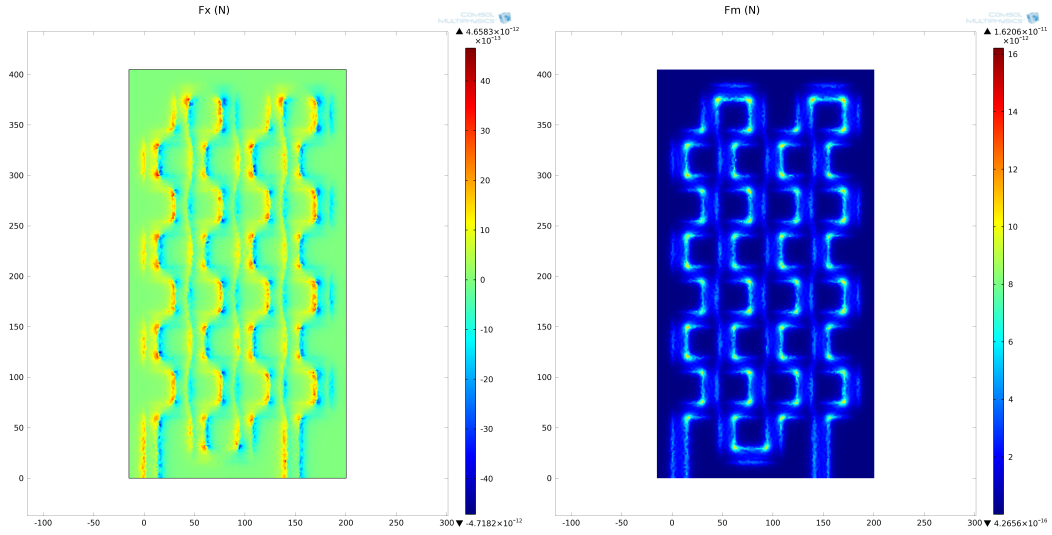

(a) $\vec{F_{mx}}$ (b) $\vec{F_{mm}}$

Figure 3.9: 2D plots of magnetic force in the $G = 30$ µm version of the meander model at a height of $z = 3$ µm. Dimension units on the x and y axes are µm. The plots of (a) $\vec{F_{mx}}$ and (b) $\vec{F_{mm}}$ serve to give an overview of the locations of highest value. Notice that there is a marked increase in magnitude at corners of the meander pattern.

Figure 3.10 displays the cutline used to extract the one-dimensional plots of figure 3.11. It was found that at a height of $z = 3$ µm, the smallest meander pattern with a gap size of 7.5 µm has the highest values for $\vec{F_{mm}}$ at up to roughly 5 pN. As the gap size increases, the peaks spread out but lose some magnitude. Separation of peak values could be useful if spreading the beads out is desirable.

The important take-away point from the information in the above plots is to note that the highest force locations are where gradients are highest (in the corners). This suggested further designs that introduce high gradients should be explored. One idea was to modify this meander pattern such that extra locations for high gradient are introduced. It is desirable to oppose flow in a single direction, so

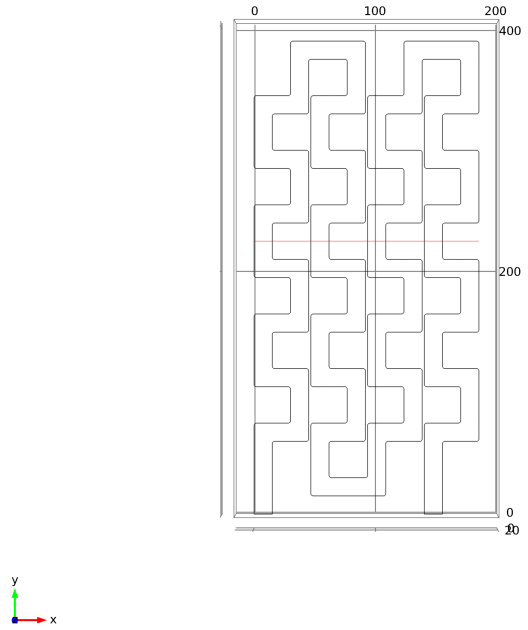

(a) Cutline at $z = 3\mu m$, through meander middle

Figure 3.10: A cutline (red) is shown in this figure which crosses the middle of the meander pattern characteristic unit ($G = 30\,\mu m$). The same cutline was drawn for each of the other meander iterations. Dimension units on the x and y axes are μm.

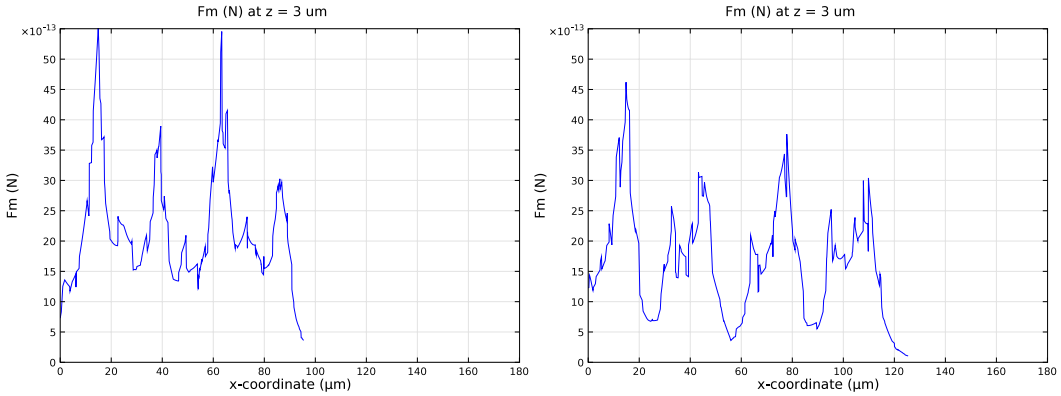

(a) $G = 7.5\mu m$ (b) $G = 15\mu m$

(c) $G = 22.5\mu m$ (d) $G = 30\mu m$

Figure 3.11: 1D plots of magnetic force in the "meander" topologies. $\vec{F_m}$ at $z = 3\,\mu m$ for each of the G factors measured.

these extra locations should be placed to generate force in that direction also. With this motivation, the "omega" pattern was introduced. Refer to section 3.7.4 for a summary and comparison of all the explored electromagnet topologies.

3.7.3.2 Omega

Stemming from the meander simulations which showed a trend towards maximizing force by introducing more high-gradient areas, a topology termed "omega" - after its characteristic omega character-like shape - was simulated. By tweaking the meander pattern such that there are more locations where current passes in opposite directions, there are more spots for high magnetic force to be generated.

The dimensions of interest in this design are termed gap-1 ($G1$) and gap-2 ($G2$), and are shown in a simplified rectangular diagram in figure 3.12. The $G1$ parameter defines the separation between traces of the omega loop in one transverse direction, and has a major impact on the gradient value obtained in the direction of interest. The $G2$ parameter defines the "width" of the omega-shaped loop.

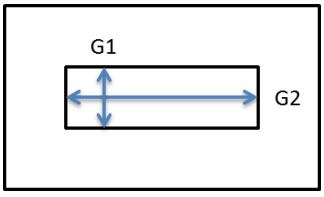

Figure 3.12: A simplified diagram of the characteristic rectangular loop of the Omega electromagnet topology showing the two parameters $G1$ and $G2$.

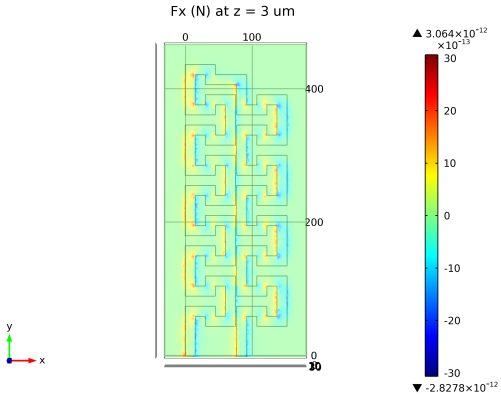

(a) Spacing = 1.8µm

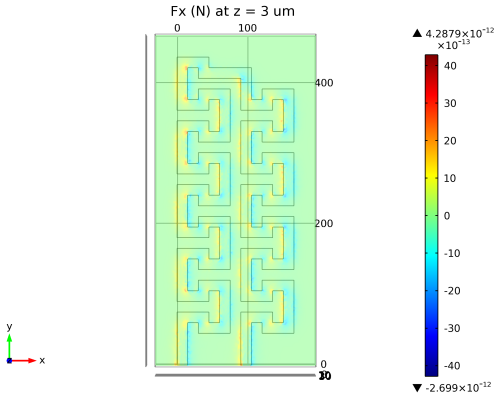

(b) Spacing = 15µm

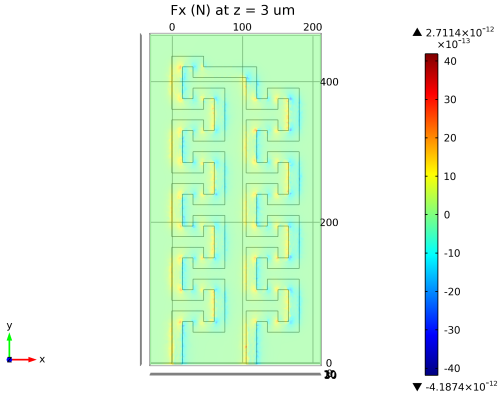

(c) Spacing = 30µm

Figure 3.13: 2D $\vec{F_{mx}}$ plots at $z = 3\,\mu$m for the three spacing levels of (a) 1.8, (b) 15 and (c) 30 µm. Dimension units on the x and y axes are µm.

At a height of $z = 3\,\mu$m it was found that there was a trend towards a smaller $G1$ parameter for

maximizing the force against flow. In figure 3.13 this is defined as the x direction. Very little change was observed by varying $G2$.

In summary, reducing the $G1$ value to its minimum of 2 µm appears to give the most significant advantage in producing a high $\vec{F_{mx}}$ value. Since varying $G2$ had little impact on the results, this parameter can be used to spread out the pattern if it turns out that too much Joule heating is taking place with a tighter configuration.

Similar to the meander pattern results, the conclusions made here point towards a plain serpentine pattern with minimal spacing to maximize the force opposing the direction of fluid flow. Therefore, the serpentine design was investigated next. Refer to section 3.7.4 for a summary and comparison of all the explored electromagnet topologies.

3.7.3.3 Serpentine

The serpentine configuration for electromagnets was put down as inferior to the meander pattern in [52]. However it was also found that cancellation of magnetic field reduced the effectiveness of the two earlier topologies. For this reason, a regular pitch serpentine model was created, and an additional "paired" serpentine design was also investigated. The purpose of the "paired" traces is to provide a region of high gradient while avoiding much of the cancellation that comes from aligning multiple traces closely side-by-side. The "paired" design constitutes pairs of wires (i.e., 2 wires) spaced minimally (1.8 µm) which are then spaced by a larger distance between the minimally spaced pairs.

The motivation for this set of simulations was to investigate whether the serpentine design is in fact a better solution for maximizing $\vec{F_{mx}}$ than the other planar electromagnet designs, contrary to the discussion in [52].

Two-dimensional models were done since the serpentine model is easily modeled this way. The results would be relevant as long as the regions of interest remain near the middle of the traces, and not at the ends of the serpentine where it has to turn back on itself.

Figure 3.14 shows a 2D picture of the model that was simulated. As usual, a current density of $2 \times 10^{10}\,\mathrm{A\,m^{-2}}$ was used (ten times the ten-year limit for our CMOS process), yielding a total current of 300 mA in the 15 µm wide wires.

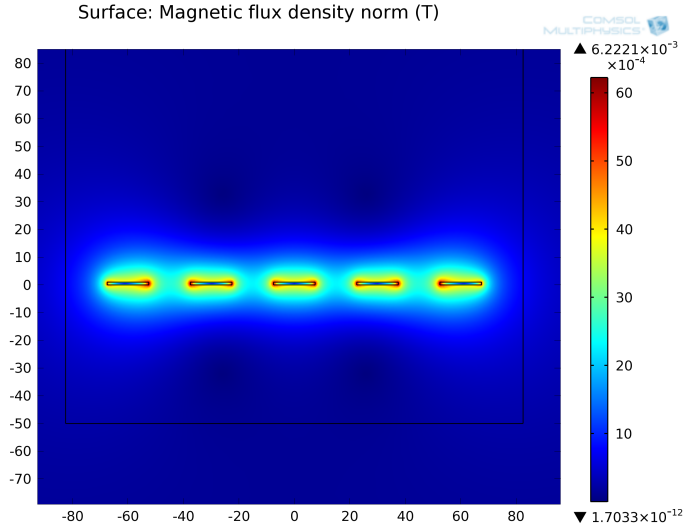

(a)

Figure 3.14: Magnetic flux density colour-map of the 2D serpentine electromagnet. The wires are of width and spacing of 15 µm, shown here by their cross section. This 2D simulation is performed in COMSOL Multiphysics. Dimension units on the x and y axes are µm.

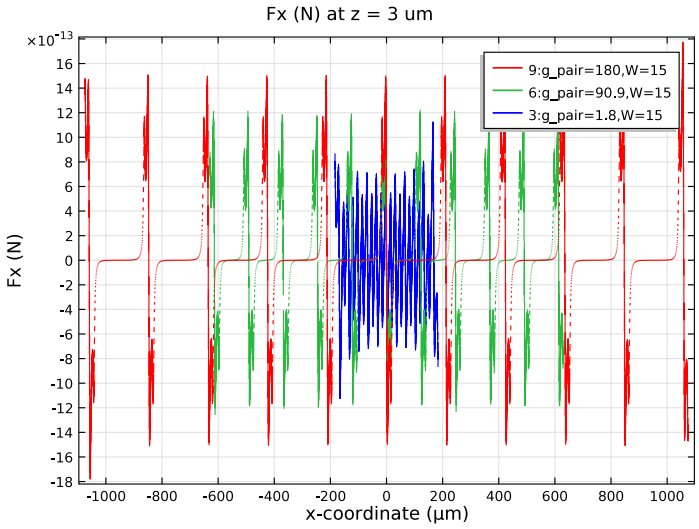

(a)

Figure 3.15: 1D plot of x-direction magnetic force for "serpentine" topology variations. $\vec{F}_x$ at $z = 3$ for three wire "pair" spacings (1.8, 90.9 and 180 µm). Wire width is 15 µm. Legend entries "3", "6", and "9" refer only to simulation parameterization indices and have no technical bearing on the results.

Figure 3.15 shows $\vec{F_{mx}}$ at $z = 3\,\mu m$ for three wire "pair" spacings of $1.8\,\mu m$, $180\,\mu m$ and one in between at $90.9\,\mu m$. The spacing between the pairs of wires is minimized to the CMOS Metal 3 layer specification of $1.8\,\mu m$, so the smallest pair spacing is actually an even pitch between all wires.

It was found that the serpentine model is in fact very good for producing a high $\vec{F_{mx}}$. Minimum pitch between paired wires maximizes the gradient while forsaking flux density. It should be noted that this concept could be useful if it was paired with an external permanent magnet; even a small permanent magnet overwhelms the flux produced by the electromagnets, and the combination of a high gradient (provided by the electromagnet) and high flux density (provided by a neodymium permanent magnet) would yield very high force terms. The larger the spacing between pairs of wires, the less cancellation of flux, and the higher the force term. Alternatively, high local field gradients could be generated by strategically placing highly permeable metals such as Metglas® to concentrate field lines. This idea is presented in section 5.3 as possible future work.

While the pair-spacing strategy may be useful, it is not practical for the CMOS work, since the planar space required (i.e., the separation between "pairs") is not worth the gains in $\vec{F_{mx}}$. For PCB-scale devices, however, it may prove to be quite useful, and this should be investigated further.

It is clear that it is not an efficient use of power to allow cancellation of flux lines, but such cancellation is necessary to produce a high gradient, which is imperative for achieving high force, since field strength is low at this scale. It would be beneficial, then, to go with a design that is additive in its field but also has regions of high gradient. This can be achieved with a spiral design. Refer to section 3.7.4 for a summary and comparison of all the explored electromagnet topologies.

3.7.3.4 Spiral

We wish to find the best topology for a planar electromagnet for doing bead manipulation against a flow. At least one group has used this design successfully in doing bead trapping and release [43]. Using spirals as planar electromagnets is not very common, since it requires at least two metal layers. With three metal layers in TDSI's CMOS, the spiral design lends itself well to the process.

The spiral inductor provides significant downwards force in the way of the theoretical square loop, and it also applies high field and gradient due to the parallel segments meeting antiparallel segments in the center. Moreover, two of these in series would yield a significant gradient between the two spirals, since current is passing in opposite directions.

A spiral topology allows for the magnetic flux to be additive - this is advantageous since it avoids the cancellation effects seen in all other designs to this point. This avoidance of cancellation yields a more efficient device for producing a functional magnetic field than one which shows lots of cancellation effects. Furthermore, there are intense gradients in the field at the center of the spiral, which combined with the higher field should yield the best combination to provide a high force on the beads for trapping. Finally, placing two square spirals side-by-side allows for a significant gradient between the two, if the spirals are oriented in the same way and current is flowing in the same direction.

As with all the other designs, this simulation adhered to the parameters of 300 mA in the 15 µm wide wires for a current density of $2 \times 10^{10}\,\mathrm{A\,m^{-2}}$ in Metal 3. Finally, the spacing was set to 1.8 µm, which is the minimum spacing for the CMOS process. A summary of these parameters is found in table 3.3.

Table 3.3: Parameters as COMSOL input for the planar square spiral simulation.

Parameter	Value	Description
W	15 µm	Wire width (CMOS dimension)
H	1 µm	Wire thickness (Metal 3 layer)
J_0	$2 \times 10^{10}\,\mathrm{A\,m^{-2}}$	Current density (ten times the ten-year current limit)
p	1.8 µm	Spacing between wires

Similar to other simulation experiments, the design was laid out in COMSOL and simulated using the 3D Magnetic and Electric Fields Interface. The geometry for the spiral electromagnet is displayed in figure 3.16. To extract force terms in regions of interest, a 2D planes were added as evaluation locations at heights of $z = 3$ and 13 µm.

The 2D colour maps of $\vec{F_{mx}}$, $\vec{F_{my}}$ and $\vec{F_{mz}}$ extracted by the cut planes are shown in figure 3.17. A tabulated summary of the force results found in the 5-turn spiral configuration is shown in table 3.4.

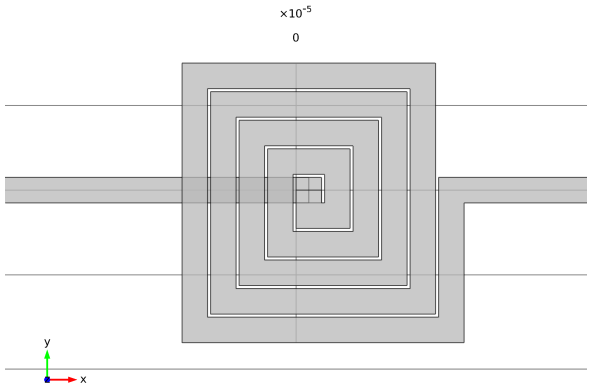

Figure 3.16: Geometry for the planar spiral electromagnet. The trace is 15 µm wide.

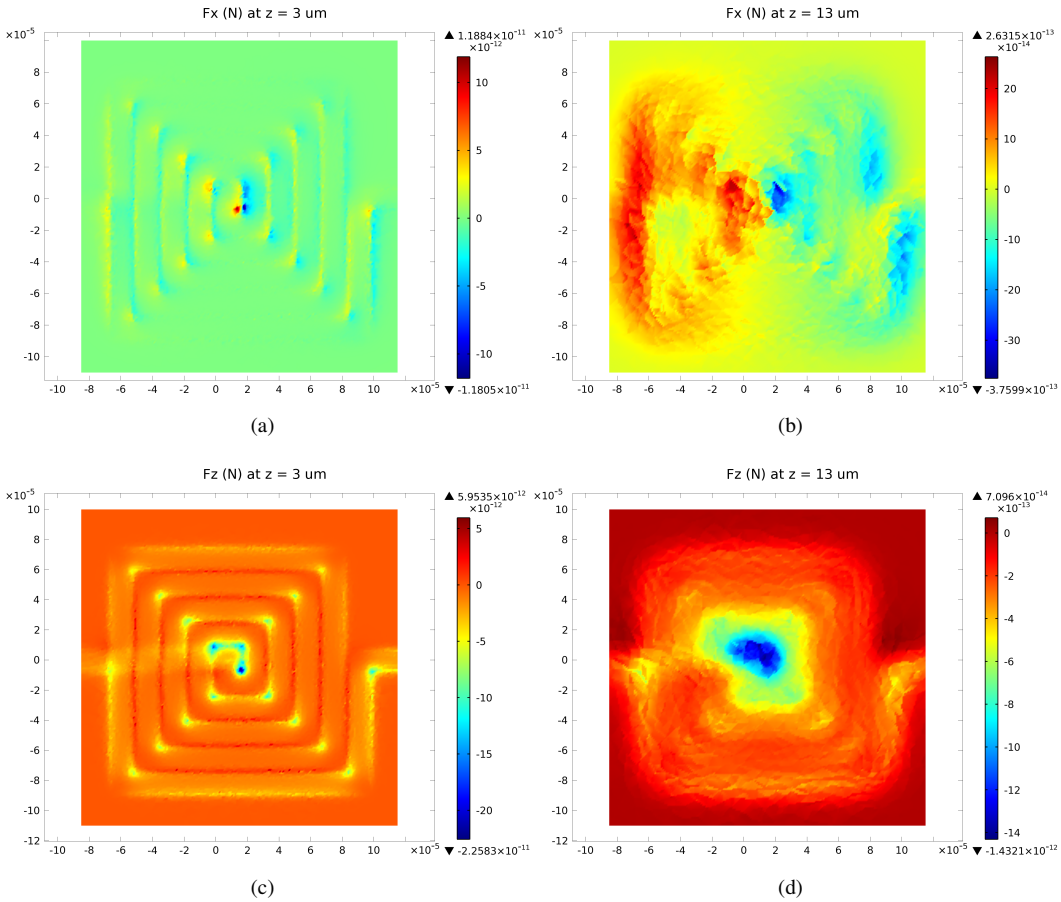

Figure 3.17: 2D colour-maps of magnetic force in the planar "spiral" electromagnet. $\vec{F_{mx}}$ at (a) $z = 3\,\mu$m, (b) $z = 13\,\mu$m, and $\vec{F_{mz}}$ at (c) $z = 3\,\mu$m, (d) $z = 13\,\mu$m.

Table 3.4: Summary of planar square spiral topology results. The first two rows show the force values obtained through simulation at the two heights of interest. The bottom two rows display the relative velocity associated with those forces given the equations derived earlier in section 3.4. Note that the $\vec{F_{mz}}$ is very high, and will allow the beads to be drawn downwards to the bottom of the channel very quickly. This is essential in the trapping mechanism, since forces increase greatly closer to the electromagnet. Conservative values are defined as the lowest simulated value of that parameter that a bead would experience in traversing the EM in the direction of flow.

Force Terms at Two Heights of Interest	$\vec{F_{mx}}$ **Conservative**	$\vec{F_{mx}}$ **Max**	$\vec{F_{my}}$ **Conservative**	$\vec{F_{my}}$ **Max**	$\vec{F_{mz}}$ **Conservative**	$\vec{F_{mz}}$ **Max**	$\vec{B_z}$
At $z = 3\,\mu m$	1.0 pN	11.8 pN	1.0 pN	9.6 pN	1.5 pN	22.6 pN	16 mT
At $z = 13\,\mu m$	0.15 pN	0.376 pN	0.15 pN	0.350 pN	1.1 pN	1.43 pN	-
$\vec{V_{rel}}$ Vertical at $z = 13\,\mu m$	-	-	-	-	$159\,\mu m\,s^{-1}$	$2391\,\mu m\,s^{-1}$	-
$\vec{V_{rel}}$ Flow at $z = 3\,\mu m$	$106\,\mu m\,s^{-1}$	$1248\,\mu m\,s^{-1}$	$106\,\mu m\,s^{-1}$	$1016\,\mu m\,s^{-1}$	-	-	-

Although the design is meant to maximize the field in the z-direction, the forces attained in the transverse plane are excellent for opposing flow. That is, the piconewton force range is obtained in the transverse directions ($\vec{F_{mx}}$ and $\vec{F_{my}}$) while maintaining at least 1×10^{-13} N or 0.1 pN in the vertical direction ($\vec{F_{mz}}$). With such a substantial vertical force, the beads will be drawn quickly down to the bottom of the channel ($\vec{V_{rel}} \approx 100\,\mu m\,s^{-1}$ vertically). At the bottom of the channel, the beads are at $z = 3\,\mu m$, and experience $\vec{F_{mx}} = 1 - 3$ pN, which would allow for a relative velocity of up to $\vec{V_{rel}} \approx 300\,\mu m\,s^{-1}$.

To conclude, it was found that a small spiral electromagnet (n = 5) produces fields and gradients sufficiently high to do bead separation from flow in a 10 µm high channel. Typical horizontal force (for opposing flow) and vertical force (for drawing the beads downwards) at $z = 3\,\mu m$ were found to be approximately 3 pN and 9 pN respectively, both at the centre of the spiral inductor. Similarly, the forces were found to be 0.2 pN and 1 pN for the horizontal and vertical forces respectively, at $z = 13\,\mu m$. Assuming beads are drawn down to the bottom of the channel by the significant vertical force (yielding a velocity of $\gtrapprox 100\,\mu m\,s^{-1}$ downwards), the relative flow rate achievable by this configuration would be approximately $300\,\mu m\,s^{-1}$.

3.7.4 Comparison of Electromagnet Topologies

A final comparison with tabulated results from each of the electromagnet topologies discussed above highlights that the spiral electromagnet offers the best opportunity for bead trapping against flow. The spiral electromagnet is capable of standing on its own as a viable option for integrated sample preparation on the system chip.

Table 3.5 shows that the spiral electromagnet yielded the best results for both $\vec{F_{mx}}$ and $\vec{F_{mz}}$ at $z = 3$ and 13 µm respectively (the most important quantities for doing bead trapping). Rough force values are entered for each design, and can be found on their associated plots from the simulation sections above. For all designs, wire width was set to 15 µm, and current density was held at $2 \times 10^{10}\,\mathrm{A\,m^{-2}}$ for a total current of 300 mA. Minimum spacing of the CMOS Metal 3 layer is 1.8 µm and bead radius and magnetic susceptibility were held at 0.5 µm and 0.5 respectively. For the volumetric flow rate calculation, the channel/chamber is assumed to be 10 µm in height to match the KMPR 1 layer, and the width is set to 500 µm.

Table 3.5: A tabulated summary of the results of the various electromagnet topologies studied in this work. Conservative values are defined as the lowest simulated value of that parameter that a bead would experience in traversing the EM in the direction of flow.

Topology	$\vec{F_{mx}}$(N) **at** $z = 3\,\mu$m **Opposing Flow**	$\vec{F_{mz}}$(N) **at** $z = 13\,\mu$m **Drawing Beads Down**	$\vec{V_{rel,x}}$ ($\mu\mathrm{m\,s^{-1}}$) **Max Relative Flow Rate**	$\vec{V_{rel,z}}$ ($\mu\mathrm{m\,s^{-1}}$) **Relative Flow Rate Down**	V_{vol} ($\mathrm{nL\,s^{-1}}$) **for** 500 µm **Wide Chamber**
Meander	1.0×10^{-12}	2.0×10^{-13}	105	21	0.53
Omega	8.0×10^{-13}	1.6×10^{-13}	85	17	0.42
Serpentine	7.0×10^{-13}	8.0×10^{-14}	74	8.5	0.37
Serpentine Pair	1.0×10^{-12}	2.3×10^{-13}	116	24	0.58
n = 5 Spiral (conservative)	1.0×10^{-12}	4.0×10^{-13}	106	42	0.53
n = 5 Spiral (max)	4.0×10^{-12}	1.4×10^{-12}	423	148	2.12

3.8 Experimental Results and Discussion

Ideally, the most successful simulated device (the square spiral) would be tested by flowing a bead solution through a polymer channel integrated with the CMOS. Due to the prototype turn-around schedule with our industrial partner, this infrastructure was not available for testing. In lieu of this important test, two experiments were performed to validate the modeling and conservative design methodology utilized in this work. The first was to qualitatively assess the spiral CMOS electromagnet by observing a free droplet of magnetic bead solution placed on top of the passivated CMOS and applying a current to the EM, described in section 3.8.1 below. The second experiment was to test a rapid-prototyped device acting as a stand-in for the CMOS module to verify the modeling method's efficacy. To make the stand-in device easier to work with than a tiny CMOS die, a credit-card sized printed circuit board serpentine electromagnet with polymer microfluidics was designed and modeled in the same fashion as the CMOS SP module. The same conservative assumptions for estimating the withstand-able flow rate (i.e., at what flow rate the beads would be "blown away" from the electromagnet by the fluid drag force) were used; this experiment and its results are described in section 3.8.2.

3.8.1 CMOS Spiral Electromagnet

A test chip including the spiral topology was produced by TDSI, dubbed ICKAAMP1 (magnetic preparation 1). Since there was no KMPR fluidic layer on these devices, the most successful device by simulation (spiral) is tested with a static droplet of the magnetic beads in water. Again, the CMOS wires visible in figure 3.18 is covered in a layer of transparent silicon nitride passivation, $0.9-1\,\mu m$ in thickness. Since CS beads were used to populate the parameters for the simulations, they were used for the experiments described in this section.

3.8.1.1 Bead Preparation

ChargeSwitch beads are sold at a concentration of $25\,mg\,ml^{-1}$ [48], which is far too concentrated to perform a visual test, since all the experimenter would see is total coverage of the electromagnet with beads. The CS beads were diluted 1:1000 in DI water to facilitate the viewing of the bead collecting mechanism of the spiral electromagnet.

3.8.1.2 On-Chip Testing

The CMOS die was placed on a probe station (Wentworth) and the contact pads were connected to a power source set in current-control mode at a level of 300 mA. After placing the droplet of beads in water on the die, the power supply was engaged and the beads were filmed as they were pulled down to the top of the passivation.

Figure 3.18 summarizes the simulation and experimental results concisely. Figure 3.18(a) shows $\vec{F_{mm}}$ with its full scale, ranging up to 23 pN. However, it may be only very few elements reaching that value, so an adjusted scale where all values above 10 pN are given the same colour is shown in figure 3.18(b). The 8-turn electromagnet of the MP1 test chip is imaged in (c) prior to the bead test and (d), after the beads have been drawn down and the water dried.

Figures 3.18(b) and 3.18(d) highlights the similarities between the simulation of $\vec{F_{mm}}$ and the experimental result. It was observed that there is a greater number of beads collected in the locations where $\vec{F_{mm}}$ is highest in simulation.

3.8.2 Conservative Design Method Validation

The goal of the work described here in chapter 3 was to design, build and test an electromagnet suitable as part of a sample-preparation module for the CMOS platform system chip ICKAAL12. This module was to be capable of doing a final-step, on-chip sample concentration immediately prior to elution to the PCR chamber.

A rapid-prototyped device was prepared as a proxy for the electromagnetic CMOS SP module. To facilitate handling, the stand-in device was constructed at a larger scale. A serpentine electromagnet was fabricated as a printed-circuit board (PCB), and dry-adhesive polymer microfluidic infrastructure was used for the fluidic interface [66]. This device was designed and modeled in the same fashion as the CMOS module of interest, and therefore was to act as a validation of the FEM procedure and conservative design estimations.

3.8.2.1 Design of Experiment

For a magnetic bead to become trapped and then withstand a given flow rate value, an associated magnetic force must be applied to oppose the fluid drag force and hold the magnetic beads pinned.

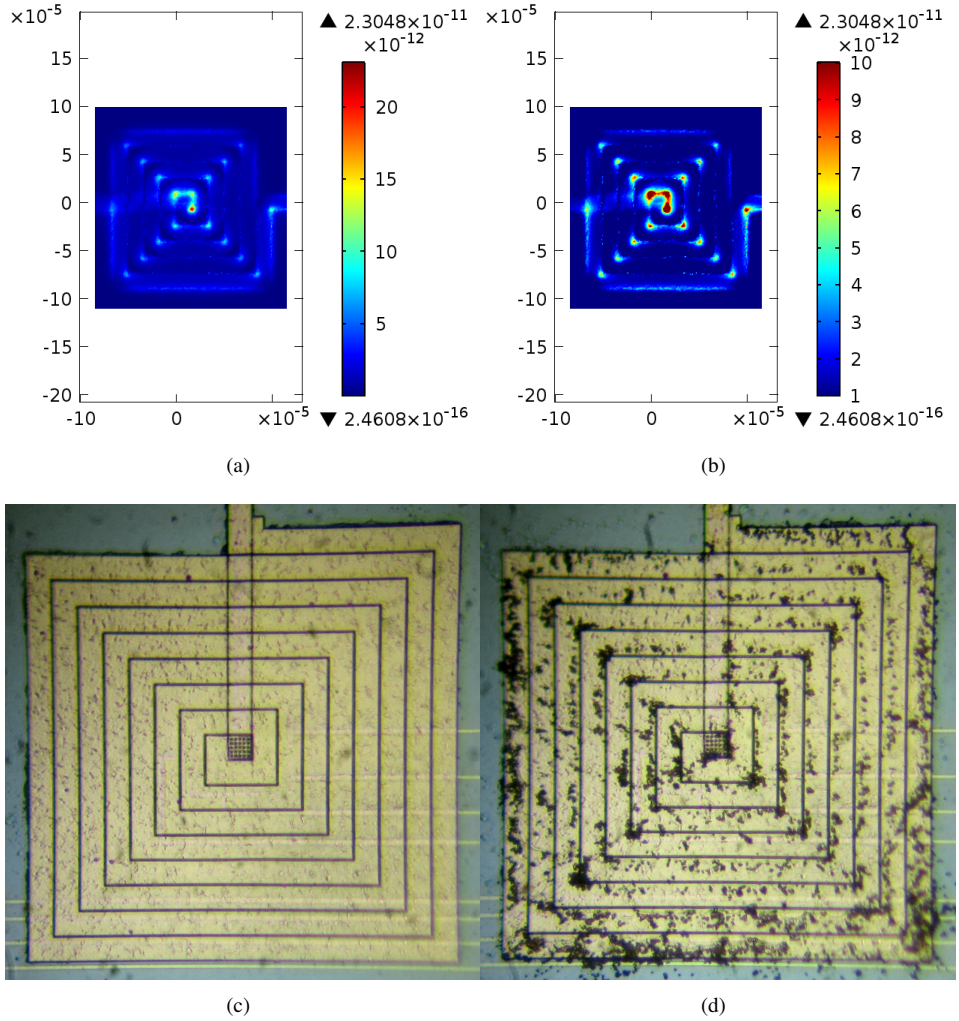

Figure 3.18: (a) $\vec{F_{mm}}$, (b) $\vec{F_{mm}}$ with an adjusted scale in which all values above 10 pN display the same deep red colour to make areas of high trapping force more visually clear, (c) 8-turn square spiral electromagnet on ICKAAMP1 prior to the bead test, (d) the same square spiral after pulling beads out of a solution.

Many assumptions were made throughout the design approach, as detailed in section 3.5. The rapid-prototyped PCB system described here serves to demonstrate whether the approach used for modeling the electromagnetic system for implementation in ICKAAL12 is sufficient to meet and exceed a target flow rate.

Objective The objective of this quantitative experiment was to determine if the approach outlined in section 3.5 is sufficient to estimate a minimum fluid flow rate from which beads could be pulled down and pinned to the channel floor. If the device can apply a magnetic force such that beads can withstand a greater flow rate than what was estimated, then the application of conservative considerations done here can be deemed a successful approach. If the device fails to hold beads against the estimated flow rate (i.e., a lower-than-estimated flow rate blows the beads away), then the design method used in this thesis is not sufficient in its current state for designing a magnetic bead-trapping system for microfluidics.

Materials and Methods A credit-card sized PCB (85.60 by 53.98 mm) was designed in 1 oz copper (standard thickness of 35.56 µm) with a serpentine trace of minimum allowable dimensions and pitch (width and spacing of 177.8 µm). The PCB was manufactured by AP Circuits®. Rapid-prototyped polymer fluidics were adhered to a UV-cure acrylic (Loctite®3525) that coated the PCB trace, planarizing the PCB and acting as a channel floor. Metal fluidic interconnects were used to feed bead solutions to the channel running over the serpentine traces in a perpendicular direction. These metal interconnects were $1/16$" diameter brass tubes from K&S Precision Metals (stock number 8125), and they were epoxied to holes drilled into the PCB.

A DC power supply (National Instrument PXI 4110) was used to provide the 1 A to the PCB. Three legs of the serpentine were powered (*i.e.*, the serpentine trace follows two switchbacks between the power connections), though many were included in this prototype. A syringe pump (Harvard Apparatus, PUMP 11 Pico Plus ELITE) was used in inject-mode to induce the fluid flow. An optical microscope (Basler acA2000-50gc) equipped with a 20X objective was used to record bead tests. Beads with a well-established magnetic susceptibility were used for the test to remove an additional unknown variable; the MyOne Dynabeads were selected for this effort (relevant properties listed in table 3.2). Refer to figure 3.19 for a photograph of the experimental setup.

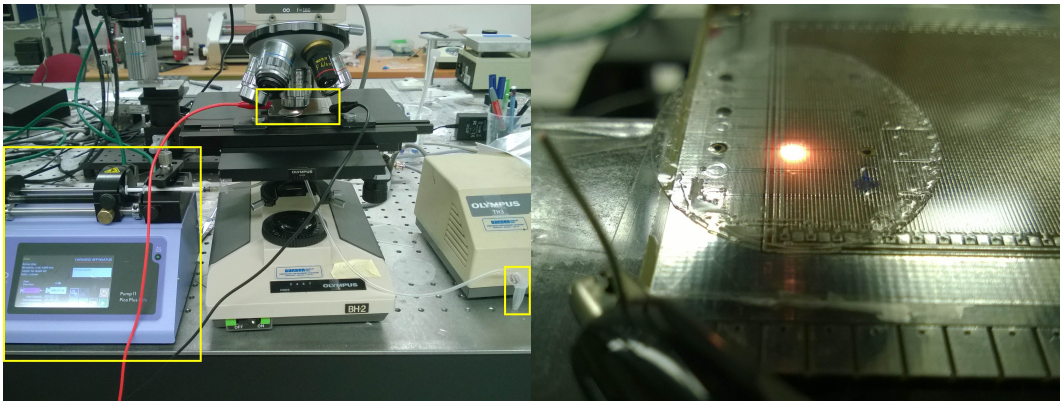

(a) (b)

Figure 3.19: PCB prototype experimental setup. (a) The Harvard Apparatus syringe pump (left), prototype on the microscope stage (middle top) and magnetic bead solution (right). (b) A close-up of the PCB electromagnet and dry-adhesive polymer microfluidics on the microscope stage.

Factors, Levels, Response To meet the objective described above, only one factor is necessary - the applied flow rate. By holding all other factors constant and modeling the system based on selected levels, the simple question of whether the conservative design method allows an estimate of a minimum expected flow rate can be answered.

As the independent variable, the applied flow rate level will be reduced by regular intervals from a value much higher than the expected withstand-able flow rate. The flow rate at which beads can be drawn down, pinned, and held against the drag force is the quantity of interest.

A COMSOL model is used to estimate the x-direction magnetic force at the channel floor; figure 3.21. The minimum expected flow rate is calculated by equating this force (24 fN) to fluid drag and solving for the fluid velocity given the channel dimensions and other parameters, all listed in table 3.6. All equations necessary to perform these calculations are presented in section 3.4.

Using equations (3.14), (3.15), and (3.26) with the dimensions of the channel (table Table 3.6 on page 57), the expected volumetric flow rate can be estimated to be 31.9 nL min^{-1}:

Table 3.6: Rapid-prototyped PCB/dry-adhesive electromagnetic microfluidic platform input parameters for flow rate calculations. For information on calculating the hydraulic diameter and non-circular coefficient, refer to sections 3.4.4.2 and 3.4.5.1, respectively.

Parameter	Value	Description
H	2.8×10^{-5} m	Channel height
W	2×10^{-4} m	Channel width
L	1.5×10^{-2} m	Channel length
A	5.6×10^{-9} m^2	Channel cross section area
D_H	4.91×10^{-5} m	Hydraulic diameter
λ_{NC}	1.28	Non-circular coefficient
r	0.5×10^{-6} m	Radius of the magnetic bead
μ	1×10^{-3} N s m^{-2}	Dynamic viscosity of the fluid medium

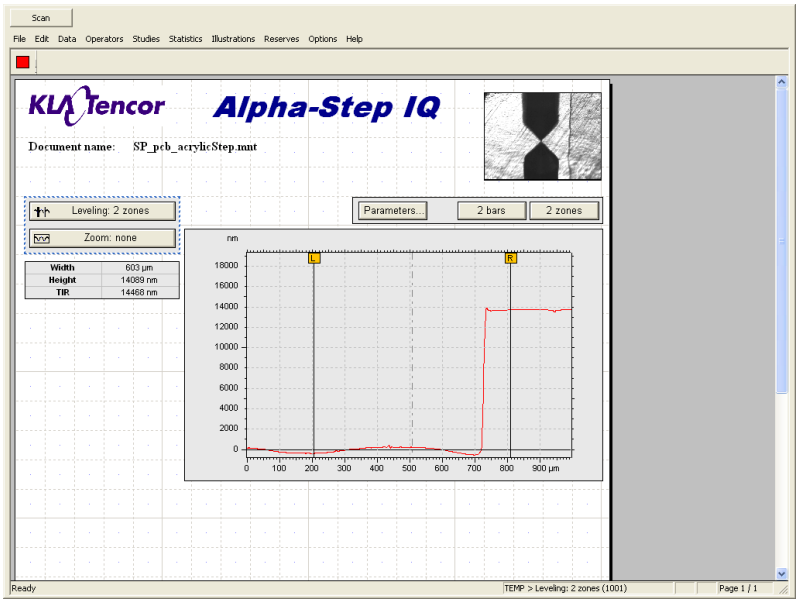

Figure 3.20: PCB prototype channel floor thickness measurement. A profilometer was used to measure the step height of PCB-to-UV-cure acrylic used as the channel floor. The UV-cure acrylic was measured to be of 14 µm thickness. Practically, this measurement represents the distance between the channel floor and the current-carrying traces making up the electromagnet. This is an important quantity for an accurate simulation.

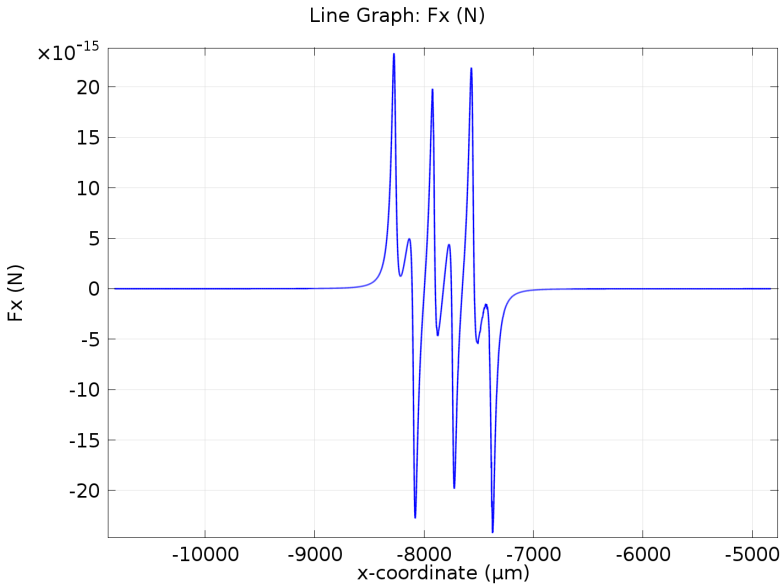

Figure 3.21: PCB prototype simulated results. $\vec{F_x}$ at the channel floor above a serpentine trace with three legs (two turns).

$$\vec{F_{mx}} = \vec{F_d}$$

$$\vec{F_{mx}} = 6\pi\mu v_{rel} r$$

$$2.4\times10^{-14}\,\mathrm{N} = 6\pi(1\times10^{-3}\,\mathrm{N\,s\,m^{-2}})v_{rel}(0.5\times10^{-6}\,\mathrm{m})$$

$$v_{rel} = 2.54\times10^{-6}\,\mathrm{m\,s^{-1}}$$

Where v_{rel} is the relative velocity of the fluid front at the height of the bead in the channel (*i.e.*, 0.5 µm). Couette's parallel plate approximation yields the max velocity from this value:

$$v_{max} = v_{(y)}\frac{\mathrm{H}}{y}$$

$$v_{max} = 2.54\times10^{-6}\,\mathrm{m\,s^{-1}}\frac{2.8\times10^{-5}\,\mathrm{m}}{0.5\times10^{-6}\,\mathrm{m}}$$

$$v_{max} = 142\,\mu\mathrm{m\,s^{-1}}$$

Then the average relative velocity in the channel is $v_{avg} = \frac{2}{3}v_{max} = 94.8\,\mu\mathrm{m\,s^{-1}}$. Knowing the dimensions of the channel, the volumetric flow rate is:

$$v_{vol} = (v_{avg})(A)$$
$$v_{vol} = (94.8 \times 10^{-6}\,\mathrm{m\,s^{-1}})(5.6 \times 10^{-9}\,\mathrm{m^2})$$
$$v_{vol} = 5.31 \times 10^{-13}\,\mathrm{m^3\,s^{-1}}, \text{ or } 31.9\,\mathrm{nL\,min^{-1}}$$

Experimental Procedure Volumetric flow rate was decreased from well-above the rough expected level to below the expected level in order to identify the rate at which the entire column of beads became trapped. This procedure was repeated with consecutively smaller flow rate steps until a value with $1\,\mathrm{nL\,min^{-1}}$ precision could be determined.

3.8.2.2 Results

It was found that the volumetric flow rate upper limit was $50\,\mathrm{nL\,min^{-1}}$. At this flow rate, all beads were trapped within the three traces (visually confirmed with the microscope). Single beads were observed to become pinned until power (current) was removed, at which point they became unstuck and continued with the fluid flow. Beads were also observed to begin to chain together, though this behaviour was not considered as part of the design calculations.

3.8.2.3 Discussion

The expected minimum flow rate at which beads could be captured and held against flow was calculated to be $31.9\,\mathrm{nL\,min^{-1}}$ per Couette's equation. It was found by experiment that this flow rate could be achieved and exceeded to the level of $50\,\mathrm{nL\,min^{-1}}$. Per the objective, since the conservatively-designed device can apply a magnetic force such that beads can withstand a greater flow rate than what was estimated, the design-method used here appears to be a successful approach.

There is room for improvement in the model; the percent difference between the simulated and experimental results is 44%. Sources of error could include the bead magnetic susceptibility (as shown earlier, there is disagreement in literature), channel dimensions (deformation of the polymer microfluidics during fabrication), thickness of the UV-cure acrylic planarization layer over the PCB traces (variability), and dimensions of the PCB traces (and therefore current density and electromagnetic field). These parameters, however, would be well-defined in an industrial

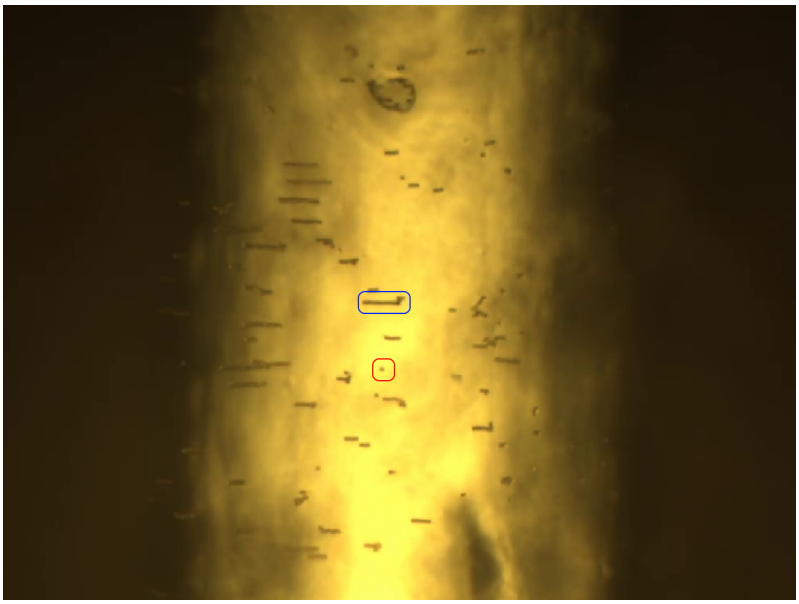

Figure 3.22: Trapped beads at a flow rate of $50\,\mathrm{nL\,min^{-1}}$. This was the maximum volumetric flow rate at which all beads could be captured within the three traces. An example of a trapped single bead is shown encircled in red, and an example of trapped chained beads is shown encircled in blue. PCB traces are not perfectly rectangular, but are instead curved on the top. This is why the "edges" of the trace appear to blend into the gaps instead of being sharp.

fabrication settings, removing those sources of error.

Much of this error will also be mitigated if the design method is used in a "forward" sense, *i.e.*, the flow rate is selected and *then* an electromagnet is designed to achieve the necessary opposing force. The reason for this is that there will be a known expected channel pressure. This is one of the parameters in the Plane-Poisseuille flow equation (equation (3.27)). We can demonstrate this improved accuracy by using the calculated channel pressure (using equation (3.23)) from this prototype situation and use it in the same estimation from above. Using Plane-Poisseuille instead of Couette yields $v_{vol} = 46.8\,\mathrm{nL\,min^{-1}}$, which yields a percent difference from the measured value of 7%.

This experiment served to validate the method for designing an electromagnet for sample preparation described in section 3.8.2. With the efficacy verified, in the next section some final information is provided on the system chip (ICKAAL12) SP module, including decisions for integration with other system components.

3.9 Integrated Microfluidic-CMOS Chip ICKAAL12

3.9.1 Design Decisions for the SP Module on L12

The spiral design showed the best performance of the electromagnet topologies investigated. Whether an external field is added, or not, the spiral can stand alone as a useful component of the system chip's SP module.

Due to computational constraints, the number of turns for the simulated spiral (5) was lower than what would be possible (given space and power constraints) in the system chip; this is significant in that the values found by simulation are yet another conservative case. With an easy extrapolation from the theory presented in section 3.6.2, one can see that multiple concentric square loops will increase the field produced by the electromagnet, assuming the current is flowing in the same direction in each of the loops, since the fields are additive. The greater number of turns, the greater the field. Of course, as the length of the spiral increases, so does the total resistance of the path, and there are power and space constraints to consider for the system chip.

Since the maximum applicable voltage on the system chip is 5 V, to achieve 300 mA current (maximizing current density to $2 \times 10^{10}\,\mathrm{A\,m^{-2}}$, or ten-times the ten-year lifetime limit) the maximum allowable resistance of the coil is $16\,\Omega$. We can use this constraint to find the maximum number of turns that can be supported by L12. This constraint can then be compared to the space allocated for the SP module, which was not known through the design process, since the chip layout was not yet complete. An engineering tradeoff will have to be made to weigh planar space against the number of desired spiral turns.

For the TDSI process Metal 3 layer, the upper bound for sheet resistance variation is $51\,\mathrm{m\Omega\square^{-1}}$. Since we know the width of the path (15 µm) and the total target resistance ($16\,\Omega$), we can calculate the total length to generate $16\,\Omega$.

$$L_{path} = \frac{W_{path} R_{spiral}}{R_{M3}} = \frac{(15 \times 10^{-6}\,\mathrm{m})(16\,\Omega)}{51 \times 10^{-3}\,\Omega\square^{-1}} = 4.71 \times 10^{-3}\,\mathrm{m}$$

Given the minimum gap size in Metal 3 (1.8 µm) the total path length can be added as the spiral is traced from the center outwards. Thirty-two segments reaches a length of 4541 µm, which is 8 turns. This is exactly the size of one of the spirals that was tested in ICKAAMP1, images shown in figure 3.18. The dimensions of an 8 turn spiral are 267 µm by 282 µm, and the design included on ICKAAL12 is shown in figure 3.23.

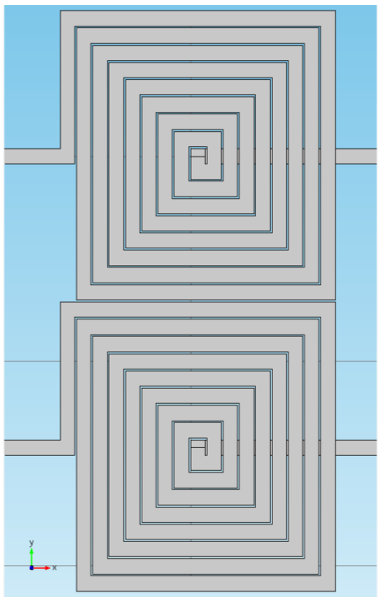

(a)

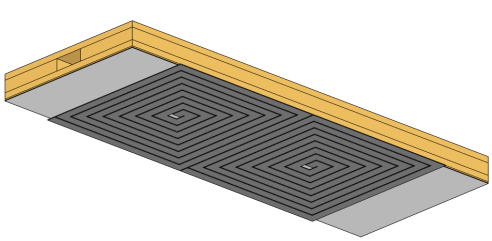

(b)

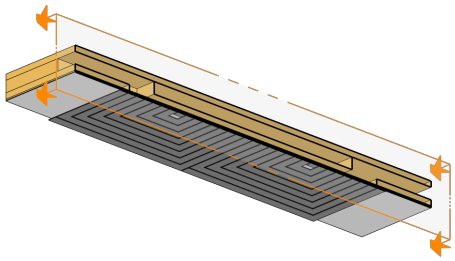

(c)

Figure 3.23: 3D model images of the dual $n = 8$ (8 turn) spiral electromagnets. (a) COMSOL model of the system to be implemented in ICKAALC12. (b) Dual spiral EMs integrated with the KMPR layers that would make up the microfluidic portion of the lab-on-chip ICKAALC12. (c) A cutplane shows how the fluidic channel drops down to enable the SP chamber to be closer to the electromagnets.

As the design of ICKAAL12 came together, the area allocation for the SP module was restricted to 290 µm by 570 µm. Since the largest dimension of the $n = 8$ spiral is 282 µm this area allocation did not disrupt the design. In fact, there was room for two spirals positioned side-by-side (564 µm). Simulation showed that there was negligible impact on the typical and maximum force values for $\vec{F_{mx}}$ with this positioning. Additional flexibility is provided by having two of the spirals beside one another - for example, the flow of the sample could be directed over both simultaneously, effectively doubling the volumetric flow rate of the device. Alternatively, if the flow is directed such that the EMs are positioned serially (with respect to fluid flow direction), then an externally applied magnetic field would induce a significant force on the line between the two square spirals, since there will be an intense gradient there.

As stated earlier, the spiral EM cannot yet be tested against a fluid flow. However, given the conservative design considerations discussed in section 3.5, there is every indication that the SP module will perform bead trapping as a standalone module.

3.9.2 Performance Estimates for the SP Module on L12

A review of estimates for the performance of the system is presented here:

- The typical and maximum force ($\vec{F_{mx}}$(N) at $z = 3\,\mu$m) values for the $n = 5$ square spiral electromagnet were found by simulation to be 1 pN and 4 pN respectively.

- The effective volumetric magnetic susceptibility (χ_v) for the ChargeSwitch beads is not available, and a conservative value of 0.5 was selected. Other 1 µm sized magnetic sample preparation beads with a different functional surface (MyOne Dynabeads) have an effective χ_v of 1.5. If the effective volumetric magnetic susceptibility ranges between these two values, then the force would scale accordingly as a range. Typical range of $1-3$ pN and maximum value range of $4-12$ pN.

- The typical and maximum force ranges of $1-3$ pN and $4-12$ pN constitute $\vec{V_{rel}}$ ranges of $106-317\,\mu\text{m}\,\text{s}^{-1}$ and $423-1269\,\mu\text{m}\,\text{s}^{-1}$ respectively.

- For the fastest sample processing time, an SP chamber of height and width dimensions $h = 10\,\mu$m and $w = 564\,\mu$m would be implemented for the configuration in which flow is

directed across two spiral EMs in parallel. In this case, the typical and maximum $\vec{V_{rel}}$ ranges would yield volumetric flow rate ranges of $0.6-1.9\,\mathrm{nL\,s^{-1}}$ and $2.4-7.2\,\mathrm{nL\,s^{-1}}$ respectively.

- The typical and maximum V_{vol} ranges of $0.6-1.9\,\mathrm{nL\,s^{-1}}$ and $2.4-7.2\,\mathrm{nL\,s^{-1}}$ would process a 1 µL volume sample in the ranges of roughly $9-28\,\mathrm{min}$ and $2-7\,\mathrm{min}$ respectively.

- Additionally, according to the Poiseuille equation (equation 3.27), given the SP chamber dimensions above, the fluid velocity in the middle of the channel would be approximately five times greater than the velocity at the height of the middle of a pinned bead. As an example, for a maximum relative flow rate in the middle of the channel of $1000\,\mathrm{\mu m\,s^{-1}}$, the fluid velocity inducing a drag force on the bead would be only $190\,\mathrm{\mu m\,s^{-1}}$.

- Finally, if a small external field (e.g., $0.05-0.1\,\mathrm{T}$) is applied, then even the shortest test times above would be improved, and even with the conservative estimate of 0.5 for the susceptibility, the time range to process 1 µL (given the same SP chamber as above) of sample is reduced to $1.4-5.6\,\mathrm{min}$. Given the MyOne Dynabeads susceptibility of 1.5, that time range reduces to $0.5-1.9\,\mathrm{min}$.

Applying these estimates to an example diagnostic process helps to demonstrate which parts of the SP process still require significant research before a fully integrated approach can be realized.

3.10 Example Diagnostic Process - Purification of gDNA from a Buccal Swab

It can be difficult to imagine exactly how the technical advancements described in this section can be applied in real life. To illustrate how the sample preparation module on L12 could be used, an example diagnostic process is presented here.

A "buccal swab" is a common way to collect cells from the inside of a patient's cheek. The application described here is the isolation of genomic DNA (gDNA) from a buccal swab using ChargeSwitch bead technology (Invitrogen ChargeSwitch gDNA Buccal Cell Kits [67]).

A buccal swab cannot simply be placed onto the L12 chip - pre-processing is necessary to interface this macro-scale collection of sample to the micro-level that a CMOS platform could handle. Although the focus of this work is on the micro-scale portion of the SP processing, this

buccal swab example helps to flag the chip-to-world interfacing issues that must be solved in future work.

Refer to table 3.8 for a summary of the example diagnostic process for a buccal swab sample preparation. Calculations in this section also adhere to the constraints summarized in table 3.7. Finally, it is important to note that this procedure implements a modified version of the protocol in that it keeps the same reagent concentrations and scales the total volume of the last three steps (purified sample, washing, elution) by a factor of ~10 000. It is not specified what percent carry-over of wash buffer is acceptable as part of the elution step (to avoid causing PCR issues), but in general, Invitrogen recommends ratios of ~10:1 of sample to elution volume and ~2:1 of wash buffer to sample volume in the ChargeSwitch protocols, so those criteria are followed here. Even if all of the dead volume in the channels between the SP and PCR chambers makes it into the PCR reaction, it would make up only about 6% of that volume, which is expected to be acceptable based on previous experience.

Table 3.7: Calculations in the following section adhere to the constraints summarized in this table.

Parameter	Value	Description
Sample Preparation Chamber Dimensions		
Height	10 µm	Chamber height.
Width	564 µm	Chamber width.
Length	282 µm	Chamber length.
Volume	1.59 nL	Chamber volume.
PCR Chamber Dimensions		
Height	20 µm	Chamber height.
Radius	500 µm	Chamber radius.
Volume	15.7 nL	Chamber volume.
Electromagnetic Parameters		
$\vec{F_{mx}}$ at channel bottom	1 pN	Magnetic force opposing fluid drag on a bead pinned to the channel floor.
V_{rel} at channel bottom	106 µm s^{-1}	Relative velocity of fluid.
χ_v for CS bead	0.5	Volumetric magnetic susceptibility of ChargeSwitch beads.

3.10.1 Lysis

Sample lysis is one part of the process that could be integrated into a handheld system's macro-scale infrastructure. A buccal swab is taken from the inside of a patient's cheek and the sample is immersed in 1 mL of a "lysis mix" in a small microcentrifuge tube. The lysis mix is made up of a proprietary lysis buffer and proteinase k (an enzyme to break down cell structures to release the DNA). Invitrogen's protocol recommends a 20 min incubation period at 37 °C for full lysis of a buccal swab sample. It is possible, however, that this time could be reduced if smaller sample and lysis volumes were used. Research would be necessary to determine what time reductions, if any, could be achieved with smaller processing volumes.

Upon completion of the lysis incubation, the released DNA can be bound by the CS beads.

3.10.2 Purification

The binding-of-DNA step (purification) is another opportunity for macro-scale integration into a hand-held device. Once DNA is bound to the beads, significant reductions in volume take place, since beads can be magnetically collected into a small volume. In the typical macro-scale protocol, the digested supernatent (i.e., the liquid) from the lysis step is transferred from the tube containing the buccal swab to a new, sterile microcentrifuge tube. 140 µL of "purification mix" is added to the supernatent and the volume is agitated gently. Purification mix is made up of a proprietary purification buffer (pH < 6.0) and the magnetic ChargeSwitch beads. The acidic solution causes the beads to have a positive charge, effectively attracting negatively charged DNA out of the sample - 1 min is recommended to achieve full isolation of DNA out of the sample volume.

Beads are then magnetically collected at the base of the tube for 1 min using a permanent magnet. The remaining supernatent is discarded, leaving a pellet of DNA-bead conjugates. This pellet would typically be resuspended in the next step (washing), but at this point, the sample is concentrated enough to be used as an input on the integrated microfluidics-CMOS system.

3.10.3 Transfer to Chip

Since this step is where the protocol departs from the established method and enters research space, protocol ratios should be reviewed.

In diagnostic protocols, processing volumes can be scaled up and down to accommodate the

amount of sample in question. The ratios of ingredient volumes, however, should remain the same. Of course, the very small volumes associated with microfluidics have not been researched extensively, and there are competing factors that may reduce efficiency at these scales. For the purposes of this example, ingredient ratios are maintained with the knowledge that future experimental results may show that the ratios should be broken to improve processing (in ways such as improved DNA collection or PCR efficiency, for example).

The adjusted protocol for on-chip processing starts with the bead-DNA sample being loaded onto the chip along with the wash buffer and PCR mix (the elution buffer combined with polymerase and other reagents). Of this microlitre-scale volume of sample, 150 nL is pumped into the SP chamber and immobilized by the active electromagnet module (about 4 min). Refer to figure 3.24(a) for a schematic presenting how this step would be actuated on-chip.

3.10.4 Washing

Protocol ratios dictate that the "wash" should be twice the volume of the sample, so 300 nL of wash buffer (pH = 7.0) is flowed through the SP chamber to clear out unwanted cellular debris from the bead-DNA conjugates (8 min 22 s). Refer to figure 3.24(b) for a schematic of how this step would be actuated on-chip.

The cleaned DNA sample is now ready to be eluted into the PCR chamber for amplification.

3.10.5 Elution

Again following protocol ratios, the PCR volume should amount to one-tenth of the bead/sample volume, equating to 15 nL of elution buffer (pH = 8.5) and other necessary ingredients for PCR (e.g., polymerase). The basic pH of the elution buffer causes the CS beads to lose their positive charge and the DNA is released, which is then carried with the PCR mix into the PCR chamber for amplification (25 s), ending the SP process. Refer to figure 3.24(c) for a cartoon of how this step would be actuated on-chip.

A tally of the time to complete each of the on-chip steps above comes to 12 min 58 s. The pre-processing steps including lysis and incubation sums to 22 min, though as stated earlier, it may be possible to reduce this pre-processing time by further integrating the steps in a new low-volume process as part of the chip-to-world interface.

Finally, as discussed in section 3.9.2, these calculations are done conservatively by using a low

magnetic susceptibility value of $\chi_v = 0.5$. If a similar protocol is followed for a different 1 µm diameter magnetic bead with the same magnetic properties as the MyOne Dynabead ($\chi_v = 1.5$), then the theoretical diagnostic process would be as presented in table 3.9. The on-chip processing time would be reduced from 12 min 58 s to 4 min 20 s.

Table 3.8: Summary of an example diagnostic process for a buccal swab sample preparation. Off-chip pre-processing amounts to 22 min and the on-chip SP sums to just under 13 min. It is possible that reductions in pre-processing time could be gained by integrating those functions as automated chip-to-world infrastructure on a handheld device.

SP Step	Volume	Processing Time	Integration	Notes
Collection	N/A	N/A	No	Dependent on assay of interest.
Lysis	1 ml	20 min	No	Incubation at 37 °C.
Purification	140 µl	2 min	No	Binding the DNA, collecting the beads.
Transfer to Chip	150 nl	4 min 11 s	Yes	Drawing sample into the SP module.
Washing	300 nl	8 min 22 s	Yes	Washing cellular debris from DNA.
Elution	15 nl	25 s	Yes	Elute DNA into the PCR chamber.

Table 3.9: Summary of an example diagnostic process for a buccal swab sample preparation using theoretical beads of the same magnetic properties as the MyOne Dynabead ($\chi_v = 1.5$). Off-chip pre-processing amounts to 22 min and the on-chip SP sums to 4 min 20 s.

SP Step	Volume	Processing Time	Integration	Notes
Collection	N/A	N/A	No	Dependent on assay of interest.
Lysis	1 ml	20 min	No	Incubation at 37 °C.
Purification	140 µl	2 min	No	Binding the DNA, collecting the beads.
Transfer to Chip	150 nl	1 min 24 s	Yes	Drawing sample into the SP module.
Washing	300 nl	2 min 48 s	Yes	Washing debris from DNA.
Elution	15 nl	8.4 s	Yes	Elute DNA into the PCR chamber.

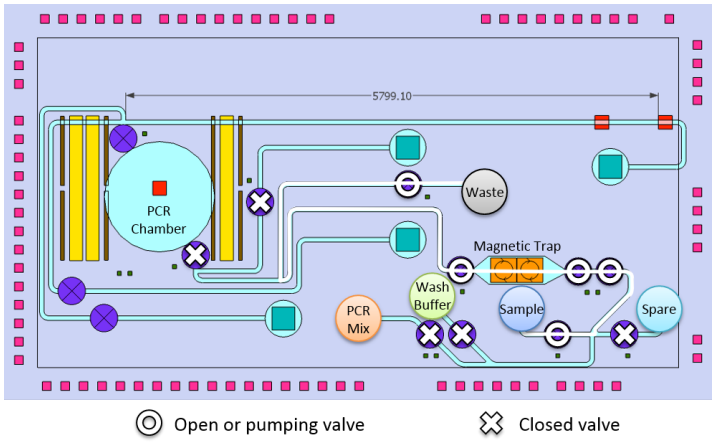

(a) Bead Trapping

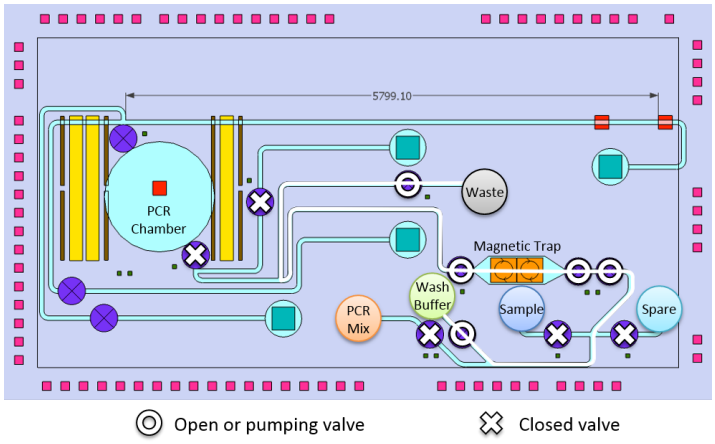

(b) Washing

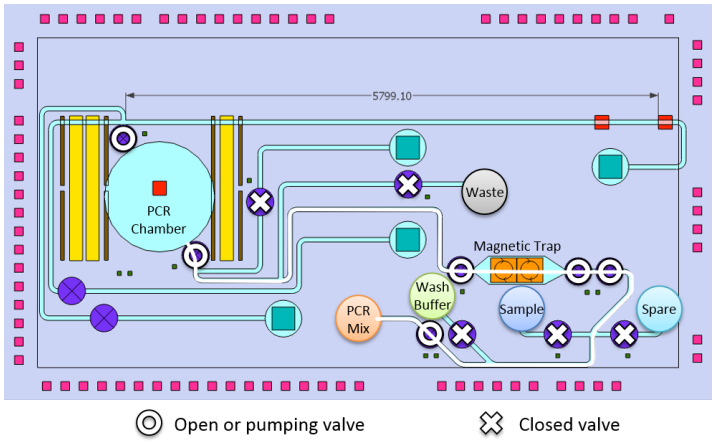

(c) Elution

Figure 3.24: Example on-chip SP process - purification of genomic DNA from a buccal swab. (a) Trapping of DNA-magnetic bead conjugates in the SP chamber by the CMOS spiral electromagnets, (b) washing of cellular debris away from the isolated DNA, (c) elution of DNA into the PCR chamber from the trapped beads.

3.10.6 Processing Gaps Identified in the Example Diagnostic Process

One of the most important aspects of exploring an example choreography is to clearly flag the parts of the process that are not yet integrated. Those not-yet-integrated parts make up the chip-to-world interface and (from the protocol explored above) include cell lysis and DNA purification. The processing parts that are currently integrated include sample washing and DNA elution to the PCR chamber.

Indeed, macro-scale integration of the pre-processing steps could be done in a hand-held device. It is important to note, however, that the current integration is a first step towards a full-integrated and cost effective solution, and that the next step in this research could be to make use of additional reagent reservoirs to implement the lysis and purification steps. Refer to figure 3.24, and note the "spare" reservoir in the bottom right corner. With those two steps integrated, the system as-designed would be capable of on-chip processing of samples roughly 1 µL in volume.

One potential issue in the macro-scale regime that has not been integrated with the microfluidic-CMOS system is the possibility of reduced effectiveness of biological protocols implemented in the reduced-volume system. There are ways to mitigate reduction in protocol efficacy, but these techniques must be explored/determined for each protocol of interest.

To summarize, this example choreography has demonstrated which pieces of the system are integrated in the microfluidic-CMOS system, which are not, and which parts of the process require further work, namely the packaging and chip-to-world interface by designing macro-scale components to accomplish initial steps of the SP process.

3.11 Conclusions: Sample Preparation in Integrated Microfluidics-CMOS LOC Technology

One of the next steps to carry this work forward is to engineer packaging to interface the microfluidic-CMOS device with the macro-scale world. The pieces for doing the microscale level SP have been shown; handling of raw samples requires further research. The pre-processing steps described in section 3.10 are highly dependent on the sample of interest: a dried blood spot, liquid urine, buccal swabs and lake water are four clearly different starting points for sample preparation.

Although there is much work to do in this area, the pieces are in place to facilitate the next integration steps.

It was confirmed by experiment that the magnetic simulations had good predictive ability for the performance of the rapid-prototyped PCB magnetic preparation module, suggesting that the simulations of the CMOS SP module also have predictive value. Specific SP processes at reduced reagent volumes have not yet been tested, but appear to be feasible based on prior work.

The advantages of using an integrated sample preparation system over traditional methods are clear: lower reagent volumes reduce the price per test; when applicable, smaller sample volumes can reduce invasiveness to the patient (e.g., blood testing); integration of SP steps reduces the chance of contamination; automated processing allows the testing to be performed by unskilled operators; hand-held infrastructure removes the need for expensive laboratories and personnel, enabling remote point-of-care testing. Magnetic beads (as opposed to alternatives presented in section 3.4.3) drive this integrated approach since they enable the ability to cascade SP stages to reduce sample volume to the point where it can be handled by micro-scale on-chip infrastructure.

Indeed, unpublished past work from the BioMEMS project on glass-based LOC devices made it clear that it is difficult to do selective manipulation of beads at the macro-scale using mechanical actuation and permanent magnets. Automating the bead-handling process with electromagnets that provide high spatial selectivity of bead trapping avoids all of the previously experienced problems while leaving the simpler manual manipulation of the raw sample off-chip until it can be integrated with the chip-to-world infrastructure should be part of the next steps in this research work.

Even without the chip-to-world scaling components, this work presents a new level of integration and makes up part of a LOC platform that is truly scalable in terms of manufacturability. With high-volume manufacturing, the cost per test is effectively driven down, making affordable POC testing one step closer to reality.

For all the conservative estimates and unknowns discussed in this chapter, the integrated SP module in the system chip ICKAAL12 has been designed to be capable of achieving a useful processing period (on the order of minutes for an on-chip volume in the microlitre range) for the first time in the ICKAALXX series of chips. The key pieces to make on-chip SP work have been shown in this chapter, which is a significant contribution to the goal of a fully-integrated on-chip rapid diagnostic. A high-force electromagnet allows for selective trapping and releasing of beads, and the recommendation of valve slew rate control mitigates the possibility for transient pressures to cause

untimely bead release. The final-step sample concentration and direct-to-PCR elution maximizes sample for amplification while removing an opportunity for contamination.

Exploring the past and present of the state of the art in sample preparation methods for lab-on-chip devices has enabled this achievement and has set the stage for more effective iterations of the SP component of the diagnostic process going forward.

Given that the processing time for the SP step is on the order of minutes, it is desirable to achieve a similar time scale for the PCR step. The next chapter explores one way to use FEM combined with a useful design methodology to produce thin-film heaters for PCR amplification of the sample.

CHAPTER 4

THERMAL SYSTEMS FOR INTEGRATED MICROFLUIDICS-CMOS LOC TECHNOLOGY

Microfluidic LOC systems often require some form of thermal control over a fluidic volume. Spatial control of thermal modules is a major challenge. Spatial selectivity is important for saving space and power, and temperature uniformity in heated volumes is essential for some important LOC functions such as PCR and MCA. Thin-film metal heaters are frequently used for LOC thermal requirements, but it is difficult to achieve uniformity in such systems.

By using a novel methodology to design thin film heaters capable of rapid, uniform heating of a PCR volume, we propose a system that is designed to perform a standard 3-step, 35-cycle PCR in under two and a half minutes (4.19 s per thermal cycle). The heater design method is implemented in an in-house polymer-on-silicon chip architecture that includes the embedded aluminum thin-film heaters. Fast, selective, uniform heating is demonstrated by infrared imaging of the powered heaters. Four different heater designs are generated and all showed uniformity within $\pm 0.5\,^{\circ}$C at the target temperature of 95 °C in the majority of the chamber volume (94% to 100% depending on the design). A final demonstration of the heater design method is implemented in a first-pass design of a thin-film heater for the system chip.

Dr. Jose Martinez-Quijada contributed significantly to this chapter by developing the first 1D RLC thermal models and 2D FEA models in COMSOL from which the rest of the thermal systems research work followed. Moreover, Dr. Martinez-Quijada created (as part of his PhD work) the first version of the non-iterative technique to automatically layout thin film heaters, as described in section 4.3. My role in the work was to take the modeling a step further and implement our designs, both preliminary and final, as 3D FEA models. This work is also published in [68].

4.1 LOC Thermal Systems

4.1.1 Background

As discussed in section 2, sample amplification (PCR) is an essential component in many diagnostics. An inexpensive heater for producing fast, uniform heating of a LOC PCR chamber is essential in achieving far-reaching use of POC devices. Indeed, temperature uniformity has a significant impact on PCR efficiency [69, 70], and accuracy in quantitative PCR (qPCR) and melting curve analysis (MCA) [71, 72]. In addition to fast, uniform heating, a PCR system should be unperturbed by changes in the ambient environment.

Several methods for producing uniform temperature PCR volumes in LOC devices have been explored: temperature-controlled blocks to heat entire devices [73] [73], infrared lamps [74], and Peltier cells [72] to name a few. However, these methods can be both power-inefficient and slow [75]. Infrared lasers have been proposed as a selective heating method [76, 77], but bulky, costly, precise optical instrumentation is required, and does not mesh well with the LOC mantra of full integration.

Following the motivation outlined in section 1.5, mass production drives the cost-per-device down such that integrated thin-film heaters can be affordable. Integrated thin-film heaters can be fabricated in close proximity to polymer microfluidic structures such as PCR chambers. Such thin metal elements have very small thermal mass, and can be used to achieve efficient power usage and fast heating/cooling. Difficulties in controlling temperature gradients across a thin-film heater and associated PCR chamber are exacerbated by the use of low-conductivity polymer materials for structural components [70, 78]. For example, planar heaters experience high heat loss at the edges, resulting in poor temperature uniformity. Another requirement of thin film heater materials is a resistance to electromigration and stability at high temperatures, since PCR requires temperatures of around 95 °C to denature DNA. These material characteristics are exhibited by platinum, making it the most commonly used metal for LOC thin film heaters [79]. Platinum has many drawbacks, however; Pt is expensive, requires Ti or Cr adhesion layers, and patterning requires lift-off [79] or a highly toxic wet etch in aqua regia at 90 °C. An inexpensive, CMOS-compatible metal like aluminum is desirable over platinum, but has less resistance to electromigration. If Al is to be used in a LOC PCR heater, current density should be taken as a key parameter during the design phase to achieve an acceptable device lifetime. Our group has demonstrated Al as a suitable alternative to Pt for thin-film heaters on polymer [80].

While heaters designed in serpentine, parallel, or block heater configurations have shown moderate levels of temperature uniformity, array-type heaters have demonstrated superiority [81–83]. An array-type parallel-track heater presented in [82] achieved $\pm 1\,^{\circ}\mathrm{C}$ variation at $94\,^{\circ}\mathrm{C}$ in 90.3% of a 5 mm diameter chamber by increasing power dissipation at the heater edges to compensate for cooling. In [83], Wang et al. demonstrated $\pm 2\,^{\circ}\mathrm{C}$ uniformity at $94\,^{\circ}\mathrm{C}$ for 98.5% of a 5.2×5.2 mm area on a 6×6 mm Pt/Au array microheater. Both of these designs require two layers of noble metals, making them expensive and not CMOS-compatible.

As mentioned above, PCR speed is very important in achieving the sample-to-answer times required by many POC applications. One of the most rapid PCR demonstrations to date was accomplished by Wheeler *et al.* in [1]. Polymerases exist that perform amplification of DNA at much faster rates than the wild-type *Taq* polymerase. For example, *Pyrococcus kodakaraensis* (KOD) polymerase was shown to support an amplification step of 15 s in a thermal cycler for 40 cycles in ten minutes [84]. One strategy for reducing PCR time is to employ a two-step reaction (denature, anneal) instead of the standard 3-step (denature, anneal, extend), in which the extension happens during the temperature ramps. Wittwer *et al.* showed that denaturing and annealing can be done very quickly, even without dedicated hold-times at their target temperatures [85]. Moreover, it was shown in [86] that specificity of the reaction decreased with a longer anneal hold time and longer ramp to that temperature. It was put forward in [87] that minimum extension and denaturing times of 6.5 s and 2 s were required for high efficiency in amplification, but [88] suggested that only 3 s and 1 s are required for those two steps, respectively. Wheeler states in [1] that the group is working towards real-time PCR detection methods, so speed (shorter time to answer) is desired at the expense of strong amplification. The thermal system used in [1] was made up of a water-heated/cooled copper block in which a polypropylene PCR-well insert was placed. A metal thin film heater in Kapton heated from above. Each PCR well holds 5 µL of PCR mix, and is covered by a PCR adhesive seal. The system in [1] achieved heating and cooling rates of $45\,^{\circ}\mathrm{C\,s^{-1}}$, which yielded thermal time constants of 1.02 s and 1.32 s respectively, allowing sub-three minute reactions. A direct comparison of the rapid PCR capabilities of the system in [1] will be made to our system.

4.1.2 Designing Heaters

The design methodology used to produce thin-film heaters suitable for LOC applications is generally rigid, time-consuming and costly. An iterative process is often employed; a heater geometry is

suggested, tested or simulated, and then corrected to improve uniformity. This whole process is repeated until suitable temperature uniformity in the region of interest is achieved. While this process may be acceptable for doing a one-off design, there are major issues if design parameters must be updated. If changes to the structural geometry, materials or boundary conditions occur, then the heater as-designed will no longer be optimized and uniformity will suffer, perhaps greatly. In both academia and industry, frequent changes of device structure and materials during the design process are common. Engineering design consulting companies must tailor their work to the whims of clients, who often have very specific applications and conditions. It is therefore very useful to have a well-organized and flexible approach to generating optimized heater designs.

Selva et al. demonstrate a very advanced heater design method in [89]. A single-layer platinum heater is optimized with respect to a PCR chamber of specific dimensions to minimize size, save power and compensate for edge cooling. An initial width for heater tracks connected in parallel is inputted, and an algorithm produces generations of variations on the input. All the variations are tested through FEM, and the cycle is repeated until a threshold for generation number is reached (1000 in [89]). Uniformity is reported as $\pm 0.6\,^{\circ}\mathrm{C}$ at $37.5\,^{\circ}\mathrm{C}$ in 82% of the area of interest, but is not explicitly reported at PCR temperatures, at which gradients are more difficult to compensate for. Furthermore, this method is iterative, exceedingly complex, and computationally demanding.

As mentioned in the introduction to this chapter, Dr. Jose Martinez-Quijada, with contributions from the author, Matt Reynolds, David Sloan, Dr. Dan Sameoto, and Dr. Duncan Elliott, produced a non-iterative technique to automatically layout thin film heaters [68].

The metal thin-film heaters that are generated by Dr. Martinez-Quijada methodology can produce a highly uniform temperature in a close-proximity volume of interest, of arbitrary shape and size. Compensating for uneven heat loss and edge effects, the heaters maximize the area of uniform temperature. Moreover, for a wide range of voltages, power requirements are minimized and current densities are maintained at low values. As mentioned in section 4.1.1, control over current density is vital for enabling the use of affordable Al metallization, which is easy to pattern and compatible with CMOS processes.

4.2 Integrated KMPR-Aluminum Thermal System

The design method mentioned briefly in section 4.1.2 and discussed in more detail in section 4.3 was used to design several heaters for PCR LOC systems. As stated earlier, our goal is to integrate

PCR function in CMOS chips. As a prototype for a future KMPR-CMOS system, we fabricated in-house LOCs constructed in layered KMPR-on-silicon with integrated aluminum heaters and a polypropylene sealing layer on top. The substrate is in contact with a heat sink at the bottom. Figure 4.1 shows a generalized cross section of the PCR chamber, heater, and substrate. Layer thicknesses and other parameters pertaining to the simulations are discussed further in subsequent sections.

In all designs we completed, we aimed to solve the problems outlined in section 4.1.1 while designing within the constraints of our processes. The key points are summarized as:

- High uniformity in PCR chamber temperature
- High speed in temperature ramping
- Robust system to changes in ambient conditions
- Design within voltage requirements
- Maintain low current density for Al heater

The configuration shown in figure 4.1 will require higher power delivered by the heater at the edges to achieve the high temperature uniformity we desire. More specifically, we wish to achieve 1 °C uniformity in the chamber volume at 95 °C (the highest PCR temperature). Another key point of this configuration is the proximity of the heater to the chamber. This allows the chamber and heater to be very close in temperature and reduces transients, which allow for fast thermal cycling. Furthermore, low thermal conductivity of polymers paired with the high conductivity of the silicon substrate yield another benefit: the thermal resistance from the heater to the environment is orders of magnitude higher than the resistance from the heater to the chamber, which makes the system very insensitive to changes in ambient conditions. Thus, the architecture chosen for our designs should be able achieve the points summarized above.

The first application of our design method was exercised on heaters designed with two different power density profiles. Uniform power density ("U") heaters deliver uniform power over a given area, and maintain low current density levels. However, by definition, uniform power delivered to an area which requires compensation for extra heat loss at the edges means that the heaters must be larger, and therefore use more power. Non-uniform power density ("NU") heaters compensate for edge effects by increasing the power density near the perimeter of the area of interest. In this case, the aluminum metal is driven at higher current densities, which will risk shorter device lifetimes

due to electromigration. A broad range of potential applications exist for these two power density profiles. Additionally, two different chamber sizes were explored (500 and 1200 µm in radius) for a total of four configurations, titled: “U850”, U1550”, “NU750”, “NU1450”.

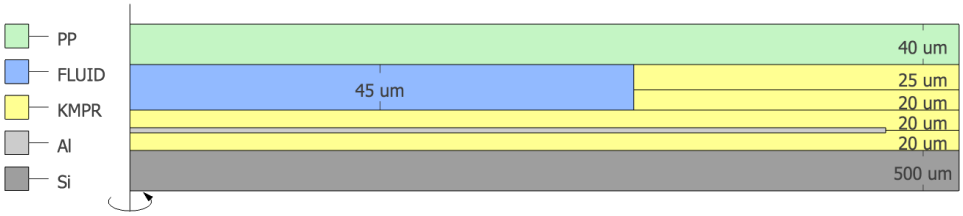

Figure 4.1: Cross section of the prototype target PCR system. Shown here is an axisymmetric model. KMPR layer thickness is 20, 20, 20 and 25 µm from the bottom to the top respectively. The sealing polypropylene layer is 40 µm, the silicon substrate is 500 µm, and the aluminum thin film heater was fabricated at a thickness of 180 nm. Note that the silicon and aluminum layers are not to scale.

4.3 Heater Design Methodology

The design methodology is briefly outlined here to make clear why each simulation is required.

Without control over the spatial distribution of power density delivered by a planar heater, regions with less thermal isolation will experience a more significant drop in temperature, contributing to non-uniformity of temperature in the region of interest. By finding the exact profile of power density that is required to produce a uniform temperature in a PCR chamber volume, a heater can be designed which delivers that profile and yields close to the desired temperature distribution, which in this case is uniform.

The procedure for designing a heater topology can be described in three steps:

1. Calculation of the Q profile

2. Discretization of the Q profile and track layout

3. Verification

The first step requires a basic FEM of the system to determine the power density field Q that produces the desired uniform temperature in the PCR chamber. This Q field is specific to the boundary conditions of the particular system. The second step sees the Q field found in the first step divided into small rectangular segments, from which the heater track width is calculated. The heater layout is then generated from the width data. All of this is accomplished by MATLAB code written by Jose Martinez-Quijada. The third step of the procedure requires a 3D FEM of the system with the heater layout included. A voltage parameter is applied to verify that the desired temperature, uniformity, and current density are achieved.

Examples of each of these steps are found in sections 4.4.1, 4.4.2, and 4.4.3 below, which serve to illustrate the process.

4.3.1 Step 1 - Power Density Profile Extraction

Again, our goal is to create a PCR volume with uniform temperature. The architecture of the polymer structure, i.e., PCR chamber dimensions, is known. This step can further be broken down into two parts. In the first part, the optimized heater radius is found, given the selected chamber dimensions. In the second part, the power density profile is extracted.

4.3.1.1 Part A: Heater Radius Optimization

In COMSOL Multiphysics, a model is constructed that accurately describes the system geometry, materials, and boundary conditions. Heat-transfer physics is included in the analysis. Since our system is nearly axially symmetric, a 2D model is used to reduce the simulation computation time. If a system is not axially symmetric, then a full 3D model would be required. In the 2D model of our LOC, the heater is represented by a line positioned at a depth beneath the PCR chamber matching the dimension of KMPR1 thickness. The heater is prescribed a uniform temperature boundary condition, at our highest target chamber temperature, 95 °C. With the heater radius, r_h, parameterized, a simulation is run to find the minimum radius that suffices to achieve temperature uniformity of 0.5 °C within the PCR chamber volume (or area, in our 2D model). Heater radius r_h is increased from the chamber radius r_c until the optimal value is found. This model is very simple, and

requires only a few seconds to complete. This relation between r_h and r_c holds true for any change in planar geometry or power density distribution. To summarize the flexibility of this process, the following concepts are shown:

- 2D geometry of the thermal space is free to choose.
- The temperature distribution and resolution in the thermal space are free to choose.
- The heater-chamber margin is calculated once per fabrication scheme, and is applicable to any adjustments to the temperature field and geometry.

With this relation in hand, the second part of this step can be performed.

4.3.1.2 Part B: Qup/Qdown Extraction

A 3D model of the device is constructed in COMSOL Multiphysics, including the heater (2D circle) of appropriate radius with respect to the chamber. As in Part A, the uniform temperature boundary condition is prescribed to the 2D circular heater. This ideal heater is forced to maintain a uniform temperature profile, T, over its area, and produces a uniform temperature within 0.5 °C in the chamber, as per Part A. After running the simulation, the heat flux, Q, sourced from the 2D circular heater to achieve the desired uniform T profile, is extracted. The extracted Q field is the power density function that must be reproduced by the heater layout to achieve a uniform temperature distribution in the PCR chamber. Locations that experience more heat loss will require higher power density to comply with the uniform temperature boundary condition constrained on the heater plane. This is the real key that makes this method deterministic; the designer chooses geometry and temperature distribution, and the Q field to achieve it is solved-for directly.

The upward and downward Q fields (from the heater plane) are extracted by sampling the solved model at a resolution of choice. As an example, values can be obtained in a 1 um grid in xy planes above and below the heater, and exported from COMSOL in matrix form. This data is then imported to MATLAB for discretization in the next step.

4.3.2 Step 2 - Power Density Profile Discretization and Track Layout

The two Q fields (Qup, $Qdown$) extracted in step 1 represent all of the heat flux produced by the heater, and are summed up point-wise to find the total power density generated by the heater. This total Q field is discretized into a grid form with rectangular segments of length L and width s. Figure

4.2 displays this visually. Segments outside the perimeter of the heater circle will see only Q matrix values of zero, since no heat flux is produced here. Segments will be connected along the y-direction to make heater tracks. Each of these segments contains a piece of the track of width w padded by spacing. Track width w plus the spacing makes up the segment parameter s, which in turn is the pitch between heater tracks that will be created by this design process. Resultant tracks will be connected to a common potential. However, to fit the designer's current and voltage requirements as well as control the track width and current density, some tracks may be connected in series as groups.

Since each segment is a sub-matrix of the Q field, those that are outside the heater and, therefore, show only values of zero, will be assigned track width $w = 0\,\mu\text{m}$. All other segments, which contain non-zero elements, will have a w calculated for them. The resulting matrix (W) of track widths (w) contains all the information required to automatically lay out the heater. Since polygons are drawn only for non-zero elements of W, the heater shape can be arbitrary. Only locations in x-y that produce heat flux will have heater segments defined for them.

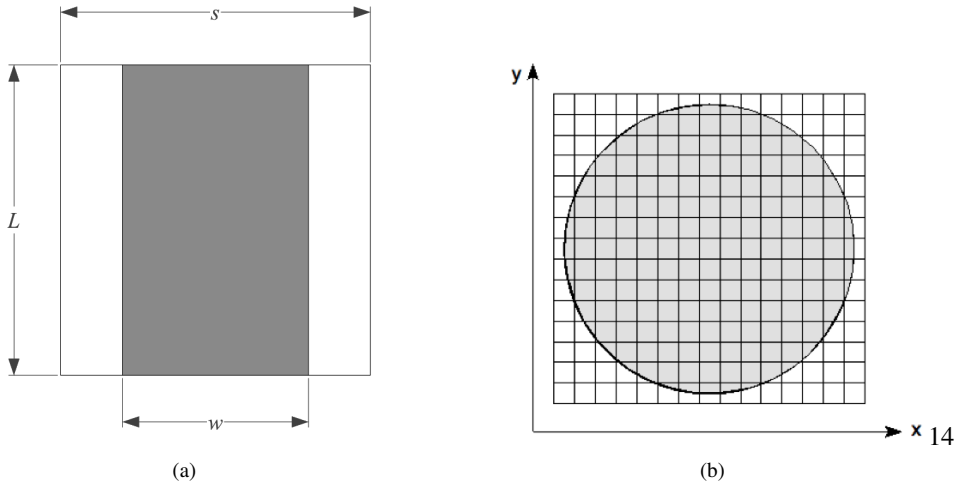

Figure 4.2: Q field segment discretization. (a) Segment structure. A segment is made up of a track segment (width w) and spacing on either side. L and s are controlled independently. (b) Discretization of the Q field into segments of width s and length L. The heater area (gray circle) will have non-zero elements in the matrix.

By integrating the power density over a segment area, the power delivered by each segment is

calculated. The metal film resistivity is approximated linearly, as in equation 4.1.

$$\rho = \rho_0(1 + \alpha(T - T_0)) \tag{4.1}$$

Where ρ_0 is the resistivity of the heater material at a reference temperature ($12.7 \pm 0.2 \times 10^{-8}\,\Omega\,\mathrm{m}$ for Al); α is the temperature coefficient of resistivity – TCR ($2.07 \pm 0.02 \times 10^{-3}\,\mathrm{K}^{-1}$) and T_0 is the reference temperature (22 °C). The values mentioned were measured for Al films on KMPR [80]. The resistivity vs. temperature curve of the film is highly linear, as verified in [80], making equation 4.1 a valid approximation.

After using the power and resistivity information to calculate the current in and resistance of each segment, the track width w to meet those values is calculated directly. It is important to note that the piece of track within its larger segment (which includes spacing) must account for all the power delivered by that segment. Equation 4.2 describes the relation between the power densities of the segment and of the track piece. The metal track's power density (Qt) must be greater than that of the segment (Qs), by the factor s/w. Consequently, the metal temperature will be higher than the target (95 °C), and the gaps between tracks will be lower than the target, but together, the average temperature across the segment will be 95 °C.

$$Q_t = Q_s \frac{s}{w} \tag{4.2}$$

When it is desirable to connect some tracks in series as groups to lower the current requirements and reduce current density, the track width w is calculated normally, but the current is calculated from the total power delivered by the group, as opposed to just one track. The number of tracks within a group can be selected by the designer to meet various requirements (e.g., reduce current to keep below a current density design rule), with the restriction that the number should be odd such that the voltage can be applied across the grouped tracks.

4.3.3 Step 3 - Verification

Once the Q field has been calculated (step 1) and the heater layout automatically generated (step 2), the final step is to check that the system behaves as expected. Since this method is deterministic, there should be no extra iteration required.

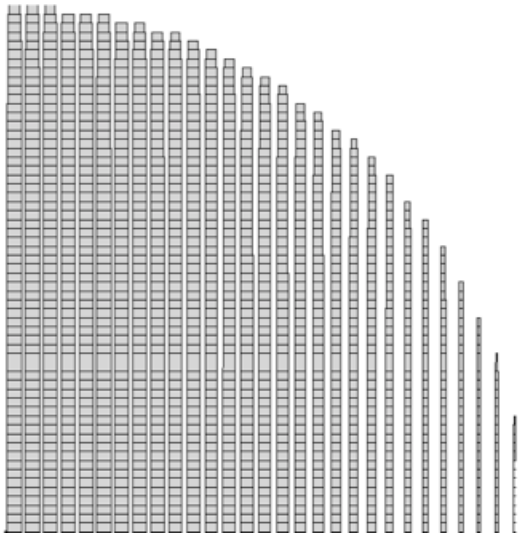

Figure 4.3: Polygons generated by the MATLAB® script. Shown is ¼ of an example grid heater. In this example, tracks are all connected in parallel. Notice the changes in track width w in both axes to properly generate the required Q for achieving the target chamber temperature and uniformity.

The Joule-Heating physics interface is added to the Heat-Transfer physics in the COMSOL model to demonstrate a fully-coupled system.

4.3.3.1 Part A: Virtual Connections

The 3D model from step 2 is updated with the actual heater layout; at this stage of development, the MATLAB®script does not include the connections between tracks within a group, though these connections are very simple to add by hand in any CAD program of choice. The unconnected set of tracks is set up in COMSOL with virtual connections – a boundary condition that serves zero electrical resistance and carries current from one track to the next. This step should show excellent agreement with the chosen design parameters. In our case, that means a 95 °C target temperature in the chamber and uniformity within 1 °C.

4.3.3.2 Part B: Physical Connections

Once the virtually connected layout expectations are confirmed, physical connections to the power bus and between tracks are added. This layout is what would be fabricated, and will be transferred to a mask for printing. Connections between tracks should be as wide as possible to minimize their resistance. Adding any significant resistance in series between tracks would disturb the design, since

accumulation of these connections could lead to a substantial voltage drop which is expected to be across the heater tracks.

Upon successful verification of the physically connected device, the design can be submitted for fabrication.

4.4 Simulation Results and Discussion

To demonstrate the design process in a detailed but concise manner, the results of just the NU1450 configuration will be followed here.

It should be noted that the four heaters were originally designed with different metal resistivity, TCR and thickness expectations than what was fabricated. From earlier work [80] it was expected that the resistivity and TCR of the aluminum thin-film would be $4.39 \times 10^{-8}\,\Omega\,\mathrm{m}$ $3.518 \times 10^{-3}\,\mathrm{K}^{-1}$). The intended thickness was 100 nm, but the resulting films were 180 nm. It was found that the increase in resistivity was offset by the increase in film thickness, and the results of the heater designs were unchanged.

4.4.1 Step 1 - Power Density Profile Extraction

4.4.1.1 Part A: Heater Radius Optimization

A 2D axisymmetric steady-state model is constructed to optimize the heater radius with respect to the chamber radius. An image of the geometry is shown in figure 4.4. The parameters used in this model are as follows:

Heater radius r_h is parameterized with an initial value equal to r_c, and is increased until desired uniformity in the chamber is attained.

Thermal modeling in COMSOL requires at least three material properties: heat capacity (Cp), density (ρ), and thermal conductivity (k). Each domain in the model is assigned the appropriate material: KMPR (structural elements), water (PCR chamber), or silicon (substrate). It is not necessary to assign a material to the "heater", which is simply represented by an unbroken 1D line in the axisymmetric model.

Table 4.1: Simulation parameters. These values hold for all subsequent simulations unless otherwise stated. Note that the chamber and heater radius are dependent on the heater configuration being designed.

Parameter	Value	Description
T_{amb}	22 °C	Ambient temperature (air above the system)
T_{hs}	30 °C	Heat sink temperature
T_h	95 °C	Ideal heater temperature
htc_{air}	$5.6\,\mathrm{W\,m^{-2}\,K^{-1}}$	Heat transfer for natural convection in air
r_{chip}	2.5 mm	Radius of the silicon chip
r_c	500 µm or 1200 µm	PCR chamber radius
r_h	$r_{chamber} + 250\,\mu m$ or $+350\,\mu m$	PCR heater radius (750 µm)
h_{Si}	500 µm	Thickness of silicon substrate
h_{layer1}	20 µm	Thickness of KMPR layer 1
h_{layer2}	20 µm	Thickness of KMPR layer 2
h_{layer3}	20 µm	Thickness of KMPR layer 3
h_{layer4}	25 µm	Thickness of KMPR layer 4
$h_{membrane}$	40 µm	Thickness of polypropylene membrane

Physics "nodes" must be added to the model, and in this case, we are interested in the "Heat Transfer" physics interface. Once the "Heat Transfer in Solids" node is added to the model, boundary conditions can be assigned. The initial values for all geometry domains is set to the heat sink temperature, and a "Temperature" boundary condition (T_{hs}) is set to the bottom boundary of the silicon substrate to model the device sitting on a heat sink. All other boundaries will be exposed to air, so a "Heat Flux" condition is added to those boundaries with a heat transfer coefficient of $5.6\,\mathrm{W\,m^{-2}\,K^{-1}}$ [90] and an external temperature of T_{amb}. The heater is assigned a uniform temperature of T_h, and with that, the model is complete. A mesh is constructed for the geometry, and for such a simple model, the meshing is done in a matter of seconds.

After computation, post-processing figures and graphs can be plotted. To determine what value for r_h satisfies our criteria of ± 0.5 °C uniformity in the chamber (as described in section 4.3), we plot a 1D graph of temperature with respect to radius. By plotting the temperature of the chamber top and bottom in addition to the heater, we can easily see what r_h level achieved our condition. Figure 4.5 shows just three values for clarity: 500, 600 and 750 µm. The target uniformity of ± 0.5 °C across the chamber radius is achieved with a heater of radius $r_h = 750\,\mu m$. This $r_h - r_c$ relation of 250 µm holds true for any shape or power density distribution desired, provided the fabrication scheme remains the

same (i.e., layer thicknesses). Since this margin is found by use of a uniform temperature condition (non-uniform power density), it is applicable to the two heater designs which adhere to this scheme (NU750, NU1450).

The power density required to produce a uniform temperature in the PCR chamber (for all but the very tip of the radial length) is used as an input for determining the margin required for the uniform power density heaters. The value found in the simulation above was $0.6314 \times 10^6\,\mathrm{W\,m^{-2}}$; the temperature boundary condition (T_{hs}) was replaced by a uniform power density condition with $Q = 0.6314 \times 10^6\,\mathrm{W\,m^{-2}}$, and it was found that a margin of 350 µm was required to maintain the $\pm 0.5\,^{\circ}\mathrm{C}$ PCR chamber uniformity. This yielded the U850 and U1550 heater models for the chamber sizes $r_{ch} = 500$ and 1200 µm respectively.

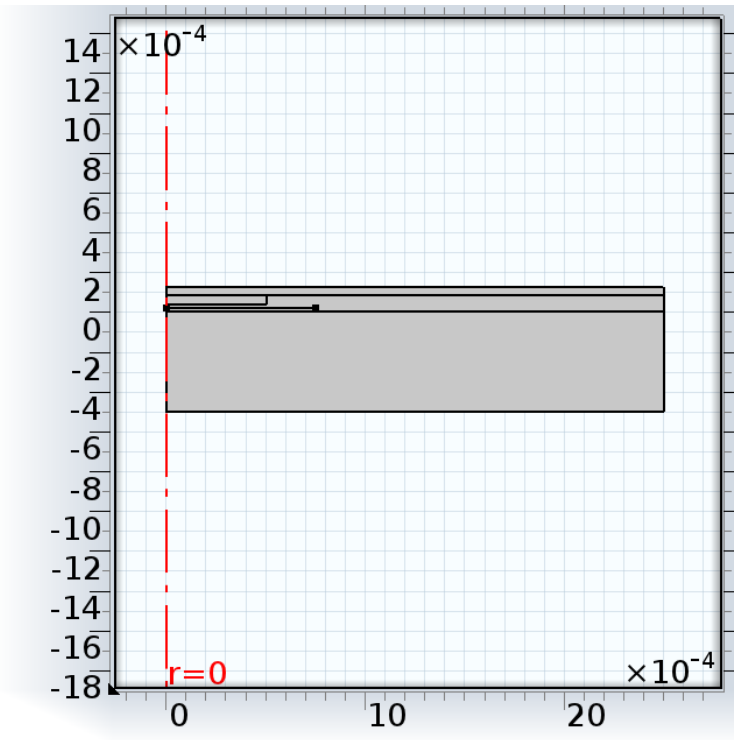

Figure 4.4: Step 1 Part A: NU750 thermal system model geometry. Axisymmetric model for $r_h - r_c$ relation simulation.

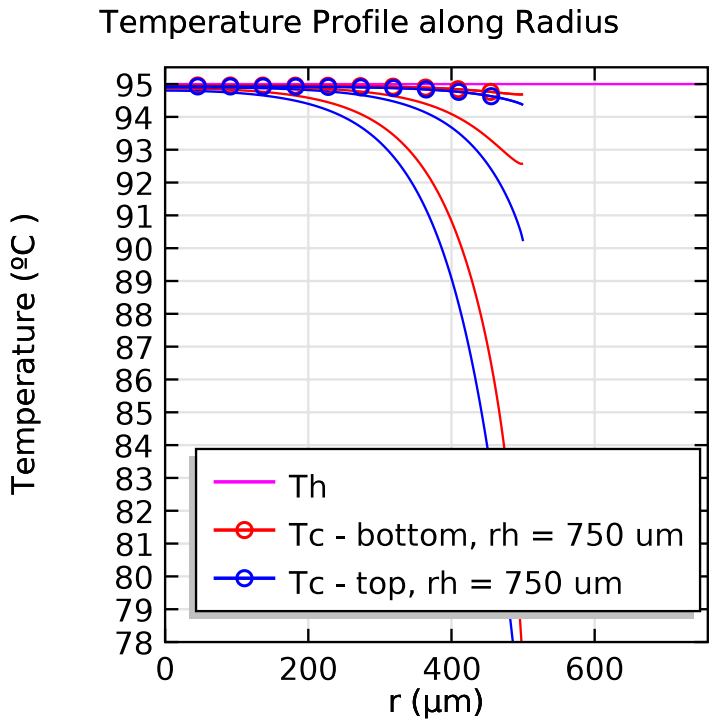

Figure 4.5: Step 1 Part A: NU750 heater-chamber temperature results. T_h, T_c bottom and top for three r_h radii for a set r_c.

4.4.1.2 Part B: Qup/Qdown Extraction

A 3D model using the same parameters in part A is constructed. The heater remains a uniform disc of radius r_h, which will supply the necessary power density gradient along its radius to achieve the uniform temperature boundary condition imposed. This power density profile is extracted and used as input to the algorithm that automatically lays out a heater design. An image of the geometry is shown in 4.6(a).

Similarly, the uniform power density models are prescribed ideal heaters supplying the calculated uniform power density from part A. The power density profile is then extracted the same way for the non-uniform models, and is processed identically to produce tracks that maintain low current density requirements at the expense of a higher power requirement.

As before, the model is assigned appropriate materials and physics nodes to achieve the heat transfer quantities of interest. Boundary conditions remain the same as those discussed in part A, but are now assigned to more surfaces, since the model has been configured in 3D. The uniform temperature condition on the heater again serves to provide all the power density required to achieve

the uniform chamber temperature that we are targeting.

Once the solution is computed, appropriate data sets can be created to extract the Q information. In the 'Results' node, a parameterized surface can be added to the solutions list. Two square surfaces were constructed to capture all of the heat flux generated by the heater. Separated by a small distance (0.5 µm) above and below the heater, the squares had a side length of $r_h(2)(2900\,\mu m)$. Using square-shaped data sets facilitated straightforward handling in MATLAB. Values outside the perimeter of the circular heater area read zero, since no flux is generated there. The above-heater surface is displayed in figure 4.6(b), and a Q profile height extrusion is shown in 4.6(c). This plot makes it very clear that the power density requirement sharply increases at the edges of the heated area. As mentioned in section 4.3, the resolution of the extracted data can be selected. For example, data can be sampled at 1 µm intervals in x and y on the two square parameterized surfaces above and below the heater. The data is discretized into new segments and used to construct tracks in MATLAB in the following step.

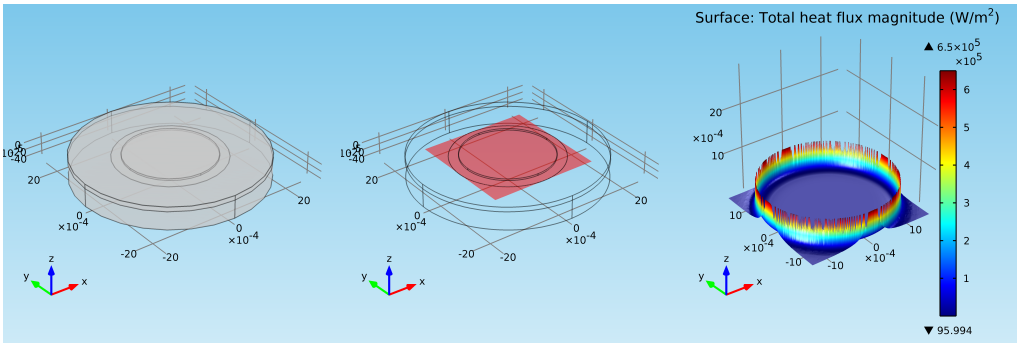

(a) (b) (c)

Figure 4.6: (a) 3D geometry (b) Plane above and below heater for Q extraction (c) Extrusion of summed Q values. This plot displays the sharp increase in power density required at the perimeter of the heated region, to achieve a uniform temperature in the chamber volume.

4.4.2 Step 2 - Power Density Profile Discretization and Track Layout

Since this step is a significant focus of Dr. Jose Martinez-Quijada's work and a summary of the process was described in section 4.3.2, only the final results are mentioned here.

Some constraints were placed to ensure success of the four devices. Operating voltage was

limited to about 4 and 10 V for the small and large heaters respectively. Also, to ensure reliable lift-off during fabrication, a minimum spacing of 5 µm was maintained between tracks. For our designs, a final constraint was that an odd number of tracks was required to facilitate connection to the power buses located on opposite sides of the heater.

Tracks were grouped, as per the discussion in section 4.3.2, to reduce current density in the tracks. Final grouping allocations and detailed specifications for the four heaters are listed in 4.2. The 2D geometry is generated as a Drawing Interchange Format (DXF), a computer-aided design (CAD) data file format that is supported by many CAD programs, including COMSOL.

Table 4.2: Four heater configurations and their specifications.

Parameter	NU750	U850	NU1450	U1550	Unit
P	1.130	1.402	4.194	4.578	W
V	3.4	3.4	9.0	10.0	V
R	10.23	8.24	19.31	21.84	Ω
I	0.332	0.412	0.466	0.458	A
J_{max}	26.67	16.36	19.83	13.66	$\mathrm{mA\,\mu m^{-2}}$
J_{min}	11.89	10.94	11.13	11.62	$\mathrm{mA\,\mu m^{-2}}$
w_{max}	24.54	27.60	45.73	52.56	µm
w_{min}	10.23	14.53	28.99	37.83	µm
g_{min}	5.46	6.40	4.27	9.44	µm
Pitch	30	34	50	62	µm
No. tracks	50	50	58	48	-
Groups of tracks	6 of 3, 1 of 7	6 of 3, 1 of 7	4 of 5, 1 of 9	3 of 5, 1 of 9	-

4.4.3 Step 3 - Verification

A full 3D model including coupled Joule-heating and heat-transfer physics was used to verify that the heater designs performed as expected.

4.4.3.1 Part A: Virtual Connections

The MATLAB®-generated 2D heater layout is imported as a .dxf file into the COMSOL geometry environment, and is mirrored in the x and y axes to produce a full layout, displayed in figures 4.7(a)

and 4.7(b). This set of heater tracks replaces the ideal heater in the 3D model that was used to extract the Q field necessary for $\pm 0.5\,^{\circ}\mathrm{C}$ uniformity. To test the as-designed tracks for producing that uniformity, virtual electrical connections between series-grouped tracks are added to the model. Since this model is making use of actual heater tracks and not an idealized circular heater plane, we remove the boundary condition of temperature or power density (for NU and U configuration heaters respectively). These two different options for generating the PCR chamber temperature are replaced by coupled Joule-heating and heat-transfer in the model. The "Electric Currents, Shell (ecs)" interface is added to the model to enable the virtual electrical connections. These are added by defining "Terminal" boundary conditions between geometry edges that require connection. A terminal condition in this manner is required for each pair of edges that must be connected. Figure 4.7(c) shows one such connection. Similarly, "Ground" and "Electric Potential" boundary conditions are applied to the ends of each group to model connections to power and ground rails.

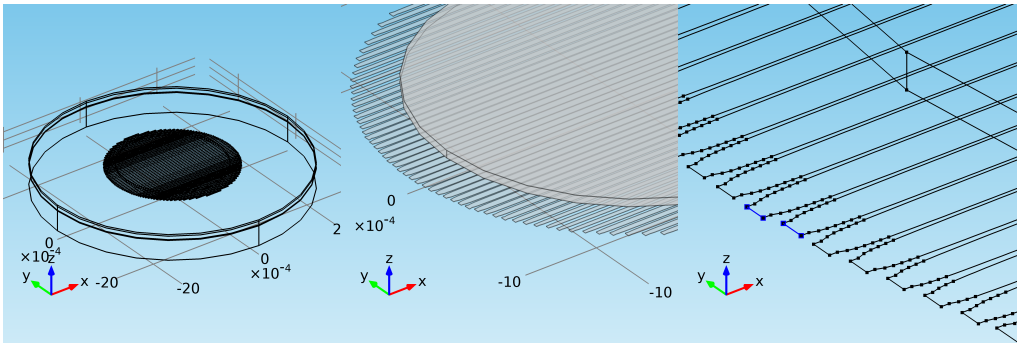

(a) (b) (c)

Figure 4.7: (a) Layout of one of the NU1450 heater design. (b) Relations between the heater and the chamber. (c) Example of one virtual connection between tracks that are part of the same group. This virtual connection will be replaced by a physical connection, or "elbow".

It should be noted that the heater is included in the 3D model as a set of 2D boundaries (tracks). The *ecs* interface allows the designer to include a thickness for the shell, which in our case was 180 nm metal thickness from sputter deposition. Such a thin component, if modeled in 3D, would cause significant difficulties in meshing the geometry. Thus, the shell interface was employed to avoid meshing issues and to maintain a low time requirement for computation.

With potential and ground nodes defined in addition to all the terminals to make virtual connections, a coupled Heat Transfer (ht) node is required to complete the Joule-heating physics. The same "Heat Transfer in Solids" physics node as was used in previous simulations is used here again. This time, the 2D heater boundaries are defined as a "Boundary Heat Source", with the power density defined by an internal variable generated by the *ecs* physics, "ecs.Qsrh" [W/m^2]. The ht interface also offers a "Highly Conductive Layer" option, for when a 2D boundary (or very thin layer) is used as a heat source, and the same heater components as included in the Boundary Heat Source node are also included here. In this way, the power generated by Joule-heating in the *ecs* physics is coupled to the heat transfer model for a fully coupled simulation.

Results from the computation show how different groups of tracks heat up differently (figure 4.8(a)). Furthermore, excellent temperature uniformity in the chamber region is demonstrated. Figure 4.8(b) shows a 2D colour plot of the PCR chamber bottom – the least uniform part of the chamber, since it is in closest contact with the heater. A 1D plot of heater and chamber bottom/top temperatures across the heater (figure 4.9(a)) shows clearly how uniform a temperature we can produce. Finally, figure 4.9(b) is a histogram of the temperature distribution in the chamber volume. Chamber temperature histograms are generated by counting the frequency of temperature values in the pyramidal mesh elements that make up the PCR chamber volume. Since this method indicates a relative volume of the chamber at temperatures near the target, it is the best metric of uniformity in our region of interest.

The next step is to connect the tracks to the power pad frame and perform a 3D simulation of the full system layout.

4.4.3.2 Part B: Physical Connections

It was established in 4.4.3.1 that the heater tracks provide the necessary power density at all locations to generate a uniform temperature volume in the chamber. However, physical connections must be made to connect the heater tracks in series and to power buses. After importing the .dxf heater file into a CAD editor of choice (in our case, Tanner EDA's L-Edit: Layout Editor) and mirroring it into the full design, the series tracks are connected with "elbows" and the tracks on the ends of groups are connected to ground or power rails. This geometry should then be checked by simulation one last

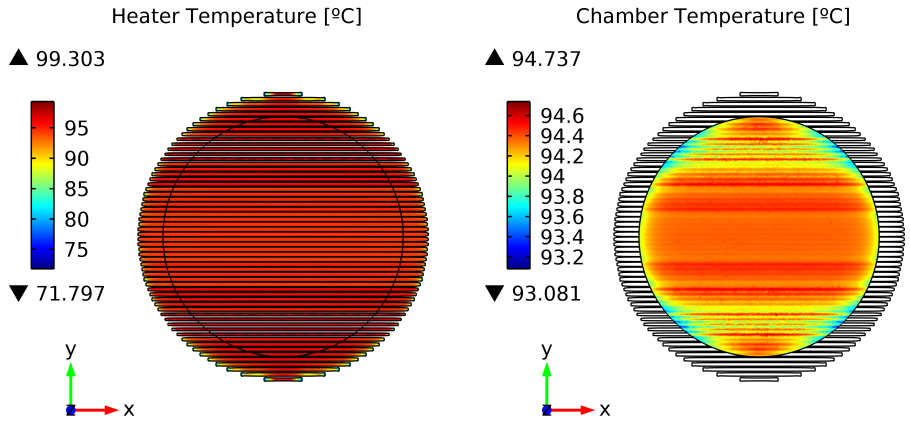

(a) (b)

Figure 4.8: 2D color plots of the NU1450 heater and chamber temperature. (a) Heater temperature. Maximum $T_h = 99.3\,^{\circ}\text{C}$, minimum $T_h = 71.8\,^{\circ}\text{C}$. (b) Chamber bottom temperature. Maximum $T_c = 94.7\,^{\circ}\text{C}$, minimum $T_c = 93.1\,^{\circ}\text{C}$

time before the photomask is printed, since mask printing is an expensive process and any changes should be made prior to committing to the design.

The 2D geometry of the connected-heater layout is exported from L-Edit as a GDS (graphic database system) format, which is supported by COMSOL. This GDS file can be imported as a layer into COMSOL's geometry environment as a work plane. Since the "Electric Currents, Shell" physics interface uses a boundary layer as its input, no extrusion is required. The power and ground connections are added to the contact pads, and the materials and boundary conditions remain the same as in the virtual connection test. This full layout replaces the virtually connected tracks from the simulation in 4.4.3.1 and is displayed in figure 4.10(a). A closer look at the connected heater shows details of the elbows in figure 4.10(b).

The heater layout has many small features, including small gaps between heater tracks and track shape features, particularly at the track tips. These small features can sometimes cause difficulties in meshing the geometry.

If after computation the heater still provides the necessary uniformity with the inclusion of track elbows, power rails and contact pads, then the verification is complete. Figure 4.11 displays another 2D colour plot of the chamber bottom, showing a great result in terms of temperature uniformity

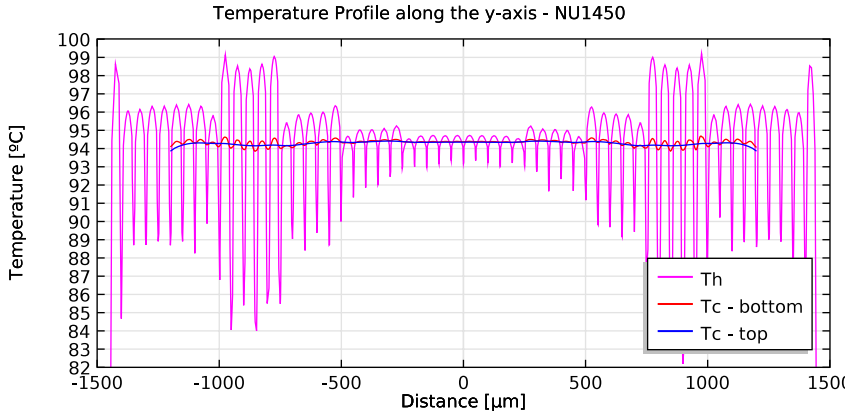

(a)

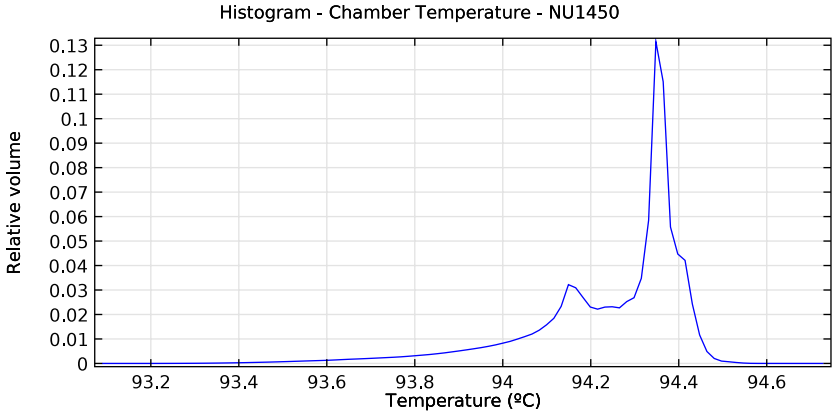

(b)

Figure 4.9: Temperature profile and histogram for the virtually-connected NU1450 heater. (a) Temperature profile along y axis. Maximum $T_c = 94.7\,^{\circ}\text{C}$, minimum $T_c = 93.1\,^{\circ}\text{C}$. Note that these extreme values may represent only a single element in the chamber volume. (b) 100-bin histogram of T_c showing that the chamber volume is 100% within $\pm 0.5\,^{\circ}\text{C}$ centered on $94.1\,^{\circ}\text{C}$.

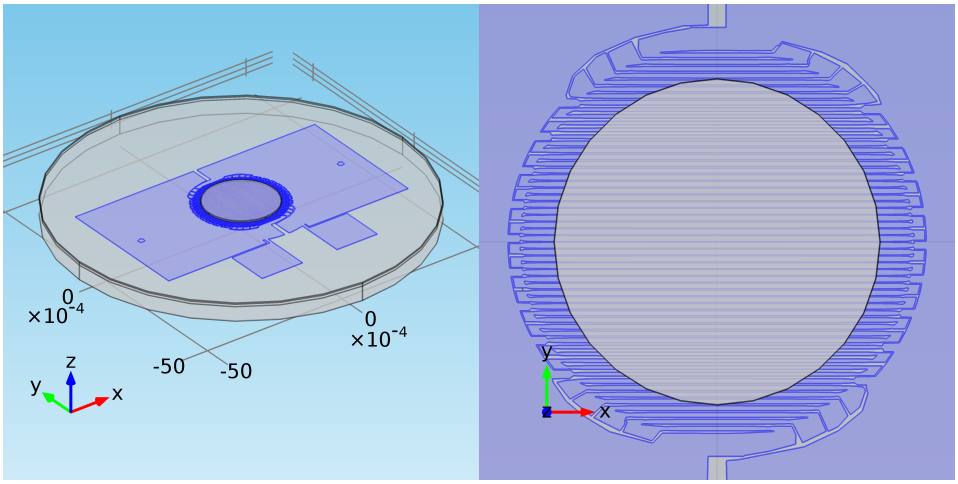

(a) (b)

Figure 4.10: (a) Final layout of the NU1450. (b) View to present the track "elbows" that connect traces into groups of odd numbers of tracks.

with the colour bar maximum and minimum at 95.8 °C and 93.8 °C respectively. Similar to the results from the virtual connection test, figure 4.12(a) shows 1D plot across the heater tracks shows the temperature ripple between heater and gap, as well as the uniformity across the chamber at the top and bottom of the volume. Finally, figure 4.12(b) confirms quantitatively that the majority of the chamber volume (98%) is within ±0.5 °C.

4.4.3.3 Accumulation of Resistance in Elbows

The problem of accumulation of resistance due to the track-connecting "elbows" of the groups was, before correction, a major source of temperature non-uniformity in the PCR chamber.

When the heater's groups were connected together in L-Edit, the elbows themselves were laid out with dimensions similar to heater track width. This caused a significant amount of power to be expended on elbows at the expense of the tracks, which was not part of the design. This caused unnecessary heating around the edge of the heater, and took away from the power required by the tracks themselves, which caused further problems in uniformity. Power expended in the elbows means that there is not sufficient power to meet the designed Q (power density) necessary to achieve the specified chamber temperature of 95 °C.

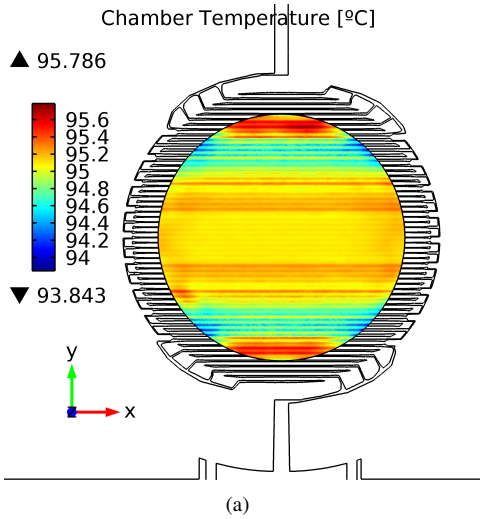

(a)

Figure 4.11: 2D colourplot of temperature at the chamber bottom (NU1450). Although temperature ripples are visible (maximum $T_c = 95.8\,°C$, minimum $T_c = 93.8\,°C$), they are within a very small range (1.94 °C) and they dissipate rapidly in the PCR fluid, as shown in the histograms of figure 4.12(b).

To mitigate this issue, the size of the elbows was increased significantly. This adjustment lowered the voltage drop across the elbows, maintaining the delivery of appropriate voltage to the heater tracks. Despite this corrective action, uniformity was not restored.

There was a discrepancy between groups in the total amount of voltage drop in all the elbows of each group. This scenario was most obvious in the U1550 heater configuration. The groups responsible for heating the y-axis "ends" of the heater appeared to be much cooler than the central groups, resulting in a significant temperature drop in a portion of the chamber, shown in figure 4.13. Since these end-groups contain the most tracks in series of any of the groups making up the heater, the accumulation of resistance (and voltage drop) in the elbows was most severe. The figure 4.14(a) colour plot of the chamber bottom shows a difference of about 4 °C between the area of the chamber above the end group compared to the middle of the chamber. With an applied voltage of 10 V to the U1550 heater, the total voltage drop in the elbows of the end and middle groups was 0.47 V and 0.16 V respectively. The uniformity was reduced by this discrepancy from our target of $\pm 0.5\,°C$ to about $\pm 2.5\,°C$. To respect the voltage requirements of the heater tracks, the length of the very last track was reduced to compensate for the increased voltage drop across the elbows. A polygon was added to the COMSOL geometry to widen the track significantly, making its resistance negligible compared to the rest of the tracks in the group. It was important to make sure that the right amount

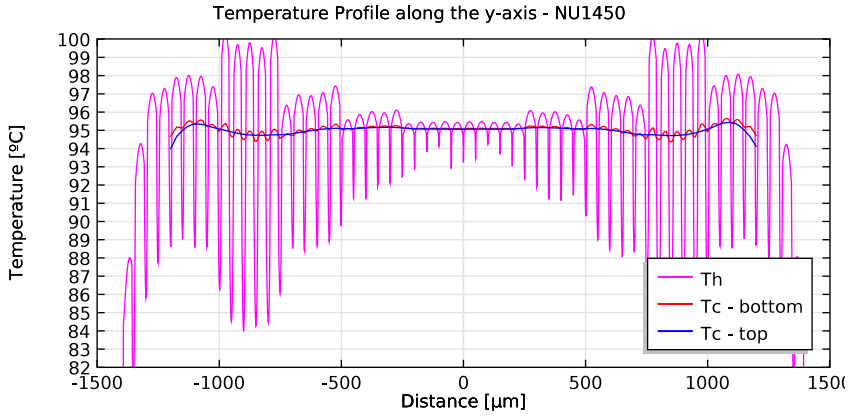

(a)

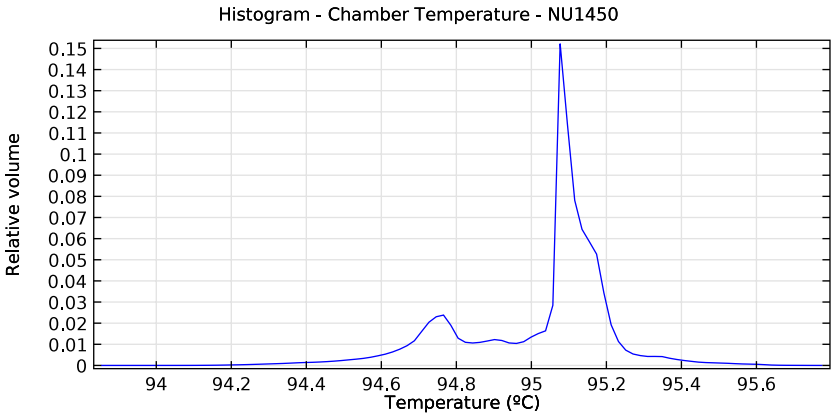

(b)

Figure 4.12: Temperature profile and histogram for the connected, full NU1450 heater layout. (a) Temperature profile along y axis. Maximum $T_c = 95.8\,^{\circ}\text{C}$, minimum $T_c = 93.8\,^{\circ}\text{C}$. Note that these extreme values may represent only a single element in the chamber volume. (b) 100-bin histogram of T_c showing that the chamber volume is 98% within $\pm 0.5\,^{\circ}\text{C}$ centered on $94.9\,^{\circ}\text{C}$.

of voltage was recouped with this method – if too much resistance was removed by widening the track, then the rest of the tracks in the group would be overpowered, resulting in a too-hot region. To determine how much of the track should be widened, the total voltage drop attributed to the elbows in each group was recorded by probing the simulation results. Since the end-groups expended a factor of 3 greater voltage than that of the center groups (0.47 V, 0.16 V respectively), the difference must be made-up to achieve uniformity. To apply the same potential difference across the end-groups and center groups, the difference in their elbow-expended voltage (0.31 V) is recouped at the ground- or power-rail connected end of the last track. The last track was probed along its length to find the location at which 0.31 V had been achieved, and the track was widened to this point, from the power/ground connected end. Figure 4.13 communicates the process visually.

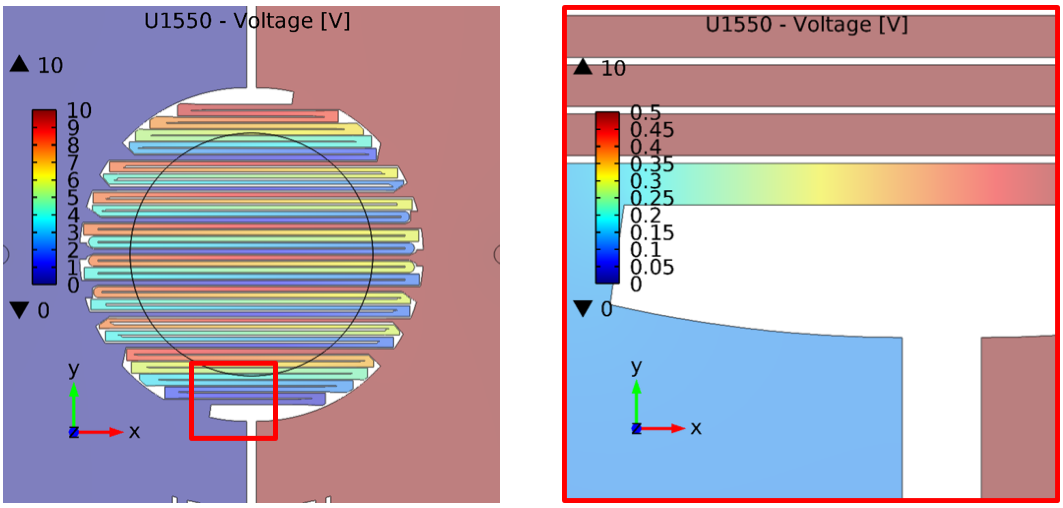

(a) (b)

Figure 4.13: Resistance in heater track "elbows". (a) Colour plot of voltage in the heater layout. (b) Zoomed image of the last track in the heater with an adjusted colour scale to show details in the frame. Probing this track in COMSOL allowed us to locate the position to which the track had to be widened to compensate for resistance accumulation in the elbows.

With the voltage drop difference eliminated, uniformity was corrected and is shown on one side of the heater in figure 4.14(b).

This procedure was performed for all four designs; to find the optimal "widened-track" point, two track correction-simulation iterations were performed for each heater. The track corrections were added to the photomask layout, ready for printing.

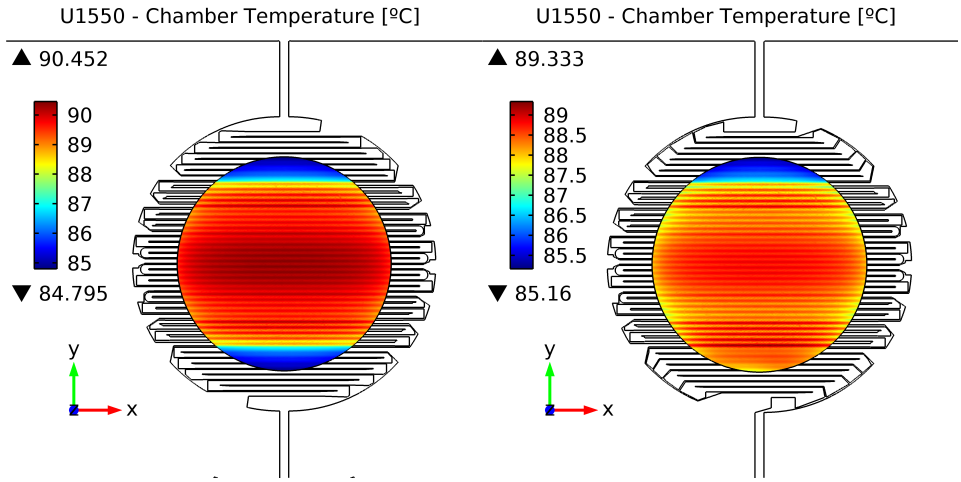

Figure 4.14: Correcting temperature non-uniformity due to "elbow" resistance. (a) No fix. (b) 2D colour plot of temperature at the bottom of the PCR chamber in the U1550 with physical connections. The voltage drop at the end group at the bottom, caused by the large number of elbows, was corrected by reducing the length of the first track. The top group was not corrected, to show the difference. The non-uniformity in this group reaches $\sim 5\,^{\circ}$C. Since power is expended in the elbows, there is not sufficient power to meet the designed Q (power density) necessary to achieve the specified chamber temperature of 95 °C, resulting in a maximum T_c of only 90.5 °C in (a).

4.4.4 Uniformity

A parametric simulation of the finalized heater layouts was done to determine what exact voltage would be required to achieve the highest target temperature of 95 °C. Once determined for each of the four heaters, chamber uniformity was explored in detail.

4.4.4.1 Steady State

The PCR chamber floor shows the worst non-uniformity in temperature since it is closest to the heater tracks. Figure 4.15 displays the chamber bottom temperature at our highest target of 95 °C for all four designs. According to these 2D colour-plots, it is expected that temperature ranges of 0.86 °C, 1.13 °C, 1.94 °C and 2.55 °C will be observed at the chamber floor in these designs. Although these ranges are greater than our 1 °C ($\pm 0.5\,^{\circ}$C) target, the majority of the heated PCR volume will not show this range, as the ripple is attenuated significantly.

Chamber temperature 100-bin histograms are presented in figure 4.16. Figure 4.16(a) displays

the results of the two small heaters for comparison (NU750 and U850), and figure 4.16(b) does the same for the large heaters (NU1450 and U1550). It is clear from these histograms that the temperature uniformity is predicted to be exceptionally good in the PCR chamber, especially for the non-uniform power density designs. For each of the four heater designs, the percentage of the chamber (from the 100-bin histograms) within 1 °C at the target temperature of 95 °C are 100% (NU750), 99% (U850), 98% (NU1450) and 94% (U1550).

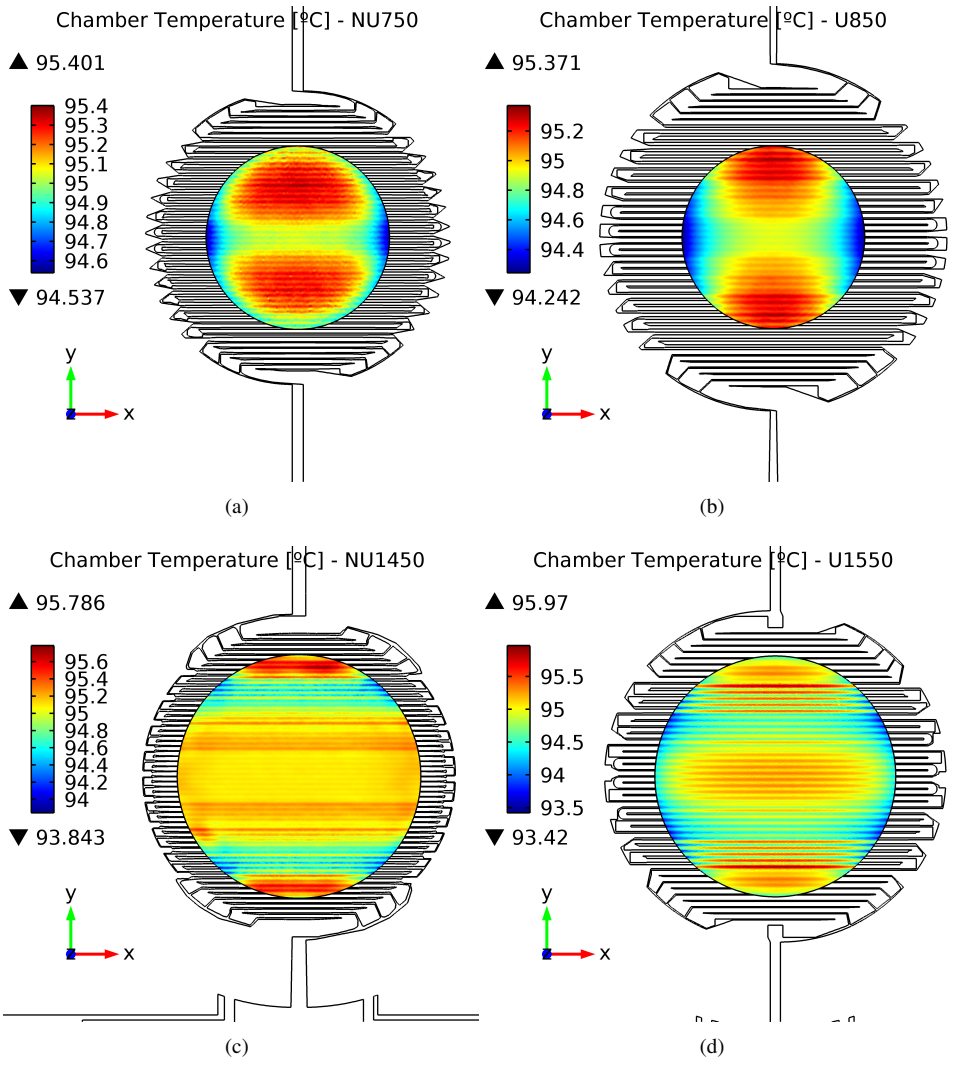

Figure 4.15: 2D colour-plots of temperature on the chamber floors of the four heater designs. (a) NU750: $T_{c-min} = 94.54$, $T_{c-max} = 95.40$, (b) U850: $T_{c-min} = 94.24$, $T_{c-max} = 95.38$, (c) NU1450: $T_{c-min} = 93.84$, $T_{c-max} = 95.79$, (d) U1550: $T_{c-min} = 93.42$, $T_{c-max} = 95.97$.

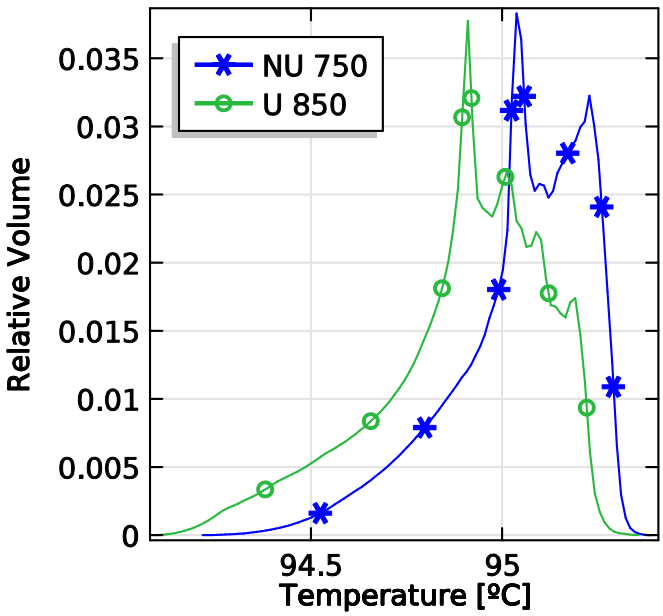

(a)

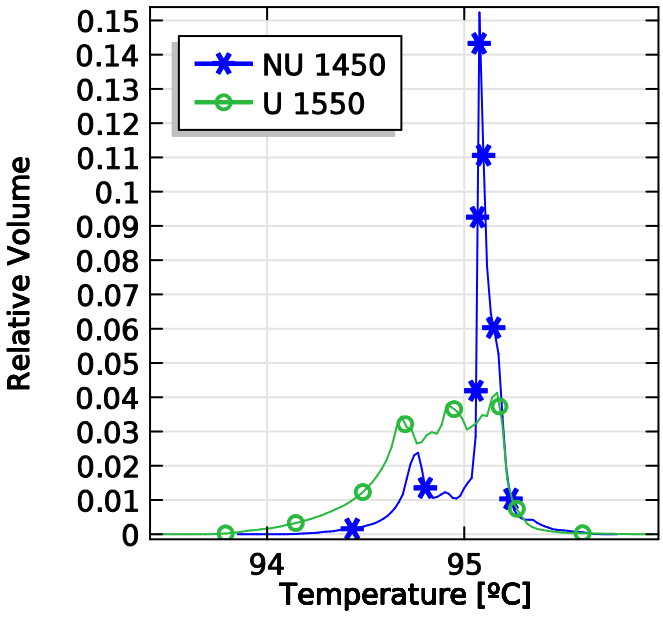

(b)

Figure 4.16: 100-bin histograms of the chamber temperature in (a) small heaters (NU750 and U850) and (b) large heaters (NU1450 and U1550). The percentage of the chamber within 1°C at the target temperature of 95°C are 100% (NU750), 99% (U850), 98% (NU1450) and 94% (U1550).

4.4.4.2 Transient

A time-dependent study was added to the NU1450 final layout model, and the transient response was simulated.

The 5τ equilibrium time is $5 \times 64.5\,\text{ms} = 0.3225\,\text{s}$, which matches with the results shown in figure 4.17(a).

The transient response of NU1450 to a series of voltage steps is shown in figure 4.17(a). A 1D plot of the temperature along a line across the heater tracks on the chamber bottom and top is shown in figure 4.17(b) for four time points: 0.05, 0.1, 0.2, and 0.5 s. It is clear that non-uniformities in the early stages of the transient occur due to the edge of the heater heating up more quickly than the center region. One interesting note is the rapid convergence of temperature between the chamber bottom and top.

A histogram showing the chamber temperature with relative volume at the same four time points is depicted in figure 4.17(c). The average chamber temperature (T_c) is defined as the volume integral of T across the chamber, divided by the total volume. Correspondingly, the average heater temperature (T_h) is defined as the surface integral of T along a surface of radius r_h on the heater plane divided by the total area.

Taken together, these results demonstrate that, in an ideal case, the heaters perform very well in achieving uniformity rapidly, opening the door to demonstrating the fastest PCR in a LOC system, ever.

4.4.5 Heater Uniformity and MCA

An important evaluation of this new thermal design is to explore what effects, if any, would be imposed on a real biological diagnostic protocol such as melt-curve analysis (MCA), which is critically dependent on temperature uniformity in the PCR chamber. Although the histograms of our simulated four heater designs show good uniformity (see figure 4.16), it is of interest to know what, if any, effects the temperature distributions will have on real MCA curves. This effect can be explored by convolving an MCA curve with the temperature histograms of our four heater designs and comparing the result to the original curve.

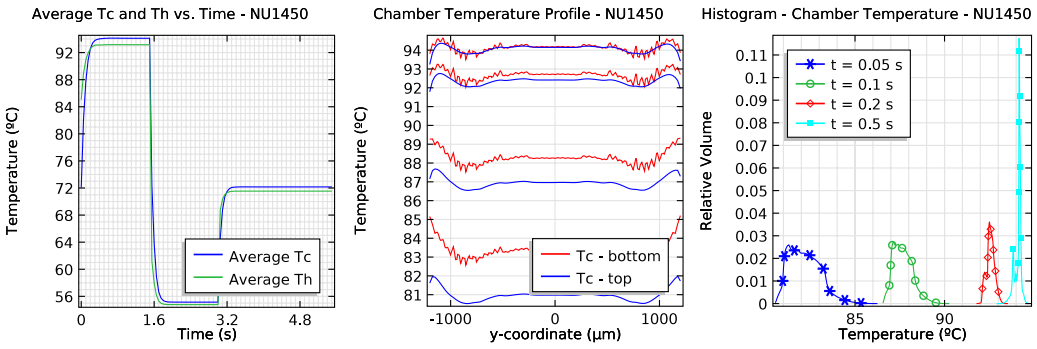

(a) (b) (c)

Figure 4.17: All three plots here refer to the NU1450 heater design. (a) T_c and T_h over time, for one generalized PCR cycle. (b) T_c at four points in time (0.05, 0.1, 0.2, and 0.5 s). (c) Histogram of the relative volume of the chamber at various temperatures along one transient.

Temperature data was exported from the closed-loop voltage COMSOL models of the final heater layouts, and was then imported into MATLAB. The *hist* operator was used to generate a histogram of the temperature data for each of the four simulated heaters. The number of bins and their centers are determined by the data extracted from an expected MCA curve. Since the uniformity is the worst case at the highest target temperature (95 °C) it is sufficient to use the histogram found at this target temperature for the convolution.

The mock MCA curve was generated by uMelt, a web-based application for predicting fluorescent high-resolution DNA melting curves of PCR products. The uMelt v2.0.2 tool is provided by The Wittwer Lab for DNA Analysis, University of Utah, and can be found at: http://www.dna.utah.edu/umelt/umelt.html. Table 4.3 lists the parameters used for this test. The sequence for the human beta-2-microglobin gene was used as a sample for this test, since it has been targeted by our lab in the past. The sequence applied to this test was:

ATGTCTCGCTCCGTGGCCTTAGCTGTGCTCGCGCTACTCTCTCTTTCTGGCCTGGAGGCT

ATCCAGCGTACTCCAAAGATTCAGGTTTACTCACGTCATCCAGCAGAGAATGGAAAGTCA

AATTTCCTGAATTGCTATGTGTCTGGGTTTCATCCATCCGACATTGAAGTTGACTTACTG

AAGAATGGAGAGAGAATTGAAAAAGTGGAGCATTCAGACTTGTCTTTCAGCAAGGACTGG

TCTTTCTATCTCTTGTACTACACTGAATTCACCCCCACTGAAAAAGATGAGTATGCCTGC

CGTGTGAACCATGTGACTTTGTCACAGCCCAAGATAGTTAAGTGGGATCGAGACATGTAA

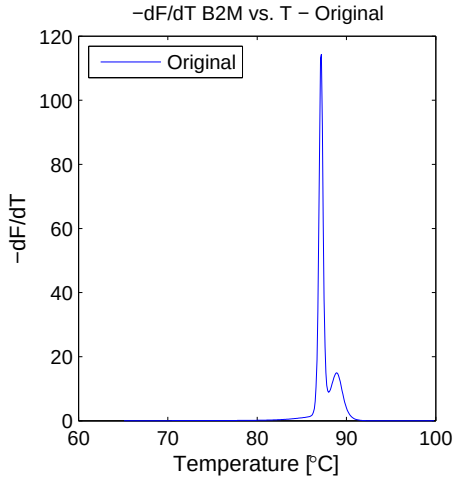

(a)

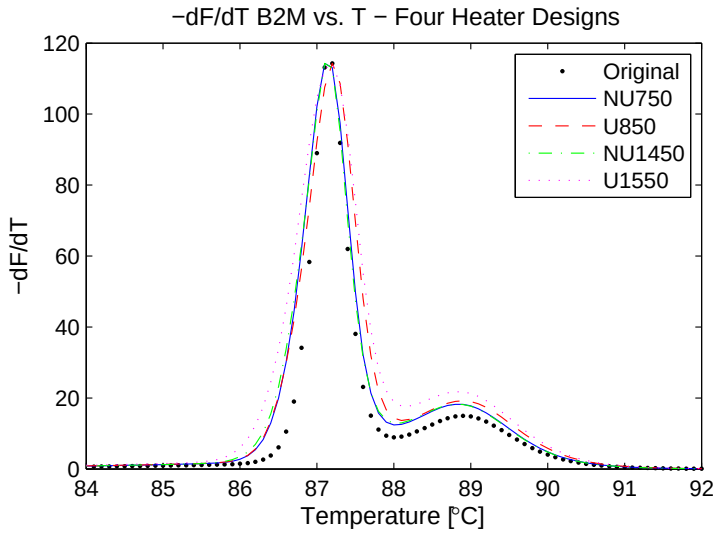

(b)

Figure 4.18: Effect of temperature uniformity on melting curve analysis. (a) uMelt negative first derivative of original fluorescence data for *B2M* melt-curve analysis. (b) Negative first derivatives of the numerical convolutions of all four heater temperature distribution histograms with the original fluorescence data.

Table 4.3: uMelt parameters. All parameters except for data resolution are the default settings. The data resolution was increased to provide a smoother plot.

Parameter	Value
DNA Sequence	Homo sapiens (human) beta-2-microglobin
[Mono^{+}]	20 mM
free [Mg^{++}]	2 mM
DMSO %	0%
Temperature range	65 – 100 °C
Data resolution	0.1 °C
Thermodynamic Set	Unified-SantaLucia (Natl. Acad. Sci., 1998)

The convolution between the uMelt results and the simulated heater histograms was done in MATLAB R2012a, using the *conv* operator. The raw fluorescence data from the uMelt curve is convolved with each of the heater's temperature distribution histograms. These data sets are then differentiated numerically to produce the rate of change in fluorescence vs. temperature plots commonly seen in MCA, and are standardized to match the uMelt scale. The original uMelt negative derivative of fluorescence curve is plotted in figure 4.18(a). The negative derivative is commonly used to identify the 50% dissociation point of the sample, indicating its "melting temperature". Melting temperatures of products are compared to controls to diagnose a sample. Figure 4.18(b) shows the results of all four heaters on one plot, and each heater is also plotted against the original individually in figure 4.19.

It is clear from figures 4.18 and 4.19 that the chamber uniformity is sufficiently good; since the histogram data approximates an impulse function, very little deterioration of the original MCA data occurs. Most important is the location of the peak on the temperature axis, which is practically unchanged in this simulation. Thus, our system should prove to be reliable (assuming good calibration) for MCA.

4.4.6 PCR Speed

One of the fastest thermal systems for rapid PCR was demonstrated by Wheeler *et al.* in [1], in which a sub-three minute PCR on a 5 µL volume was achieved. To make their reactions as rapid

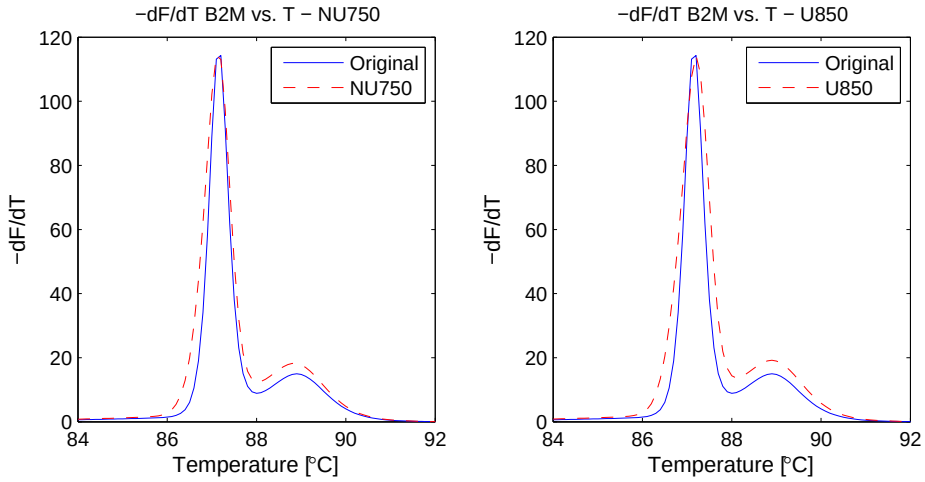

Figure 4.19: Negative first derivative of fluorescence from the convolutions with each of the four heater designs.

as possible, Wheeler *et al.* investigated two different rapid PCR polymerases: SpeedSTAR^{TM} HS DNA Polymerase (Takara Bio Inc.) and KAPA2G Fast PCR Enzyme (KAPA Biosystems). Both of these polymerases are specially designed to be used in fast PCR protocols.

The above two polymerases were used by Wheeler *et al.* to amplify two targets: a 58 bp target of genomic *pantoea enterobacter agglomerans* (otherwise known as *erwinia herbicola*, *Eh*) and a 107 bp synthetic SARS oligomer target. The KAPA2G polymerase was used only on the Eh target to produce two amplicons - the 58 bp target and an additional 160 bp target.

The LOC system in [1] was programmed to amplify the targets via several different cycle time variations. For the agarose gel electrophoresis results shown in figure 4.20(a), the total amplification times were 2 : 50 s and 3 : 18 s for Eh and SARS targets, respectively. Although it is clear that the SARS target was only amplified by the SpeedSTAR polymerase, it is unclear which polymerase was used to amplify the Eh target. A comparison of band strength with respect to the total number of PCR cycles (varied from 30-45 cycles) is shown in figure 4.20(b).

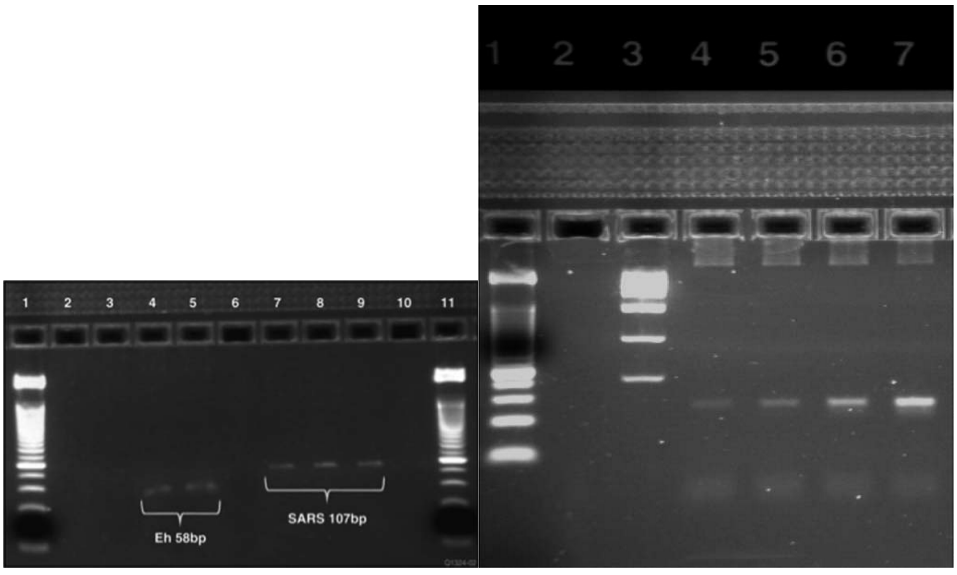

(a) (b)

Figure 4.20: Agarose gel electrophoresis results. (a) Agarose gel electrophoresis showing amplification of Eh (2 min, 50 s) and SARS (3 min, 18 s) amplicons. (b) Agarose gel electrophoresis of KAPA2G-generated Eh amplicon comparing cycle number and band strength. $n = 30, 35, 40, 45$ for lanes 4-7 respectively. Band strength (brightness) increases with then number of cycles. Reproduced in part from [1] with permission of The Royal Society of Chemistry http://dx.doi.org/10.1039/c1an15365j.

4.4.6.1 Two-Step PCR in [1]

Recall from section 2.1.2 that PCR usually consists of three steps: denaturation, annealing, and extension. The PCR programs employed in [1] were simplified PCR sequences of only two steps. That is, the thermal cycling consisted of only two temperature targets, which were alternated. Figure 4.21 shows a plot of temperature versus time for a typical PCR program in their device. Two different cycling programs were presented that each have a total PCR time of $2:50\,\text{s}$, and they are listed in table 4.4. Average temperature parameters were $90\,^{\circ}\text{C}$ for denaturation and $45\,^{\circ}\text{C}$ for annealing. Note that there are no "hold" times associated with the two target temperatures at all; the annealing and extension times reported in [1] and reprinted in table 4.4 are made up of temperature transitions. That is, an acceptable range of values around the target temperature was used in [1] to define the time spent at each of the two targets.

The PCR device in [1] was calibrated to determine that the reference temperature (the temperature of a large, copper block) was within $2\,^{\circ}\text{C}$ of the PCR mixture during temperature cycling. Following this calibration, the annealing and extension times in table 4.4 were defined as the time that the block temperature was within given ranges. For the annealing time, this range was "$50\,^{\circ}\text{C}$ or below", and for the extension time, the range was "$70\,^{\circ}\text{C}$... to $80\,^{\circ}\text{C}$" inclusive.

The standard protocols for the two polymerases used in [1] are shown in table 4.5. The shortcut in thermal cycling that [1] employed is obvious when the times for each step are compared to the standard protocols: annealing in the standard SpeedStar protocol is $10\,\text{s}$, and in Program 2 (35 cycles) of [1] it is $0.84\,\text{s}$. Similarly, extension is $5\,\text{s}$ in the standard SpeedStar protocol and in Program 2 of [1] it is $0.44\,\text{s}$.

The lack of explicit hold times is acceptable for the application presented in [1] (very small-length products that take very little time to be replicated in the extension step). For longer amplicons (e.g, thousands of base-pairs long), dedicated hold times would certainly be necessary to allow time for the polymerase to replicate the target. With this in mind, the heaters presented in this thesis work offer a solution to this hold-time problem while maintaining an exceptionally low PCR cycle time. This concept is discussed further in the following section.

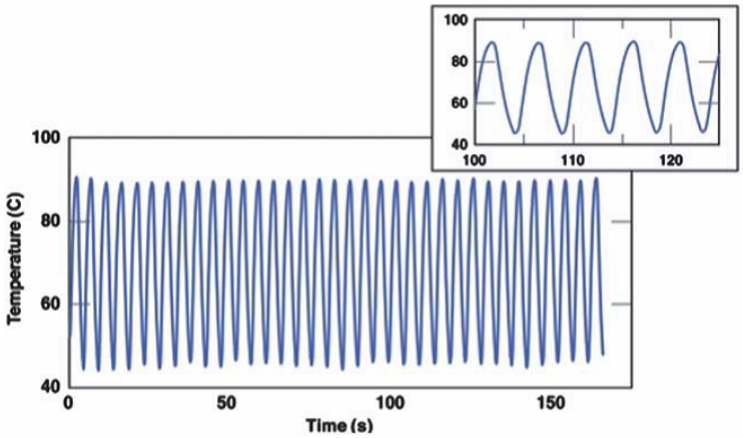

Figure 4.21: 35-cycle thermal trace in LOC device discussed in [1]. Reproduced in part from [1] with permission of The Royal Society of Chemistry http://dx.doi.org/10.1039/c1an15365j.

Table 4.4: Two cycling programs for fast PCR employed in [1]. It is not clear which program was used for generating the products shown in the gel electrophoresis figures presented in [1]. Reproduced in part from [1] with permission of The Royal Society of Chemistry http://dx.doi.org/10.1039/c1an15365j.

Two cycling programs in [1]	**Program 1**	**Program 2**
Total PCR time (min : s)	2 : 50	2 : 50
Number cycles	30	35
Annealing time (s)	1.43	0.84
Extension time (s)	0.38	0.44
Average cycle time (s)	5.55	4.4
N	21	23

4.4.6.2 Three-Step PCR in our Microfluidics-CMOS Integrated LOC Thermal System

The most conservative operating time estimate for UA heaters comes from operation without a controller. For the UA thermal systems, $\tau = 64.5\,\text{ms}$, so five time constants is $0.3225\,\text{s}$. Even taking the conservative estimate that this ramp time does not contribute to any of the PCR steps, there is still room to complete a 3-step PCR cycle including hold-times at the target temperatures. The introduction of hold-times is a significant improvement over [1], in which only two temperature targets were used and with no hold-time allocation at all. Depending on optimization of the biology in improving PCR efficiency (e.g., hot start, final deletion, adjusting the ratio between the three steps) we can easily still achieve the same or better than the total PCR time discussed in [1].

Table 4.5 compares the 3-step SpeedSTAR and KAPA2G protocols to two proposed protocols for running our new chips. It is easy to see that with our exceptionally fast ramp time we are able to achieve much longer hold times at each step than what was done in [1]. If the standard protocols (i.e., the manufacturer-recommended hold-times) for the two fast-PCR polymerases SpeedSTAR and KAPAG2 are followed, our system can complete 35 cycles in under 13 minutes. Figure 4.22 shows what a 3-step PCR cycle would look like in the NU1450 heater if the proposed SpeedSTAR protocol was employed.

Table 4.5: Standard protocols and reduced, rapid protocols for SpeedSTAR and KAPA2G polymerases, as applied to our thermal system. The ramp value is 5τ, or $0.3225\,\text{s}$, and is multiplied by 3 in the total cycle time (one for each temperature change).

	SpeedSTAR Standard	**KAPA2G Standard**	**SpeedSTAR UA**	**KAPA2G UA**
Denature (s)	5	10	1	2
Anneal (s)	10	10	2	2
Extend (s)	5	1	1	1
Ramp (s)	0.32	0.32	0.32	0.32
Cycle Time (s)	20.97	21.97	4.97	5.97
Cycles (n)	35	35	35	35
Total Time (s)	733.86	768.86	173.86	208.86
Total Time (min:s)	12:14	12:49	2:54	3:29

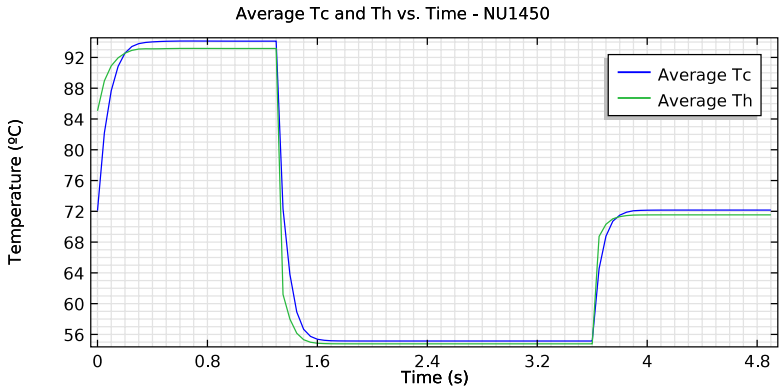

Figure 4.22: T_c and T_h transients for 1 PCR cycle of the proposed "SpeedSTAR - UA" protocol from table 4.5. This data was generated in a full 3D transient simulation.

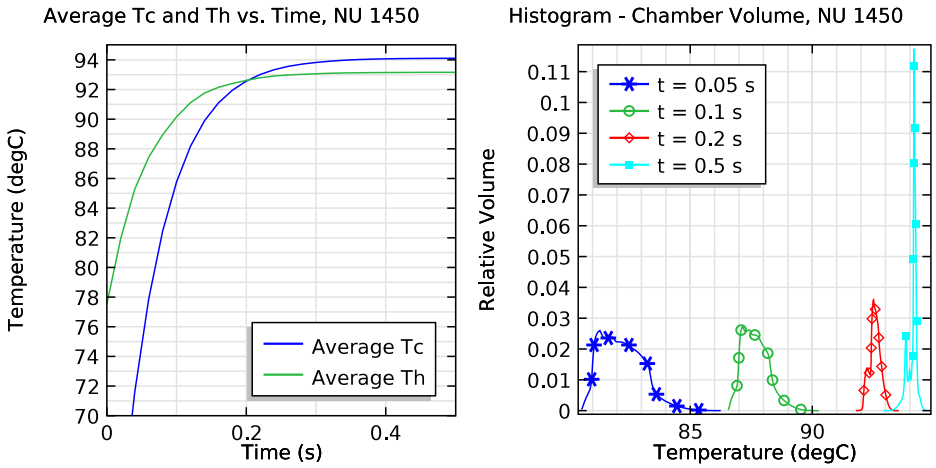

(a) (b)

Figure 4.23: Early transient response of the NU1450 heater. The plots in (a) and (b) cover the same range of time. It is easy to see here that the chamber temperature and uniformity converge to their targets (95 °Cand 1 °C respectively) very quickly (less than 0.5 s).

If we define three time constants ($1 - 1/e^3 = 0.9502$, or 95% of target) acceptable as our equilibrium time ($3\tau = 193.5$ ms), then we reduce the SpeedSTAR cycle time from 4.97 s to 4.58 s, and the overall PCR time from 174 s to 160 s. This makes our 35-cycle, true 3-step PCR both faster than the demonstrations presented in [1] as well as closer to standard protocol, in that hold-times are performed at the target temperatures. The worst case error in temperature at 3τ is 4.75 °C, or in other words, an active denaturation step starting at 90.25 °C. Additional time-savings can be attained by

applying a controller to the heater power, and this is discussed briefly in the following section.

4.4.6.3 Closed-Loop Response

The previous section presented details on the generalized open-loop operation of the heater system. It was shown that with an equilibrium time of 0.19 s (3τ), the ramp time represents only 12.7% of the total cycle time (0.58 of 4.58 s). Though the gains are limited, the addition of a controller for operation of the heating element could reduce the cycle time even further.

One way to estimate the best case that a controller could provide is to consider "full-power rise" and "zero-power fall" times. A full-power rise is achieved by applying the maximum allowable power to the heating element, and conversely a zero-power fall is performed by removing all power to allow maximum cooling of the element.

The time constant for each of these two conditions can be calculated as follows:

$$\text{For a full-power rise: } T_{(t)} = T_{min} + (T_{max} - T_{min})\,(1 - \exp(-t/\tau)) \quad \text{where } T_{(0)} = T_{min} \tag{4.3}$$

$$\text{For a zero-power fall: } T_{(t)} = T_{max} + (T_{min} - T_{max})\,(1 - \exp(-t/\tau)) \quad \text{where } T_{(0)} = T_{max} \tag{4.4}$$

Where T_{min} is the minimum temperature of the heater (i.e., the same temperature as the heatsink) and T_{max} is the maximum temperature that the heater is to achieve.

The work of Dr. Jose Martinez-Quijada in [91], concurrent to the work herein, presented a transfer function based on a one-dimensional thermal model of the heater system, which was shown to have good agreement with the COMSOL simulations used in this work. That transfer function and its constants are shown here:

$$TF = R_d \frac{as+1}{bs^2+cs+1} \tag{4.5}$$

Where

$$
\begin{aligned}
a &= C_m R_c \\
b &= C_c C_m R_c (R_2 + R_c) \\
c &= C_c (R_2 + R_d) + C_m (R_2 + R_d + R_c)
\end{aligned}
$$

and

$$
\begin{aligned}
C_c &= 33.27 \times 10^{-5}\,\mathrm{J\,K^{-1}} \\
C_m &= 17.18 \times 10^{-5}\,\mathrm{J\,K^{-1}} \\
R_2 &= 56.59\,\mathrm{K\,W^{-1}} \\
R_c &= 37.84 \times 10^{-5}\,\mathrm{K\,W^{-1}} \\
R_d &= 56.59\,\mathrm{K\,W^{-1}}
\end{aligned}
$$

For the transfer function shown in equation 4.5, $\tau = 0.0568\,\mathrm{s}$. Rearranging equation 4.3 and using τ to solve for t at $T = 94\,^{\circ}\mathrm{C}$, we get a time of $t = 0.1316\,\mathrm{s}$ for the full-power rise from $30\,^{\circ}\mathrm{C}$ to $94\,^{\circ}\mathrm{C}$. Similarly, rearranging equation 4.4 for a zero-power fall from $94\,^{\circ}\mathrm{C}$ to $30\,^{\circ}\mathrm{C}$ yields $t = 0.0568\,\mathrm{s}$. If these rise and fall times are used in the SpeedSTAR cycle time calculation, the ramping/falling time is reduced to just $0.19\,\mathrm{s}$ per cycle (down to 4.5% from 12.7%). Over the course of a 35-cycle PCR run, a $4.19\,\mathrm{s}$ cycle amounts to just $147\,\mathrm{s}$, or just under two and a half minutes.

To conclude, a UA heater being run under closed-loop conditions could perform a 35-cycle PCR in two and a half minutes using the SpeedSTAR polymerase. This work effectively shifts the paradigm of PCR time limitation from one dictated by temperature ramping time to one limited by the replicating speed of the selected polymerase, and the length of the amplicon.

4.5 Experimental Results and Discussion

4.5.1 Fabricated Device

The devices were fabricated by Matt Reynolds ([92]) in the University of Alberta NanoFab facility. Figure 4.24 displays four photos, one of each of the four heater designs.

4.5.2 Calibration

Our methods for microfabricating thin-film Al metal heaters on KMPR polymer are described in [80, 93]. Variations in small-batch processing means that some type of calibration for the devices is necessary, if results are to be trusted - an essential requirement of LOC technology.

The fabricated heaters, shown in figure 4.24 were diced by a diamond-tipped dicing saw (Diamond Touch Technology Inc.) and placed on an aluminum heat sink with thermal paste (T630 THERM-A-GAP Dispensed Thermal Gel, Parker Chomerics) to ensure good thermal contact between the Si and Al surfaces. In turn, the Al heat sink (72.5 mm $\times$ 40 mm $\times$ 6.5 mm) was affixed to the surface of a Torrey Pines Scientific EchoTherm™ HS40 hotplate using the same thermal paste as above. A custom-designed PCB with spring-loaded Au-coated 1 mm diameter-tip pogo pins (Interconnect Devices Inc.) was used to contact the terminals of the heaters. The hotplate was used to heat the entire Al block and chip to a known temperature, and resistance was measured with an HP-34401A (Hewlett Packard) multimeter in 4-wire mode. Taken on ramp-up and -down at 25 °C, 40 °C, 60 °C, 80 °C, 100 °C, these nine measurements were used to construct a resistance versus temperature curve. The slope of this curve was used to calculate the TCR of the metal by using a geometric factor determined from the heater design.

As expected from simulation, linear behaviour for the resistance-temperature curve was demonstrated. As shown in figure 4.25, the simulated linear curve was a factor of two lower in resistance than what was observed empirically. The slope, however, remains very close to the same; $0.0332\,\Omega\,^{\circ}\mathrm{C}^{-1}$ for the calibration curve and $0.0296\,\Omega\,^{\circ}\mathrm{C}^{-1}$ for the simulation. The full linear equations are:

$$R = 0.0332(T) + 15.419 \qquad \text{Calibration}$$

$$R = 0.0296(T) + 7.662 \qquad \text{Simulation}$$

Note that despite collecting data on both a heating and cooling cycle, the only temperature at which resistance showed a noticeable difference was room-temperature. This high repeatability is explored further in section 4.5.3 below. The difference between the expected (simulation) and

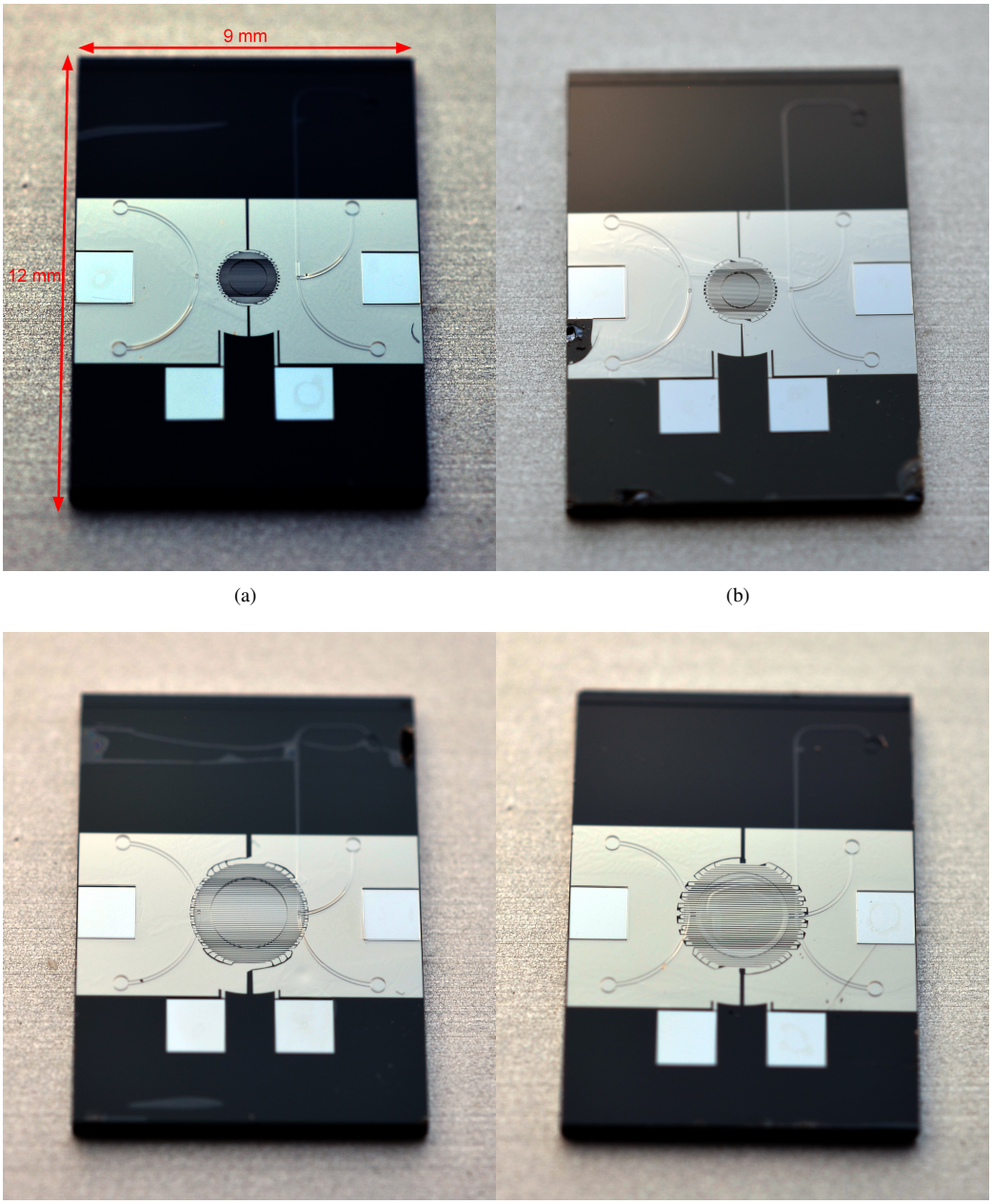

(a) (b)

(c) (d)

Figure 4.24: Four in-house fabricated heater designs. (a) NU750, (b) U850, (c) NU1450, (d) U1550. The dimensions of the die are the same in all four pictures. Note the convenient standard layout is maintained, and the heater design only is changed between devices.

measured (calibration) heater resistance curves is attributable to variations in metal deposition. It was found by simulation that despite this significant change in resistance, the temperature uniformity in the chamber did not suffer. Useful aspects of the base resistance being twice the expected value are presented in section 4.5.4.

From these results it is reasonable to expect that one chip per fabrication batch could be calibrated in this manner to account for any changes in the deposition.

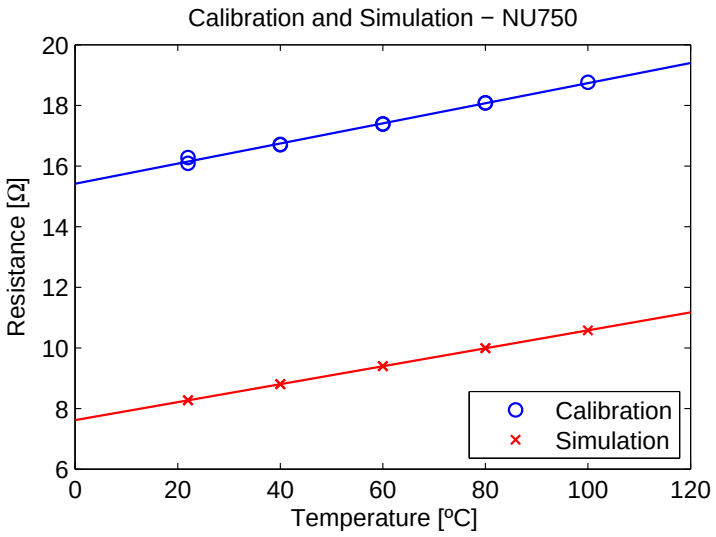

Figure 4.25: Heater resistance (R) versus temperature (T) from calibration and simulation. Note the remarkable consistency in slope, but the significant difference in intercept. The difference is attributable to metal deposition variation in thickness and resistivity. More information on the metal deposition can be found in [92].

4.5.3 Repeatability

The repeatability of our heater/sensor system is good. Fitted linear curves and the data points from five identically administered runs on one NU750 chip are shown in figure 4.26. Note that the test repeated here has exactly the same experimental conditions and method as described in section 4.5.2, above. Clearly there is significant overlap between the tests. The average chamber temperature and standard deviation of the five runs, per the simulation curve, was $99.6 \pm 0.1\,^{\circ}\mathrm{C}$, but the calibration equation shows that, in fact, the heater generated $131.1 \pm 0.78\,^{\circ}\mathrm{C}$. Comparing the linear regressions for the five runs in table 4.6 clearly shows the repeatability and stability of the heater at temperatures that far exceed what is necessary for doing PCR. The results found here agree

with what was obtained and published in [80].

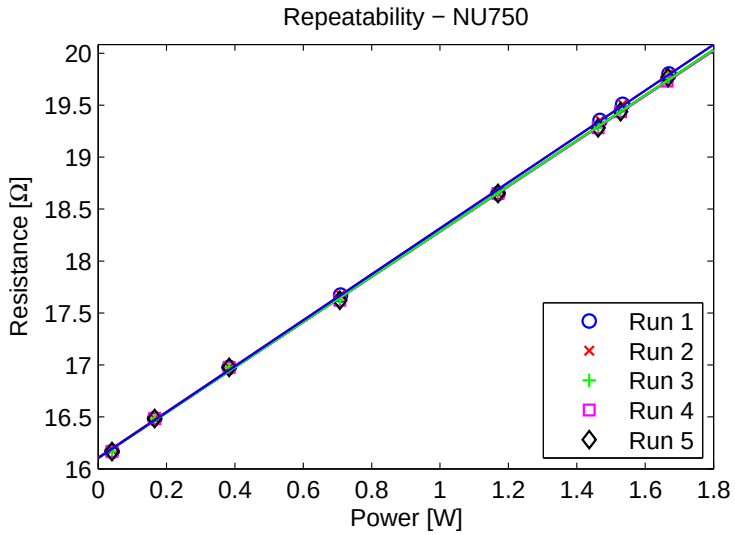

Figure 4.26: The NU750 showed excellent repeatability for five runs of ramping power up to a maximum operating temperature. Each run was fitted with a linear equation, with coefficients listed in table 4.6. Experimental conditions and method for these runs were exactly the same as those described for the calibration procedure, section 4.5.2 and figure 4.25.

Table 4.6: Five runs of the same NU750 chip. Linear regressions applied to each run show excellent fitting and consistency between runs. Experimental conditions and method for these runs were exactly the same as those described for the calibration procedure, section 4.5.2 and figure 4.25.

Run	**Slope (m)** $\sigma = 0.015$	**Intercept (b)** $\sigma = 0.0017$	R^2
1	2.2113	16.104	0.9998
2	2.2076	16.108	0.9998
3	2.1823	16.105	0.9997
4	2.1749	16.108	0.9998
5	2.1823	16.105	0.9997

4.5.4 Lifetime Testing

Higher temperature and high current density can cause electromigration and compromise proper operation of the heaters. It is important to ensure that the metal layer which is used in our KMPR-

on-CMOS process is suitable for our heater/sensor purpose. Moreover, our in-house prototypes must be able to withstand our power requirements for at least as long as a PCR test in order for us to generate useful results that will help design the next generation of heaters in CMOS. Of the four designs, the NU750 heater in particular is at the highest risk since it functions with the highest current density.

We previously demonstrated that our sputtered Al on KMPR can support $7.8\,\mathrm{mA\,\mu m^{-2}}$ for six hours at 165 °C without succumbing to electromigration damage significant enough to cause a measurable change in resistance [80].

Our recently-designed lifetime testing procedure for the heaters is an automated system that applies current through an element and measures resistance in four-wire mode. Experiments were performed by David Sloan, Matt Reynolds and the author. With a temperature-resistance curve for the element of interest, the system increases the current until it reaches a target resistance-temperature point. As resistance increases with electromigration occurring, the system adjusts its current input to preserve the set target resistance, attempting to hold a temperature until failure. With this method, we tested a simple single track in the on-KMPR metal for our CMOS process as well as the in-house fabricated heaters.

In $10\,\mu\mathrm{m} \times 100\,\mu\mathrm{m}$ (cross section) CMOS Al tracks on KMPR, a failure time of 145 min was measured from a constant current density of $57.5\,\mathrm{mA\,\mu m^{-2}}$ at 120 °C. This lifetime is beyond what is necessary to sustain a PCR reaction in our LOC system, as shown in section 4.4.6.

The NU750 was selected to demonstrate device lifetime, since it should fail the most quickly of the four heaters designs presented in this work. The chip was placed on an aluminum block to act as a heat sink, matching the boundary condition of the simulation. The sputtered aluminum thickness was measured at 180 nm, and a low melting temperature (62 °C) solder known as Field's metal, (Rotometals.com) composed of 32.5% Bi, 51% In, and 16.5% Sn, was used to improve the physical robustness and electromigration resistance of the thin-film heater pads (visible in figure 4.24). The device pads were then connected to a power supply via spring-loaded pogo pins (Digi-Key Corp.).

The target resistance/temperature was set to 95 °C (11.43 Ω), as determined by the calibration procedure discussed in section 4.5.2. To maintain the resistance and associated temperature of the NU750 heater, current and voltage were controlled. Current was recorded as 0.314 A and voltage as 3.59 V when the system was in steady state at the target resistance. This current is slightly lower than expected from simulation (332 mA) which can be attributed to noticeable processing

variation; the aluminum-on-KMPR of the fabricated devices was found to have a resistivity and TCR of $12.7 \pm 0.2\ 10^{-8}\,\Omega\,\mathrm{m}$ and $2.07 \pm 0.02\ 10^{-3}\,\mathrm{K}^{-1}$ instead of the expected $4.39 \pm 0.16\ 10^{-8}\,\Omega\,\mathrm{m}$ and $3.52 \pm 0.059\ 10^{-3}\,\mathrm{K}^{-1}$ from [80]. This power level was held for 41 h and 25 min, at which point the first failure occurred. It is noteworthy that 41 h equates to 1004 times the estimated controller-implemented 35-cycle protocol of 147 s, discussed in section 4.4.6. This first failure caused the current and voltage to reduce to 0.247 A and 2.83 V respectively to maintain the 11.43 Ω target resistance. The heater went on to complete failure (open circuit) after an additional 8 h and 35 min. Figure 4.27 shows a dark field microscope image of what we believe to be one of the failure points in the heater. There appears to be damage (bright spots) in the regions of the tracks that experience the highest current densities, and therefore highest electromigration. These voids could cause the open circuit that defined the device lifetime.

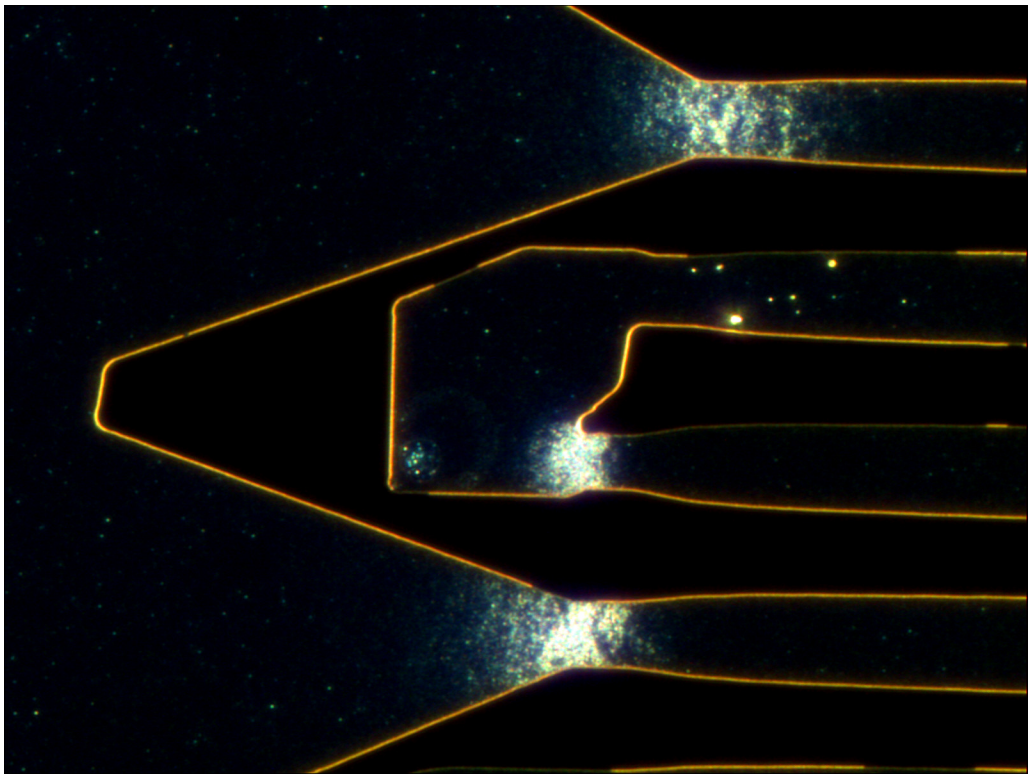

Figure 4.27: NU750 operated in the lifetime test, imaged under a dark-field microscope (oblique illumination yields images that only capture light diffracted by the sample). Bright spots are presumably caused by electromigration damage, and were found where current density is highest. A version of this image appears in [92].

The higher resistivity found in our latest fabrication is actually advantageous for the system since it allows for a lower current to deliver the target power. This means that the current density is lowered, thereby reducing damage due to electromigration. Although the processing variation seen here has an impact on the operating voltages of the heaters, it was found by simulation that it does not impact the chamber temperature uniformity.

By extrapolating the results found here, we know that all three of the other heater designs will have longer lifetimes since they boast lower current densities than what is found in the NU750. This work serves as a demonstration of Al as a successful alternative to expensive noble metals for the purpose of fabricating heaters/sensors in LOC devices. Moreover, the results of this test are important in considering the cost of research; in order to debug problems and make the best use of expensive fabrication time, these in-house devices must last longer than they are ultimately intended. This concept is discussed further in section 5.3.

4.5.5 Infrared Camera Imaging

A FLIR SC5600-M (FLIR Systems Inc.) infrared camera, equipped with a microscope lens, was used to image the powered NU750 and U1550 heaters to demonstrate temperature uniformity. A regulated DC current was applied to the heaters to induce the Joule heating with the same 4-point resistance measurement scheme used in the calibration and repeatability tests. The experiments were recorded at 30 fps. Exceptional selectivity at PCR temperatures ($\sim 100\,^{\circ}$C for the NU750 and $\sim 60\,^{\circ}$C for the U1550) was demonstrated; figure 4.28 shows thermographs of the heaters at room-temperature and under power. The rapid decay at the edge of the heater should be noted, confirming the selectivity simulated and shown in figure 4.12(a) for the NU1450 design. Uniformity in the chamber is also clear, although there are some complications to consider.

The NU750 used in the infrared imaging tests (figures 4.28(a) and 4.28(c)) was fabricated with the fourth (topmost) layer left unpatterned. This configuration essentially replaces the polypropylene membrane from figure 4.1 with KMPR to form an air-filled, closed chamber. The thick polypropylene layer shown in figure 4.1 is part of the chip-to-world interface that is currently being designed, and was not necessary to include in this imaging test. Alternately, the U1550 was imaged without a membrane layer (figures 4.28(b) and 4.28(d)), leaving the PCR chamber open

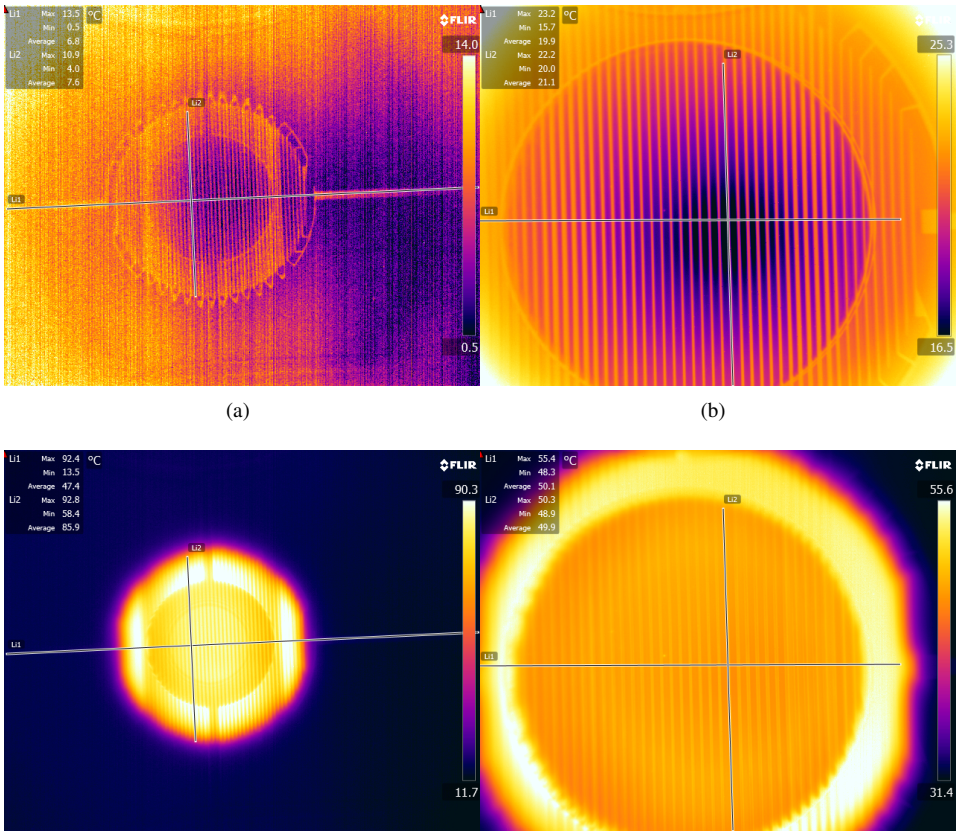

(a) (b)

(c) (d)

Figure 4.28: Infrared thermographs of the large, uniform power density heater U1550 and the small, non-uniform power density heater NU750. (a) NU750 power off, room temperature. (b) U1550 power off, room temperature. (c) NU750 power on, $\sim 100\,^{\circ}$C. (d) U1550 power on, $\sim 60\,^{\circ}$C. The NU750 was driven with 1.85 W, and the U1550 with 3.34 Wpower. Both heater designs show temperature uniformity and selectivity matching simulation. The transparency of air in the chamber and partial transparency of KMPR allows the observation of the temperature ripple on the metal layer below. This ripple agrees with what was seen from simulation (NU1450 example shown in figure 4.12(a)). The temperature ripple dissipates through the KMPR layers and in the chamber. The hotter annulus surrounding the PCR chamber is an optical artifact.

to air during the experiment. It was simulated that neither of these configurations would alter the expected temperatures of the heaters.

Visible in figure 4.28 is a hotter annulus region around the chamber. Several factors contribute to this artifact; the partial transparency of KMPR and the different emmisivities of the materials making up the system cause this interesting distortion. Simulation of the imaged chips indicate that there is no reason for the area immediately outside the radius of the chamber to be hotter than the chamber itself, supporting the optical artifact hypothesis. Indeed, it is unreasonable to believe that such a sharp change in temperature would occur along the length of a single track that has not undergone a change in dimension. This is clear in the images - even along a single track, there is a change in temperature. Figure 4.29(b) shows a 1D plot of temperature along a track, further showing the artifact. This effect is caused by the KMPR being partially transparent in IR. The region outside the chamber (85 or 60 µm for NU750 and U1550) is of greater KMPR thickness than inside the chamber (65 or 40 µm for NU750 and U1550). Since each KMPR layer contributes to the total emission, the thicker region of KMPR around the chamber shows higher radiated power than in the chamber itself, where the total KMPR thickness is lower. The camera then detects the increased emission intensity outside the chamber as a higher temperature, yielding the hot annulus artifact.

Moreover, the instrument was not calibrated properly. Note figures 4.28(a) and 4.28(b) - in these two thermographs, the heaters were in thermal equilibrium at 23 °C (room temperature), and yet they show temperature gradients of up to 13.5 °C including temperatures below ambient. It is possible that this spurious result is due to a reflection of the cooled IR camera sensor back onto itself. It is interesting to note that even at room temperature, the unpowered heaters show the hotter annulus optical artifact.

With these artifacts in mind, 1D plots of temperature along the lines shown in figure 4.28(c) yield useful results, including the uncalibrated temperature, shown in figure 4.29. It is clear that the temperature is uniform, even with the ripple, in the region of the chamber. Even considering all of the issues discussed above, the thermographs still demonstrate consistency with simulation results.

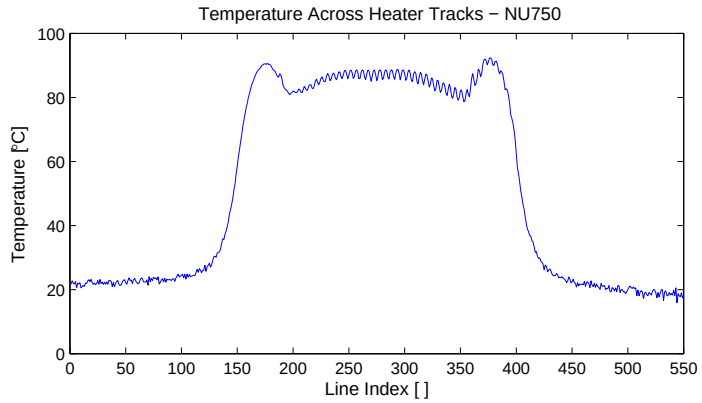

(a)

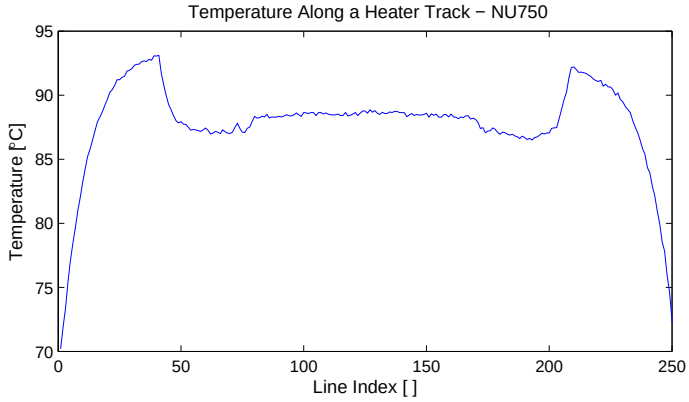

(b)

Figure 4.29: 1D plots of temperature versus arbitrary line index units on the non-uniform power density heater NU750. (a) Across NU750 heater tracks. Notice the ripple in temperature, as well as the general gradient towards a lower temperature on the right-hand side. (b) Along a track in NU750. Note the sharp change in temperature along a heater track which does not change its dimensions at that location, illustrating the optical artifact issue discussed above.

4.6 Methodology Flexibility: CMOS-Scale Heater

In a final demonstration of the flexibility of this design process, the methodology was applied to a very complex geometry. For integration of TDSI-processed microfluidics with the existing CMOS components of the LOC series of chips, it was found that an air pocket beneath the heater may be necessary.

An air pocket in the KMPR (roughly the same size as the PCR chamber and directly beneath it) may sag when the system is brought up to denaturation temperatures, since the glass transition temperature of KMPR is relatively low [93]. To support the floor of the chamber, "posts" can be designed into the system to prevent sagging. The air chamber and posts are collectively referred to as the "air-bridge". Unfortunately, these posts offer a direct route for heat flux to travel rapidly downwards to escape through the highly thermally-conductive silicon wafer. Thus, extra power must be delivered in locations of the chamber affected by this loss.

The architecture of this design is made up of the same layers presented in figure 3.6, with the addition of a metal-on-KMPR layer between KMPR1 and KMPR2. From bottom to top, the air pocket and posts would be patterned in KMPR1 (2 µm), the heater would be patterned on the bottom side of KMPR2 in 100 nm thick aluminum, the PCR chamber floor would be made up of KMPR2 (10 µm), the chamber volume would be constructed in KMPR3 (20 µm), and the PCR ceiling would be made up of KMPR4 (10 µm).

Work done by Matt Reynolds [92] determined the minimum pitch between heater posts that is required to prevent collapse of the membrane beyond 0.5 µm. To accommodate TDSI KMPR processing techniques, it was necessary to make the pitch between posts fixed in the x direction such that all the posts appear between the heater tracks. This was accomplished by making the post pitch and track pitch values multiples and then offsetting the posts to appear between track locations. Hexagonally shaped posts are placed with a pitch of 123 µm in the x and y directions with an offset of 61.5 µm in the y direction between adjacent columns of posts.

The TDSI process responsible for manufacturing the air-bridge and posts is subject to variation which can cause the posts to range ± 2 µm (centered on ~ 14 µm) in radius. The effect of this variation on the temperature uniformity of the chamber will be explored.

By repeating the steps outlined in section 4.3 with a geometry that describes the post locations, a new heater was designed for the KMPR-on-CMOS version of our PCR system. At the time of

writing, this is a work in progress that will be continued by David Sloan.

4.6.1 Step 1 - Power Density Profile Extraction

Performed in exactly the same way as described in sections 4.3.1 and 4.4.1. It was determined that an ideal heater radius of 600 µm is necessary to achieve $\pm 0.5\,^{\circ}\mathrm{C}$ uniformity in the chamber with the air-bridge/posts underneath. Simulation of an ideal heater this size provided the power density profiles that are extracted as arrays above and below the heater plane. As before, these arrays were plotted with 1 µm resolution in the *xy* plane.

4.6.2 Step 2 - Power Density Profile Discretization

It was mentioned that this heater layout generation methodology is a topic of active research. The most recent incarnation of the process has been implemented by David Sloan as a graphical user interface (GUI), written in C#. A screen shot of the resultant heater tracks produced in the GUI is shown in figure 4.30. Note the extreme narrowing of tracks in only the post locations. Current density is intense in these locations, which may reduce device lifetime by electromigration issues.

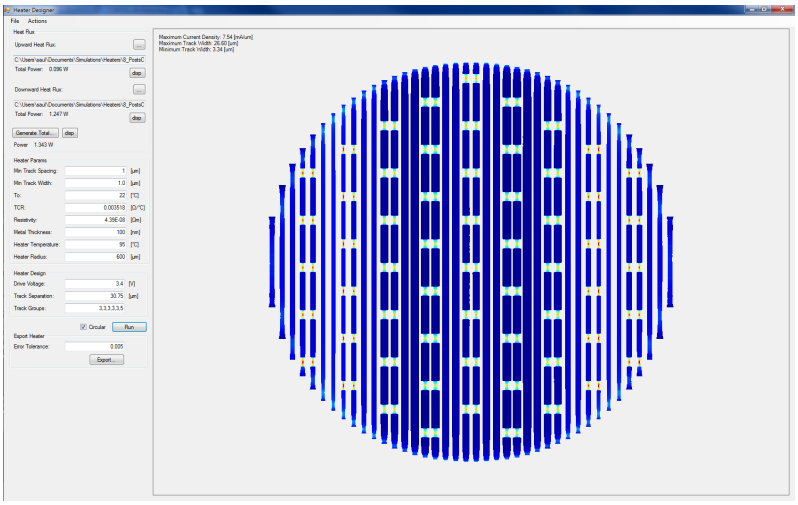

Figure 4.30: This screenshot of the most recent iteration of the heater design methodology as a GUI programmed in C# shows the simulated heater for a CMOS air-bridge design.

4.6.3 Step 3 - Verification

To verify that the generated heater layout achieves good performance, it is placed back into the 3D COMSOL model in place of the idealized planar heater. Figure 4.31 displays a zoomed-in image of the simulated geometry, showing the relation of the air bridge and posts, heater and chamber.

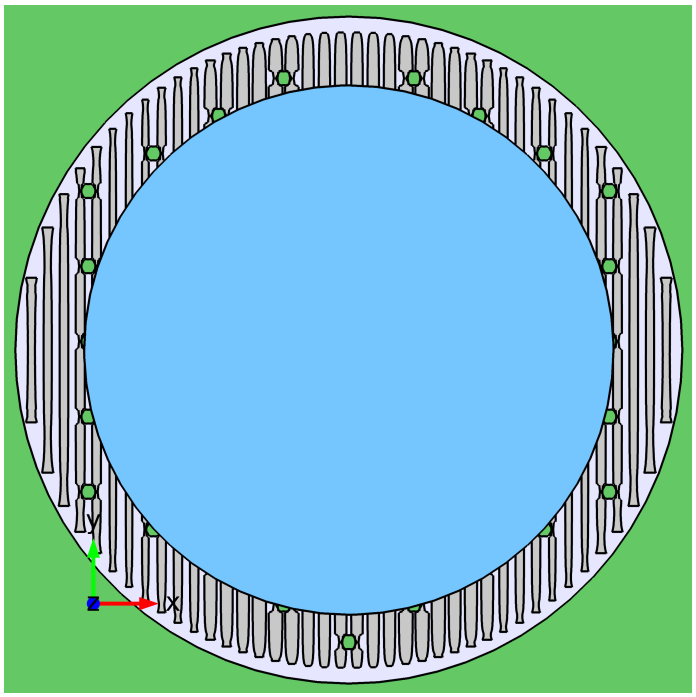

Figure 4.31: A bird's eye view (along the z axis) of the integrated device geometry is shown. KMPR features are shown in green, while heater elements are dark gray and the fluid-filled PCR chamber is shown in light blue. The air bridge itself appears as a lighter Grey around the heater tracks.

As this simulation represents the first attempt at a complicated heater design that includes air-bridge posts, it is only verified with virtual connections between the tracks. With the twenty tracks virtually connected in five groups of three tracks and one group of five tracks (shown as a design choice input in figure 4.30) the model is simulated and uniformity data is plotted.

Finally, this third step in the process was repeated twice with the maximum and minimum possible post sizes. That is, the heater designed for a particular post size was also simulated in two more models, one with the smallest possible posts and one with the largest possible posts.

4.6.4 Simulation Results and Discussion

The results of this complicated geometry imply that there is plenty of opportunity to improve upon the heater design methodology as it currently exists. Figure 4.32(a) shows a 2D colour plot of the temperature on the PCR chamber floor. Note that this plane shows the extremes of temperature variation, which is attenuated in the volume of the reaction chamber. While the target temperature was 95 °C, the plot shows that the chamber floor sees a range from 90.9 °C to 104.6 °C. The histogram of chamber temperature in relative volume, figure 4.32(b), reveals how the chamber temperature is affected when the post radius changes by ±2 µm. Table 4.7 collects all of the uniformity information from the histograms plotted throughout this work. Here we can see clearly what sort of effect on uniformity the introduction of posts below the heater has had. The four original heater designs (no posts) show excellent uniformity: the two smaller heaters were simulated to have 100% of the chamber volume within ±0.5 °C, and the two larger heaters showed 100% of the chamber volume within a ±1 °C range. The CMOS-sized heater with the air-bridge and posts, on the other hand, was simulated to have up to only 82% of the chamber within ±1 °C, in the case where the post size was largest. An additional metric was added to evaluate these designs; the range of temperature for 95% uniformity in the chamber is listed in the third row of table 4.7.

Table 4.7: Temperature uniformity in chamber volume for various heaters, tabulated results.

Heater Design	**NU600** $r_{post} =$ 16 µm	**NU600** $r_{post} =$ 14 µm	**NU600** $r_{post} =$ 12 µm	**NU750**	**U850**	**NU1450**	**U1550**
Percentage of chamber within ±0.5 °C range, (centered on) T_0	51%, 93.2 °C	43%, 97.4 °C	34%, 100.3 °C	100%, 94.3 °C	100%, 94.3 °C	98%, 94.4 °C	94%, 94.2 °C
Percentage of chamber within ±1 °C range, (centered on) T_0	82%, 93.2 °C	73%, 97.1 °C	57%, 100.0 °C	-	-	100%, 94.4 °C	100%, 94.2 °C
±X °C range for 95% chamber volume temperature uniformity, (centered on) T_0	±1.59 °C, 92.8 °C	±1.73 °C, 96.5 °C	±2.40 °C, 99.3 °C	-	-	-	-

The data in table 4.7 makes it clear that the chamber temperature uniformity is significantly worse with a system which makes use of an air-bridge/posts structure underneath the heater. The posts offer a significantly easier path for heat flux to travel than the surrounding air of the air-bridge. As such, the heater tracks passing over and beside post locations must deliver more power to compensate for the loss. This causes a marked decrease in localized track width, increasing current density by a factor of roughly 3.5 and offering points for failure due to electromigration. The increase in track temperature delivered by these "pinches" in the track are shown in figure 4.33(b). Figure 4.33(a) displays the temperatures across the tracks between the posts, in addition to the chamber floor and ceiling. A comparison of these two plots shows how much hotter the tracks get near posts compared to tracks away from posts (up to 170°C near tracks versus 120°C away from tracks). It is evident from figure 4.33(a) that this configuration with the posts is impractical. Such high temperatures can cause problems with polymers exposed to these regions, and can also generate points susceptible to electromigration.

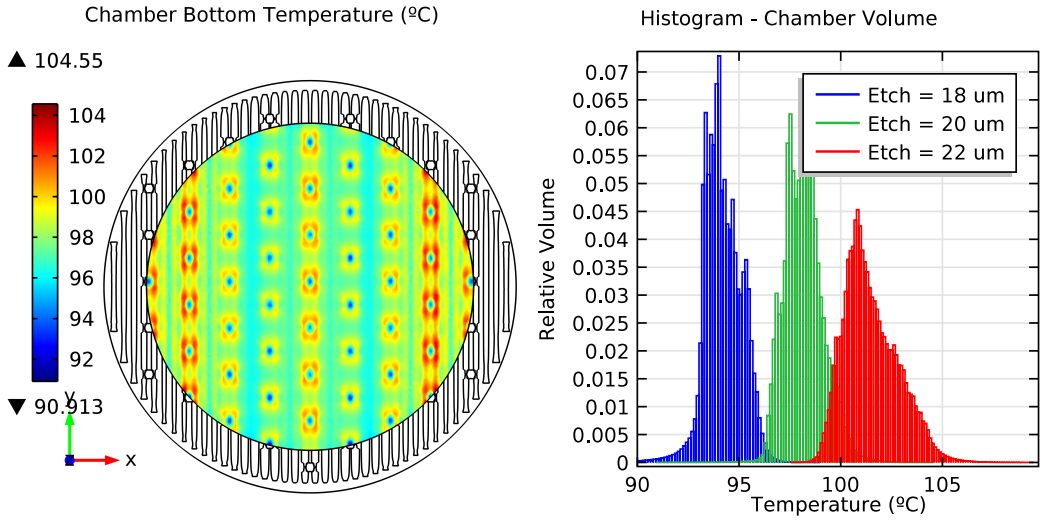

(a) (b)

Figure 4.32: 2D plots of temperature uniformity in NU600 with polymer support posts. (a) Chamber floor temperature plot. (b) Histogram of chamber volume temperature for three etch sizes. Refer to table 4.7 for uniformity values extracted from 100-bin histograms for each of the three post etch sizes.

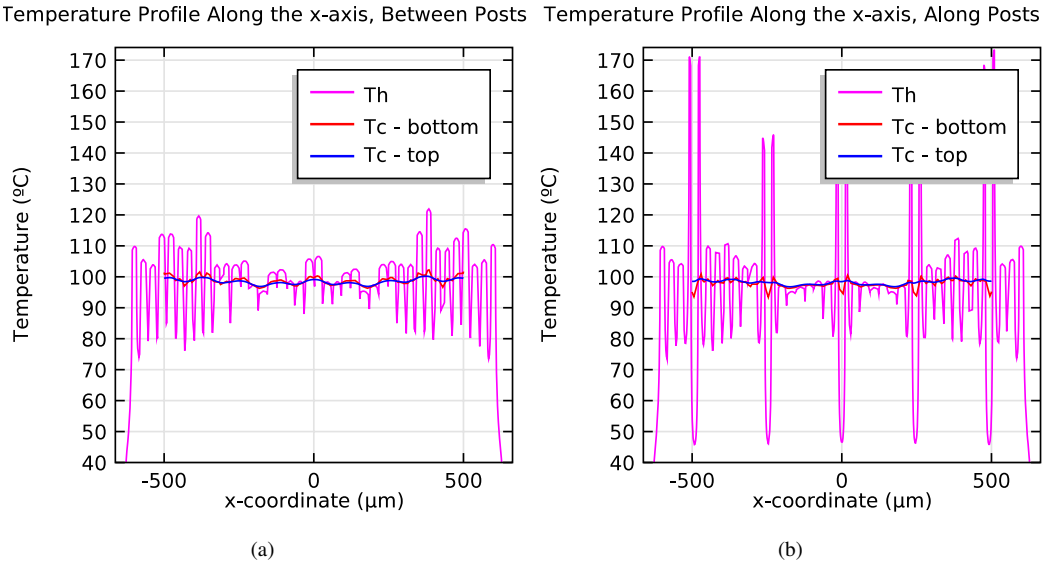

Figure 4.33: 1D plots of temperature uniformity in NU600 with polymer support posts. (a) Temperature profile along the x-axis between posts. (b) Temperature profile along the x-axis along posts. Note the much higher heater temperature T_h to accommodate the higher necessary heat flux at post locations.

Another issue with the air-bridge/posts configuration is the inherent variability in post radius. This is a symptom of the manufacturing process, which is currently part of a non-disclosure agreement. It is important to note that the three post sizes were applied to the exact same heater design, which was designed for the target post size (14µm radius). Interestingly, the uniformity is better in the case where the post size is larger. This suggests that the heater design methodology has much room for improvement, since it appears that too much power is being delivered to the post locations in the target post size case.

Clearly there are many issues with the air-bridge/posts architecture, and alternatives should be explored. One such alternative is to use a thicker KMPR floor layer, effectively replacing the thin, insulating air layer with a thicker, less insulating polymer layer.

To conclude, this NU600 CMOS heater design is a significant step towards a fully-integrated polymer-on-CMOS PCR system. Although the geometry is very complex, the heater design methodology was able to produce a successful design, albeit with much room for improvement. Arbitrary shapes placed in locations that are very disruptive of power delivery for a uniformly heated volume can be mitigated. Moreover, the exercise of doing this design has highlighted issues with

the methodology that can be improved upon in the next iteration

4.7 Conclusions:

Thermal Systems for Integrated Microfluidics-CMOS LOC Technology

LOC thermal system challenges including robustness to changes in ambient environment, accurate thermal control and uniformity, power efficiency, the use of affordable but electromigration-prone metals, and thermal cycling speed, were tackled by making use of finite-element modeling to design the next-generation of LOC thermal systems.

A novel method for designing thin-film heaters was employed to produce an integrated PCR LOC system. This deterministic method controls the power density of the heater, yielding heaters that compensate for uneven heat loss and produce an isothermal environment in the PCR chamber. Moreover, ideal power density distributions can be replicated by the method, allowing for creative or unconventional topologies. Current densities in the traces making up the heating element are controlled, enabling the use of low-cost materials for metallization such as Al in place of the electromigration-resistant, but expensive, Pt.

Robust, accurate thermal control is achieved by combining insulating polymer layers with a highly thermally conductive silicon substrate, making heat sink temperature boundary condition the only external variable of interest. Since the thin-film Al heater is in intimate coupling with the PCR chamber, the thermal resistance between the two components is negligible compared to the resistance from the chamber to the surrounding environment, making it robust to external variables. This configuration mitigates the effect of changing boundary variables and maximizes temperature uniformity in the chamber.

By designing, building and testing two uniform power density profile heaters and two non-uniform power density profiles, we demonstrate the design methodology in a repeatable fashion. The heaters were designed to produce temperatures within 1 °C (± 0.5 °C) at up to 95 °C in the polymer PCR chamber structure. Achieving such a high degree of uniformity makes the method well-suited for designing LOC heater applications, and reduces measurement uncertainty. Since the temperature of the chamber volume is mapped from the resistance of the heater, the measurement uncertainty depends on the TCR of the element. Assuming TCR consistency within 1%, the chamber

temperature is accurate to within $\pm 0.73\,^{\circ}\mathrm{C}$. By virtue of the system's exceptionally short time constant of 64.5 ms, the system can thermal-cycle quickly enough to enable the first ever 3-step PCR of 35 cycles in under two and a half minutes (4.19 s per cycle).

Taken together, these achievements present a LOC thermal system that is inexpensive, accurate and robust - meeting all requirements of a POC medical diagnostic system, and represents a new state of the art for thermal control.

CHAPTER 5

CONCLUSIONS AND FUTURE DIRECTIONS

It was established in the introduction and background of this work that there are still major issues with LOC technology, including the high cost of external instrumentation required for operation of such devices. The option of polymer-on-CMOS as a solution to building the next generation of truly integrated LOC platforms was therefore investigated. More specifically, the FEA tool COMSOL was used in developing the next iterations of the SP and PCR stages of a three-step DNA-based microfluidic diagnostic device.

5.1 Sample Preparation in Integrated Microfluidics-CMOS Technology

Until this work, there had been no on-chip infrastructure to support an integrated sample preparation stage at the device level, which is crucial in a DNA-based LOC diagnostic approach. The goal of this project was to bring this first step of the process up to speed with the other two components (amplification via PCR and detection via CE or MCA) which have seen multiple iterations on the system chip series, ICKAALXX. Finite element modeling techniques were leveraged in designing an on-chip electromagnet applicable to a wide variety of magnetic bead-based SP methods. Conservative design considerations were taken at every step to ensure that the system would have the best chance of success in its first iteration.

Key pieces to a successful on-chip SP module were discussed and issues were resolved, including the the design of a high-force electromagnet for selective trapping and releasing of magnetic beads and an analysis of transient pressures caused by peristaltic pumping. This final concentration step to the SP process is vital for the miniscule volumes associated with on-chip diagnostics, and direct elution to the PCR chamber avoids one point of possible contamination.

An $n = 8$ square spiral electromagnet was implemented in ICKAAL12. It was found by simulation to generate a typical and maximum transverse force (opposing flow) of 1 pN and 4 pN respectively. Although there remain some unknowns in the system (an accurate measure of the magnetic susceptibility of the ChargeSwitch brand of magnetic beads), based on our conservative estimates a safe range for a 1 µL volume sample processing time would be $2-28$ min with no external field applied and $0.5-5.6$ min with a small 50 mT external field applied.

Given that the SP processing time has been reduced roughly to the order of minutes, it was important that the PCR step in the process also adhered to this scale. With a new in-house design methodology for generating heater layouts, a new design was capable of doing rapid temperature cycling of small fluid volumes, this task was achieved as well.

5.2 Thermal Systems for Integrated Microfluidics-CMOS Technology

Many LOC microfluidic systems require some sort of thermal control. In the diagnostic approach of SP-PCR-CE or MCA, the PCR and MCA components require accurate temperature control and uniformity. For CMOS-relevant designs, spatial selectivity of the thermal system is very important for saving space and power. The novel thin-film heater design methodology demonstrated in this work represents a convenient and powerful tool for generating micro-scale heaters. Moreover, it enabled the use of affordable but electromigration-prone metals for the heater fabrication

The in-house KMPR-on-silicon variants of heaters that were used to validate this design methodology are capable of operating a standard 3-step, 35 cycle PCR protocol in under two and a half minutes (4.19 s per cycle). This demonstration is a significant step towards the implementation of a heater in the system chip KMPR architecture. These in-house fabricated designs were supplemented with another design that could be implemented in TDSI's existing KMPR-on-CMOS process. Although it showed several problems, the air-bridge-with-posts design highlighted underlying issues with the heater design methodology that can be corrected in future iterations.

5.3 Future Directions

With regards to future work relating directly to the two subjects of interest in this thesis, there is plenty to do. The SP module designed in this work is the first of its kind in our system chip. This design and future iterations will refine it to minimize process time and power. The heater design methodology to create the in-house KMPR-on-silicon heater prototypes has room for improvement, as brought to light by the CMOS air-bridge/posts architecture. Further iterations of the CMOS heater itself are required before a final selection is made for a design to be implemented in the next KMPR-on-CMOS fabrication run by TDSI. In addition to these topics, there are may more issues that justify further research.

5.3.1 Chip-to-World SP Scaling

The main point of the CMOS SP module discussed in this work is to integrate a method for tertiary sample preparation - that is, to take an already reduced-volume sample approximately 1 µL in volume and process it on-chip to avoid many of the problems associated with off-chip processing. Further, if the cell lysis and DNA purification steps are implemented on chip by making use of additional reagent wells and valves, then the system as-designed could be capable of processing even a raw sample 1 µL in volume.

Despite this step towards a well-integrated cost-effective solution, reducing a large sample volume to a small one is not a trivial matter. Going forward, much work is left to be done in prototyping a first-step for the SP module in which large volumes (such as in water quality) are reduced in a way that integrates with the system chip platform. Fortunately, magnetic bead-based applications lend themselves well to processes that require volume reductions.

One option for maintaining selectivity even at the macro scale is to use a PCB device similar to the rapid-prototyped model presented in section 3.8.2. To improve this module, a highly susceptible magnetic yoke could be used to concentrate the field in strategically-placed locations. One such ultra-highly magnetically permeable material is known as Metglas® (Fe85B5Si10), which can be deposited as an amorphous thin film allowing for creative designs.

Another alternative at the macro scale is to use strong permanent magnets. Mechanical movement could be introduced to allow for selective trapping and releasing of magnetic beads. This method, however, introduces complications due to the necessity of moving parts. Moreover, spatial

selectivity with permanent magnets is not as good as with electromagnets, making fine volume reductions more difficult.

5.3.2 Alternative Sample-Preparation Methods

Despite the elegance of having a single CMOS-based system chip that integrates all the instrumentation necessary for doing a LOC DNA-based diagnostic, there remain other good, possibly superior options for various parts of the process. The SP module, for example, could benefit from the simplified approach of mechanical trapping of the beads. Alternatively, the charge-switching coating that makes the CS beads useful for SP could be integrated into a chip-world scaling device, removing the need for beads or an electromagnet altogether. If beads and electromagnets prove to offer the most opportunities for various SP approaches, fields and gradients could be increased substantially again by incorporating a highly susceptible material to concentrate local fields. As mentioned above, Metglas® [94] is one such material that can be used in this way.

5.3.3 Controller-Optimization for Thermal Systems

Although the thermal system discussed in this work displays an incredibly fast response, even further reductions in the slew rate would be possible when the system is implemented with an optimized controller. The PCR speeds possible with the implementation of a controller were presented, though the controller itself has not yet been designed and implemented.

5.3.4 Modeling and Prototyping

5.3.4.1 Alternatives for Simulation-Prototyping Research

The time and cost savings achieved by leveraging FEM techniques via COMSOL Multiphysics were very beneficial in this work. However, the planar structures and high meshing resolution necessary for successful simulations meant that the modeling process itself was fairly time-consuming - some 3D electromagnetic simulations and 3D thermal transient simulations took several hours to complete. Other design and experimentation methods could be explored to improve deliverables and reduce prototyping time even further.

Analytical tools and software could be implemented to do initial designs. This would enable researchers to design and fabricate in-house proof-of-concept prototypes that help to elucidate

problems earlier. Experimental results also assist in driving work to literature by serving to validate the associated theoretical work.

In future, it is recommended that researchers consider two phases for this kind of work: in a first phase, analytical calculations could be performed, followed by rapid prototyping and experimental research. After finalizing on these efforts by submitting the work to peer-reviewed journals, a second phase of doing detailed design and FEM simulations of the final device can be performed. This second phase would be concluded by attempting to publish final work as a follow up to the initial findings.

5.3.4.2 Prototype Lifetime

As discussed briefly in section 4.5.4, the costs of in-house prototyping are substantial. Roughly one week of a researcher's time spent in a fabrication facility plus the equipment time and materials cost adds up to much more than the dollar-per-test regime that is necessary for disposable units. Furthermore, for debugging purposes, the fabricated devices would ideally be reliable in repeating experiments, and at the very least, do not fail after only one test. For these additional reasons it is very important to design robust systems and use affordable fabrication techniques and materials.

5.4 Final Remarks

Malaria was introduced at the beginning of this thesis as one prime application for the LOC developments presented here; to illustrate one scenario in which this work as a whole could be applied, we conclude with a final look at how Malaria is diagnosed today.

Visual identification of the malaria parasite in blood smear samples under microscope is the gold standard in malaria diagnosis [95]. This technique, however, directly depends the quality of the equipment, reagents, and laboratorian. Inexperienced personnel, poor staining of the parasite, or imaging of poor quality may contribute to false-negative diagnoses. Moreover, medical personnel performing visual identification of the parasite cannot distinguish between malaria species, but PCR can; malaria treatment plans vary significantly because of species-specific drug resistance. Indeed, the Centers for Disease Control and Prevention (CDC) of the United States Department of Health & Human Services recommends that drug resistance be evaluated in every malaria case in the U.S [95]. Unfortunately, PCR continues to be "...of limited utility for the diagnosis of acutely ill patients in

the standard healthcare setting [since] PCR results are [not] available quickly enough to be of value in [diagnosis] of malaria infection." [95]

Similar to the designs found in this thesis, a bead-based "blood kit" capable of isolating genomic DNA out of whole blood could be used in this diagnostic process. Integrated as part of a medical device, the electromagnets and fluidic designs would be constructed to ensure that they are capable of manipulating the beads as required by the protocol (e.g., holding them against a fluid flow, trapping and releasing for mixing, etc.). That bead-based SP module could be integrated with an under-2.5 min PCR step, and finally a detection mechanism, yielding a total system capable of going from sample to answer in a matter of minutes, effectively replacing the gold standard for Malaria identification both in the US and abroad in remote settings where point-of-care testing is vital to the successful treatment of infected patients.

Many regions of the world are not sufficiently economically developed to afford state of the art medical infrastructure. Afflictions such as malaria are curable, but require diagnosis for effective treatment. Portable point-of-care diagnostics implemented in fully integrated, robust lab-on-chip platforms represent one way to address the lack of accessibility to expensive diagnostic equipment. Considerable reductions in price-per-test achieved through economies of scale will be achieved as lab-on-chip technology moves forward with developments in polymer-on-CMOS architectures.

BIBLIOGRAPHY

[1] E. K. Wheeler, C. A. Hara, J. Frank, J. Deotte, S. B. Hall, W. Benett, C. Spadaccini, and N. R. Beer, "Under-three minute PCR: probing the limits of fast amplification," *The Analyst*, 2011. [Online]. Available: http://xlink.rsc.org/?DOI=c1an15365j

[2] "WHO | malaria." [Online]. Available: http://www.who.int/mediacentre/factsheets/fs094/en/index.html

[3] "WHO | World Malaria Report 2014." [Online]. Available: http://www.who.int/malaria/publications/world_malaria_report_2014/en/

[4] G. Kaigala, M. Behnam, C. Bliss, M. Khorasani, S. Ho, J. McMullin, D. Elliott, and C. Backhouse, "Inexpensive, universal serial bus-powered and fully portable lab-on-a-chip-based capillary electrophoresis instrument," *IET Nanobiotechnology*, vol. 3, no. 1, p. 1, 2009. [Online]. Available: http://link.aip.org/link/INEACX/v3/i1/p1/s1&Agg=doi

[5] Y. Zhang and P. Ozdemir, "Microfluidic DNA amplification–a review," *Analytica Chimica Acta*, vol. 638, no. 2, pp. 115–125, Apr. 2009. [Online]. Available: http://www.sciencedirect.com.login.ezproxy.library.ualberta.ca/science/article/B6TF4-4VRX68N-2/2/8a7732832ed2314f98c8eb9fc74de9c0

[6] G. V. Kaigala, M. Behnam, A. C. E. Bidulock, C. Bargen, R. W. Johnstone, D. G. Elliott, and C. J. Backhouse, "A scalable and modular lab-on-a-chip genetic analysis instrument," *The Analyst*, vol. 135, no. 7, p. 1606, 2010. [Online]. Available: http://xlink.rsc.org/?DOI=b925111a

[7] A. T. Ciftlik and M. A. M. Gijs, "A low-temperature parylene-to-silicon dioxide bonding technique for high-pressure microfluidics," *Journal of Micromechanics and Microengineering*, vol. 21, p. 035011, 2011.

[8] N. Thaitrong, P. Liu, T. Briese, W. I. Lipkin, T. N. Chiesl, Y. Higa, and R. A. Mathies, "Integrated capillary electrophoresis microsystem for multiplex analysis of human respiratory viruses," *Analytical Chemistry*, vol. 82, no. 24, pp. 10 102–10 109, Dec. 2010. [Online]. Available: http://pubs.acs.org/doi/abs/10.1021/ac1020744

[9] P. Liu, X. Li, S. A. Greenspoon, J. R. Scherer, and R. A. Mathies, "Integrated DNA purification, PCR, sample cleanup, and capillary electrophoresis microchip for forensic human identification," *Lab on a Chip*, vol. 11, no. 6, p. 1041, 2011. [Online]. Available: http://xlink.rsc.org/?DOI=c0lc00533a

[10] G. V. Kaigala, V. N. Hoang, A. Stickel, J. Lauzon, D. Manage, L. M. Pilarski, and C. J. Backhouse, "An inexpensive and portable microchip-based platform for integrated RT–PCR and capillary electrophoresis," *The Analyst*, vol. 133, no. 3, p. 331, 2008. [Online]. Available: http://xlink.rsc.org/?DOI=b714308g

[11] V. F. Cardoso, S. O. Catarino, J. S. Nunes, L. Rebouta, J. G. Rocha, S. Lanceros-Mendez, and G. Minas, "Lab-on-a-chip with b-poly(vinylidene fluoride) based acoustic microagitation," *IEEE Transactions on Biomedical Engineering*, vol. 57, no. 5, pp. 1184–1190, May 2010. [Online]. Available: http://ieeexplore.ieee.org/lpdocs/epic03/wrapper.htm?arnumber=5306140

[12] L. Yu, C. M. Li, Y. Liu, J. Gao, W. Wang, and Y. Gan, "Flow-through functionalized PDMS microfluidic channels with dextran derivative for ELISAs," *Lab on a Chip*, vol. 9, no. 9, p. 1243, 2009. [Online]. Available: http://xlink.rsc.org/?DOI=b816018j

[13] S. Talaei, O. Frey, P. D. Van Der Wal, N. F. De Rooij, and M. Koudelka-Hep, "Hybrid microfluidic cartridge formed by irreversible bonding of SU-8 and PDMS for multi-layer flow applications," *Procedia Chemistry*, vol. 1, no. 1, pp. 381–384, 2009.

[14] T. B. Christensen, D. D. Bang, and A. Wolff, "Multiplex polymerase chain reaction (PCR) on a SU-8 chip," *Microelectronic Engineering*, vol. 85, no. 5-6, pp. 1278–1281, 2008.

[15] Y. S. Shin, K. Cho, S. H. Lim, S. Chung, S. J. Park, C. Chung, D. C. Han, and J. K. Chang, "PDMS-based micro PCR chip with parylene coating," *Journal of Micromechanics and Microengineering*, vol. 13, p. 768, 2003.

[16] Q. He, E. Meng, Y. C. Tai, C. M. Rutherglen, J. Erickson, and J. Pine, "Parylene neurocages for live neural networks study," in *TRANSDUCERS, Solid-State Sensors, Actuators and Microsystems, 12th International Conference on, 2003*, vol. 2, 2003, pp. 995–998.

[17] J. Lee, K. Hwang, K. Yoon, T. Kim, S. Ahn, J. Lee, K. Hwang, K. Yoon, T. Kim, and S. Ahn, "Microstructure and adhesion of au deposited on parylene-c substrate with surface modification for potential immunoassay application," *IEEE Transactions on Plasma Science*, vol. 32, no. 2, pp. 505–509, Apr. 2004. [Online]. Available: http://ieeexplore.ieee.org/lpdocs/epic03/wrapper.htm?arnumber=1308499

[18] E. Meng and Y. C. Tai, "Parylene etching techniques for microfluidics and bioMEMS," in *Micro Electro Mechanical Systems, 2005. MEMS 2005. 18th IEEE International Conference on*, 2005, pp. 568–571.

[19] Z. Hua, Y. Xia, O. Srivannavit, J.-M. Rouillard, X. Zhou, X. Gao, and E. Gulari, "A versatile microreactor platform featuring a chemical-resistant microvalve array for addressable multiplex syntheses and assays," *Journal of Micromechanics and Microengineering*, vol. 16, no. 8, pp. 1433–1443, Aug. 2006. [Online]. Available: http://stacks.iop.org/0960-1317/16/i=8/a=001?key=crossref.52fd85b4d877b493521211f3e1af417f

[20] C. L. Chen, S. Selvarasah, S. H. Chao, A. Khanicheh, C. Mavroidis, and M. R. Dokmeci, "An electrohydrodynamic micropump for on-chip fluid pumping on a flexible parylene substrate," in *Nano/Micro Engineered and Molecular Systems, 2007. NEMS'07. 2nd IEEE International Conference on*, 2007, pp. 826–829.

[21] R. S. Gaster, D. A. Hall, and S. X. Wang, "nanoLAB: an ultraportable, handheld diagnostic laboratory for global health," *Lab on a Chip*, 2011. [Online]. Available: http://xlink.rsc.org/?DOI=c0lc00534g

[22] N. Beyor, L. Yi, T. S. Seo, and R. A. Mathies, "Integrated capture, concentration, polymerase chain reaction, and capillary electrophoretic analysis of pathogens on a chip," *Analytical Chemistry*, vol. 81, no. 9, pp. 3523–3528, May 2009. [Online]. Available: http://pubs.acs.org/doi/abs/10.1021/ac900060r

[23] I. K. Dimov, L. Basabe-Desmonts, J. L. Garcia-Cordero, B. M. Ross, A. J. Ricco, and L. P. Lee, "Stand-alone self-powered integrated microfluidic blood analysis system (SIMBAS)," *Lab on a Chip*, 2011. [Online]. Available: http://xlink.rsc.org/?DOI=c0lc00403k

[24] J. Do and C. H. Ahn, "A polymer lab-on-a-chip for magnetic immunoassay with on-chip sampling and detection capabilities," *Lab on a Chip*, vol. 8, no. 4, p. 542, 2008. [Online]. Available: http://pubs.rsc.org.login.ezproxy.library.ualberta.ca/en/Content/ArticleLanding/2008/LC/b715569g

[25] J. Parton, C. Birch, C. Kemp, S. J. Haswell, N. Pamme, and K. J. Shaw, "Integrated DNA extraction and amplification using electrokinetic pumping in a microfluidic device," *Analytical Methods*, vol. 4, no. 1, p. 96, 2012. [Online]. Available: http://xlink.rsc.org/?DOI=c1ay05552f

[26] "KMPR 1000 photoresist - MicroChem." [Online]. Available: http://microchem.com/Prod-KMPR.htm

[27] M. Behnam, G. V. Kaigala, M. Khorasani, P. Marshall, C. J. Backhouse, and D. G. Elliott, "An integrated CMOS high voltage supply for lab-on-a-chip systems," *Lab on a Chip*, vol. 8, no. 9, p. 1524, 2008. [Online]. Available: http://xlink.rsc.org/?DOI=b804275f

[28] T. Notomi, H. Okayama, H. Masubuchi, T. Yonekawa, K. Watanabe, N. Amino, and T. Hase, "Loop-mediated isothermal amplification of DNA," *Nucleic Acids Research*, vol. 28, no. 12, p. e63, Jun. 2000, PMID: 10871386 PMCID: PMC102748. [Online]. Available: http://www.ncbi.nlm.nih.gov/pmc/articles/PMC102748/

[29] J. Compton, "Nucleic acid sequence-based amplification," *Nature*, vol. 350, no. 6313, pp. 91–92, 1991.

[30] R. K. Saiki, D. H. Gelfand, S. Stoffel, S. J. Scharf, R. Higuchi, G. T. Horn, K. B. Mullis, and H. A. Erlich, "Primer-directed enzymatic amplification of DNA with a thermostable DNA polymerase," *Science*, vol. 239, no. 4839, pp. 487–491, Jan. 1988, PMID: 2448875. [Online]. Available: http://www.sciencemag.org.login.ezproxy.library.ualberta.ca/content/239/4839/487

[31] C. J. Easley, J. M. Karlinsey, J. M. Bienvenue, L. A. Legendre, M. G. Roper, S. H. Feldman, M. A. Hughes, E. L. Hewlett, T. J. Merkel, J. P. Ferrance, and J. P. Landers, "A fully integrated microfluidic genetic analysis system with sample-in–answer-out capability," *Proceedings of*

the National Academy of Sciences, vol. 103, no. 51, pp. 19 272 –19 277, Dec. 2006. [Online]. Available: http://www.pnas.org/content/103/51/19272.abstract

[32] Z. Hua, J. L. Rouse, A. E. Eckhardt, V. Srinivasan, V. K. Pamula, W. A. Schell, J. L. Benton, T. G. Mitchell, and M. G. Pollack, "Multiplexed real-time polymerase chain reaction on a digital microfluidic platform," *Anal. Chem*, vol. 82, no. 6, pp. 2310–2316, 2010.

[33] D. Liu, Z. Ou, M. Xu, and L. Wang, "Simplified transient isotachophoresis/capillary gel electrophoresis method for highly sensitive analysis of polymerase chain reaction samples on a microchip with laser-induced fluorescence detection," *Journal of Chromatography A*, vol. 1214, no. 1-2, pp. 165–170, 2008.

[34] P. Liu, T. S. Seo, N. Beyor, K.-J. Shin, J. R. Scherer, and R. A. Mathies, "Integrated portable polymerase chain reaction-capillary electrophoresis microsystem for rapid forensic short tandem repeat typing," *Analytical Chemistry*, vol. 79, no. 5, pp. 1881–1889, Mar. 2007. [Online]. Available: http://dx.doi.org.login.ezproxy.library.ualberta.ca/10.1021/ac061961k

[35] M. E. Johnson and J. P. Landers, "Fundamentals and practice for ultrasensitive laser-induced fluorescence detection in microanalytical systems," *Electrophoresis*, vol. 25, no. 21-22, pp. 3513–3527, Nov. 2004, PMID: 15565706. [Online]. Available: http://www.ncbi.nlm.nih.gov/pubmed/15565706

[36] A. Chandrasekaran and M. Packirisamy, "Integrated microfluidic biophotonic chip for laser induced fluorescence detection," *Biomedical Microdevices*, vol. 12, no. 5, pp. 923–933, Jun. 2010. [Online]. Available: http://www.springerlink.com/index/10.1007/s10544-010-9447-9

[37] E. P. Dupont, E. Labonne, C. Vandevyver, U. Lehmann, E. Charbon, and M. A. M. Gijs, "Monolithic silicon chip for immunofluorescence detection on single magnetic beads," *Analytical Chemistry*, vol. 82, no. 1, pp. 49–52, Jan. 2010. [Online]. Available: http://pubs.acs.org/doi/abs/10.1021/ac902241j

[38] P. Chomczynski and N. Sacchi, "Single-step method of RNA isolation by acid guanidinium thiocyanate-phenol-chloroform extraction," *Analytical Biochemistry*, vol. 162, no. 1, pp. 156–159, Apr. 1987. [Online]. Available: http://www.sciencedirect.com/science/article/pii/0003269787900212

[39] "Dynabeads products & technology for magnetic bead separation | life technologies." [Online]. Available: http://www.invitrogen.com/site/us/en/home/brands/Product-Brand/Dynal/dynabeads_technology.html?s_kwcid=AL!3652!3!27523444506!e!!g!!dynabeads&ef_id=UOXBxQAAEFec5LK8:20130805152140:s

[40] O. Florescu, K. Wang, P. Au, J. Tang, E. Harris, P. R. Beatty, and B. E. Boser, "On-chip magnetic separation of superparamagnetic beads for integrated molecular analysis," *Journal of Applied Physics*, vol. 107, no. 5, p. 054702, 2010. [Online]. Available: http://link.aip.org/link/JAPIAU/v107/i5/p054702/s1&Agg=doi

[41] C. Fuh and S. Chen, "Magnetic split-flow thin fractionation of magnetically susceptible particles," *Journal of Chromatography A*, vol. 857, no. 1–2, pp. 193–204, Oct. 1999. [Online]. Available: http://www.sciencedirect.com/science/article/pii/S002196739900775X

[42] Q. Ramadan and M. A. M. Gijs, "Simultaneous sample washing and concentration using a "trapping-and-releasing" mechanism of magnetic beads on a microfluidic chip," *The Analyst*, vol. 136, no. 6, p. 1157, 2011. [Online]. Available: http://xlink.rsc.org/?DOI=c0an00654h

[43] R. Fulcrand, A. Bancaud, C. Escriba, Q. He, S. Charlot, A. Boukabache, and A.-M. Gue, "On chip magnetic actuator for batch-mode dynamic manipulation of magnetic particles in compact lab-on-chip," *Sensors and Actuators B: Chemical*, vol. 160, no. 1, pp. 1520–1528, Dec. 2011. [Online]. Available: http://www.sciencedirect.com/science/article/pii/S0925400511007349

[44] R. Afshar, Y. Moser, T. Lehnert, and M. Gijs, "Magneto-microfluidic three-dimensional focusing of magnetic particles," in *American Institute of Physics Conference Series*, vol. 1311, 2010, pp. 161–166.

[45] Invitrogen, "Dynabeads Oligo (dT)25 Manual," 2008. [Online]. Available: https://www.lifetechnologies.com/order/catalog/product/61005

[46] H. Tsai, Y. Fang, and C. Fuh, "BioMagnetic research and technology," *BioMagnetic Research and Technology*, vol. 4, p. 6, 2006.

[47] H. Lee, Y. Liu, R. Westervelt, and D. Ham, "IC/Microfluidic hybrid system for magnetic manipulation of biological cells," *IEEE Journal of Solid-State Circuits*, vol. 41, no. 6, pp. 1471–1480, Jun. 2006. [Online]. Available: http://ieeexplore.ieee.org/lpdocs/epic03/wrapper.htm?arnumber=1637611

[48] "ChargeSwitch nucleic acid purification technology | life technologies." [Online]. Available: http://www.invitrogen.com/site/us/en/home/brands/Product-Brand/ChargeSwitch.html

[49] J. W. Choi, C. H. Ahn, S. Bhansali, and H. T. Henderson, "A new magnetic bead-based, filterless bio-separator with planar electromagnet surfaces for integrated bio-detection systems," *Sensors and Actuators B: Chemical*, vol. 68, no. 1-3, pp. 34–39, 2000.

[50] J.-W. Choi, T. M. Liakopoulos, and C. H. Ahn, "An on-chip magnetic bead separator using spiral electromagnets with semi-encapsulated permalloy," *Biosensors and Bioelectronics*, vol. 16, no. 6, pp. 409–416, Aug. 2001. [Online]. Available: http://www.sciencedirect.com/science/article/pii/S0956566301001543

[51] M. Tondra, M. Granger, R. Fuerst, M. Porter, C. Nordman, J. Taylor, and S. Akou, "Design of integrated microfluidic device for sorting magnetic beads in biological assays," *Magnetics, IEEE Transactions on*, vol. 37, no. 4, pp. 2621–2623, 2001.

[52] Q. Ramadan, V. Samper, D. Poenar, and C. Yu, "On-chip micro-electromagnets for magnetic-based bio-molecules separation," *Journal of Magnetism and Magnetic Materials*, vol. 281, no. 2-3, pp. 150–172, Oct. 2004. [Online]. Available: http://www.sciencedirect.com/science/article/pii/S0304885304005219

[53] K. Smistrup, O. Hansen, H. Bruus, and M. F. Hansen, "Magnetic separation in microfluidic systems using microfabricated electromagnets–experiments and simulations," *Journal of Magnetism and Magnetic Materials*, vol. 293, no. 1, pp. 597–604, May 2005. [Online]. Available: http://www.sciencedirect.com/science/article/pii/S0304885305001411

[54] K. Smistrup, P. Tang, O. Hansen, and M. Hansen, "Microelectromagnet for magnetic manipulation in lab-on-a-chip systems," *Journal of magnetism and magnetic materials*, vol. 300, no. 2, pp. 418–426, 2006.

[55] K. Smistrup, M. Bu, A. Wolff, H. Bruus, and M. F. Hansen, "Theoretical analysis of a new, efficient microfluidic magnetic bead separator based on magnetic structures on multiple length scales," *Microfluidics and Nanofluidics*, vol. 4, no. 6, pp. 565–573, Aug. 2007. [Online]. Available: http://www.springerlink.com/index/10.1007/s10404-007-0213-0

[56] Y. Moser, T. Lehnert, and M. A. M. Gijs, "On-chip immuno-agglutination assay with analyte capture by dynamic manipulation of superparamagnetic beads," *Lab on a Chip*, vol. 9, no. 22, p. 3261, 2009. [Online]. Available: http://xlink.rsc.org/?DOI=b907724c

[57] L. Neel, *Selected works of Louis Neel: translation from the French authorized by the Centre national de la recherche scientifique*. New York: Gordon and Breach, 1988.

[58] N. Pamme, "Magnetism and microfluidics," *Lab on a Chip*, vol. 6, no. 1, p. 24, 2006. [Online]. Available: http://xlink.rsc.org/?DOI=b513005k

[59] E. W. Weisstein, "Convective Operator." [Online]. Available: http://mathworld.wolfram.com/ConvectiveOperator.html

[60] H. Tromborg, E. Aksnes, A. Molteberg, N. Kjus, I. Manger, M. v. Wanrooij, and M. Martens, "New optimised one micron magnetic bead platform for fast and efficient development of automated immunoassays." [Online]. Available: http://tools.lifetechnologies.com/content/sfs/brochures/660_Automated_immunoassays.pdf

[61] P. Minqiang, T. Yong, Z. Wei, and L. Longsheng, "Flow distribution among microchannels with asymmetrical manifolds," in *Control and Automation, 2007. ICCA 2007. IEEE International Conference on*, Jun. 2007, pp. 193 –197.

[62] C. Fuh, M. Lai, L. Lin, and S. Yeh, "A method for determination of particle magnetic susceptibility with analytical magnetapheresis," *Analytical chemistry*, vol. 72, no. 15, pp. 3590–3595, 2000.

[63] C. Fuh, J. Lai, and C. Chang, "Particle magnetic susceptibility determination using analytical split-flow thin fractionation," *Journal of Chromatography A*, vol. 923, no. 1-2, pp. 263–270, 2001.

[64] J. Schenck, "The role of magnetic susceptibility in magnetic resonance imaging: MRI magnetic compatibility of the first and second kinds," *Medical Physics*, vol. 23, no. 6, pp. 815–850, Jun. 1996, WOS:A1996UT13100001.

[65] D. J. Laser and J. G. Santiago, "A review of micropumps," *Journal of Micromechanics and Microengineering*, vol. 14, no. 6, pp. R35–R64, Jun. 2004. [Online]. Available: http://stacks.iop.org/0960-1317/14/i=6/a=R01?key=crossref.137857bfcf5ea513064ec576b484af8f

[66] A. Wasay and D. Sameoto, "Gecko gaskets for self-sealing and high-strength reversible bonding of microfluidics," *Lab Chip*, vol. 15, no. 13, pp. 2749–2753, 2015. [Online]. Available: http://xlink.rsc.org/?DOI=C5LC00342C

[67] "ChargeSwitch gDNA Normalized Buccal Cell Kit - Life Technologies." [Online]. Available: https://www.lifetechnologies.com/order/catalog/product/CS11020

[68] J. Martinez-Quijada, T. Ma, G. H. Hall, M. Reynolds, D. Sloan, S. Caverhill-Godkewitsch, D. M. Glerum, D. Sameoto, D. G. Elliott, and C. J. Backhouse, "Robust thermal control for CMOS-based lab-on-chip systems," *Journal of Micromechanics and Microengineering*, vol. 25, no. 7, p. 075005, Jul. 2015. [Online]. Available: http://iopscience.iop.org.login.ezproxy.library.ualberta.ca/0960-1317/25/7/075005

[69] J. Noh, S. W. Sung, M. K. Jeon, S. H. Kim, L. P. Lee, and S. I. Woo, "In situ thermal diagnostics of the micro-PCR system using liquid crystals," *Sensors and Actuators A: Physical*, vol. 122, no. 2, pp. 196–202, Aug. 2005. [Online]. Available: http://www.sciencedirect.com/science/article/pii/S092442470500275X

[70] P.-C. Chen, D. E. Nikitopoulos, S. A. Soper, and M. C. Murphy, "Temperature distribution effects on micro-CFPCR performance," *Biomedical Microdevices*, vol. 10, no. 2, pp. 141–152, Apr. 2008. [Online]. Available: http://link.springer.com.login.ezproxy.library.ualberta.ca/article/10.1007/s10544-007-9119-6

[71] C. D. Bennett, M. N. Campbell, C. J. Cook, D. J. Eyre, L. M. Nay, D. R. Nielsen, R. P. Rasmussen, and P. S. Bernard, "The LightTyper: high-throughput genotyping using fluorescent melting curve analysis," *Biotechniques*, vol. 34, no. 6, pp. 1288–1295, 2003. [Online]. Available: http://www.biotechniques.com/multimedia/archive/00011/03346pf01_11290a.pdf

[72] K. Hu, Z. Chen, and J. Huang, "Research on temperature measuring positions selection and verification for polymerase chain reaction instruments," in *2011 4th International Conference on Biomedical Engineering and Informatics (BMEI)*, vol. 3, Oct. 2011, pp. 1165 –1169.

[73] H. Nagai, Y. Murakami, K. Yokoyama, and E. Tamiya, "High-throughput PCR in silicon based microchamber array," *Biosensors and Bioelectronics*, vol. 16, no. 9–12, pp. 1015–1019, Dec. 2001. [Online]. Available: http://www.sciencedirect.com/science/article/pii/S0956566301002482

[74] M. G. Roper, C. J. Easley, L. A. Legendre, J. A. C. Humphrey, and J. P. Landers, "Infrared temperature control system for a completely noncontact polymerase chain reaction in microfluidic chips," *Analytical Chemistry*, vol. 79, no. 4, pp. 1294–1300, Feb. 2007. [Online]. Available: http://dx.doi.org/10.1021/ac0613277

[75] C. Zhang and D. Xing, "Miniaturized PCR chips for nucleic acid amplification and analysis: latest advances and future trends," *Nucleic acids research*, 2007.

[76] H. Kim, S. Dixit, C. J. Green, and G. W. Faris, "Nanodroplet real-time PCR system with laser assisted heating," *Opt. Express*, vol. 17, pp. 218–227, 2009.

[77] N. Pak, D. C. Saunders, C. R. Phaneuf, and C. R. Forest, "Plug-and-play, infrared, laser-mediated PCR in a microfluidic chip," *Biomedical Microdevices*, vol. 14, no. 2, pp. 427–433, Apr. 2012. [Online]. Available: http://link.springer.com.login.ezproxy.library.ualberta.ca/article/10.1007/s10544-011-9619-2

[78] Q. Zhang, W. Wang, H. Zhang, and Y. Wang, "Temperature analysis of continuous-flow micro-PCR based on FEA," *Sensors and Actuators B: Chemical*, vol. 82, no. 1, pp. 75–81, Feb. 2002. [Online]. Available: http://www.sciencedirect.com/science/article/pii/S0925400501009935

[79] D. Resnik, D. Vrtacnik, M. Mozek, B. Pecar, and S. Amon, "Experimental study of heat-treated thin film Ti/Pt heater and temperature sensor properties on a si microfluidic platform," *Journal of Micromechanics and Microengineering*, vol. 21, no. 2, p. 025025, 2011. [Online]. Available: http://iopscience.iop.org/0960-1317/21/2/025025

[80] J. Martinez-Quijada, S. Caverhill-Godkewitsch, M. Reynolds, L. Gutierrez-Rivera, R. Johnstone, D. Elliott, D. Sameoto, and C. Backhouse, "Fabrication and characterization of aluminum thin film heaters and temperature sensors on a photopolymer for lab-on-chip systems," *Sensors and Actuators A: Physical*, vol. 193, pp. 170–181, Apr. 2013. [Online]. Available: http://www.sciencedirect.com/science/article/pii/S0924424713000484

[81] T.-M. Hsieh, C.-H. Luo, F.-C. Huang, J.-H. Wang, L.-J. Chien, and G.-B. Lee, "Enhancement of thermal uniformity for a microthermal cycler and its application for polymerase chain reaction," *Sensors and Actuators B: Chemical*, vol. 130, no. 2, pp. 848–856, Mar. 2008. [Online]. Available: http://www.sciencedirect.com/science/article/pii/S0925400507008842

[82] T.-M. Hsieh, C.-H. Luo, J.-H. Wang, J.-L. Lin, K.-Y. Lien, and G.-B. Lee, "A two-dimensional, self-compensated, microthermal cycler for one-step reverse transcription polymerase chain reaction applications," *Microfluidics and Nanofluidics*, vol. 6, no. 6, pp. 797–809, Jun. 2009. [Online]. Available: http://link.springer.com.login.ezproxy.library.ualberta.ca/article/10.1007/s10404-008-0353-x

[83] J.-H. Wang, L.-J. Chien, T.-M. Hsieh, C.-H. Luo, W.-P. Chou, P.-H. Chen, P.-J. Chen, D.-S. Lee, and G.-B. Lee, "A miniaturized quantitative polymerase chain reaction system for DNA amplification and detection," *Sensors and Actuators B: Chemical*, vol. 141, no. 1, pp. 329–337, Aug. 2009. [Online]. Available: http://www.sciencedirect.com/science/article/pii/S0925400509005103

[84] M. Griep, C. Kotera, R. Nelson, and H. Viljoen, "Kinetics of the DNA polymerase pyrococcus kodakaraensis," *Chemical Engineering Science*, vol. 61, no. 12, pp. 3885–3892, Jun. 2006. [Online]. Available: http://linkinghub.elsevier.com/retrieve/pii/S000925090600011X

[85] C. T. Wittwer, G. C. Fillmore, and D. J. Garling, "Minimizing the time required for DNA amplification by efficient heat transfer to small samples," *Analytical biochemistry*, vol. 186, no. 2, pp. 328–331, May 1990, PMID: 2363506.

[86] C. T. Wittwer, G. B. Reed, and K. M. Ririe, "Rapid cycle DNA amplification," in *The Polymerase Chain Reaction*. Springer-Verlag, 1994, pp. 174–181.

[87] P. Neuzil, "Ultra fast miniaturized real-time PCR: 40 cycles in less than six minutes," *Nucleic Acids Research*, vol. 34, no. 11, pp. e77–e77, Jun. 2006. [Online]. Available: http://www.nar.oxfordjournals.org/cgi/doi/10.1093/nar/gkl416

[88] H. Terazono, H. Takei, A. Hattori, and K. Yasuda, "Development of a high-speed real-time polymerase chain reaction system using a circulating water-based rapid heat-exchange," *Japanese Journal of Applied Physics*, vol. 49, no. 6, p. 06GM05, Jun. 2010. [Online]. Available: http://jjap.jsap.jp/link?JJAP/49/06GM05/

[89] B. Selva, P. Mary, and M.-C. Jullien, "Integration of a uniform and rapid heating source into microfluidic systems," *Microfluidics and Nanofluidics*, vol. 8, no. 6, pp. 755–765, Oct. 2009. [Online]. Available: http://www.springerlink.com/index/10.1007/s10404-009-0505-7

[90] J. Fontes, "Temperature sensors," in *Sensor Technology Handbook*, J. S. Wilson, Ed. Oxford: Elsevier Inc., 2005, pp. 531–562.

[91] J. Martinez-Quijada, "Design and microfabrication of robust and highly integrated thermal lab-on-a-chip polymeric systems for genetic diagnosis," Ph.D. dissertation, 2014. [Online]. Available: http://era.library.ualberta.ca/public/datastream/get/uuid:6a735f29-610f-48ee-9de8-0c5c954b669a/DS1/JMQ%20Thesis%20-%20FINAL.pdf

[92] M. Reynolds, "Development of KMPR-based microfluidic structures for use in LOC systems," Master's thesis, University of Alberta, 2014. [Online]. Available: https://era.library.ualberta.ca/public/view/item/uuid:c6e2168e-bda4-47dd-9759-d7b16f296bf6/DS1/Reynolds_Matthew_Spring_2014.pdf

[93] M. Reynolds, A. Elias, D. G Elliott, C. Backhouse, and D. Sameoto, "Variation of thermal and mechanical properties of KMPR due to processing parameters," *Journal of Micromechanics and Microengineering*, vol. 22, no. 12, p. 125023, Dec. 2012. [Online]. Available: http://iopscience.iop.org/0960-1317/22/12/125023

[94] F. Li, R. Misra, Z. Fang, Y. Wu, P. Schiffer, Q. Zhang, S. Tadigadapa, and S. Datta, "Magnetoelectric Flexural Gate Transistor With Nanotesla Sensitivity," *Journal of Microelectromechanical Systems*, vol. 22, no. 1, pp. 71–79, Feb. 2013.

[95] C. for Disease Control and Prevention, "CDC - Malaria - Diagnosis & Treatment (United States) - Diagnosis (U.S.)." [Online]. Available: http://www.cdc.gov/malaria/diagnosis_treatment/diagnosis.html

[96] COMSOL, "Integrated Square-Shaped Spiral Inductor." [Online]. Available: http://www.comsol.com/model/integrated-square-shaped-spiral-inductor-129

[97] "Plotting Spatial Derivatives of the Magnetic Field." [Online]. Available: http://www.comsol.com/blogs/plotting-spatial-derivatives-magnetic-field/

APPENDIX A

COMSOL VALIDATION

This report describes a simulation experiment done to validate the results obtained using the COMSOL Multiphysics, Magnetic and Electric Fields interface against an accepted analytical model. The model in question is a single current carrying wire in free space, and the quantities of interest are the magnetic field and gradient, which can be used to calculate the force on a magnetizable spherical object in the field. It was found that the COMSOL force term results agree with the idealized analytical solution within a percent difference of 5%. It is also noted that while a small value for air conductivity must be given in order to make this physics interface work, there appears to be little effect on the results in this particular case. With that said, the issue is interesting and results of more complicated simulations using this interface should be examined carefully and tested against analytical solutions whenever possible.

A.1 Motivation

The purpose of this report is to demonstrate the validity of simulations done in COMSOL's Magnetic and Electric Fields interface by comparing results of a simple simulation to those of an analytical model. The motivation for doing this is that it is important to evaluate whether the COMSOL results are around what is expected from well-known analytical solutions. If the results are accurate according to these well known solutions, then it can be expected that the results for more complicated design scenarios using the same type of simulation are satisfactorily accurate for our purposes.

A.2 Design of Experiment

The simple case of determining the magnetic field, gradients and forces on a magnetizable, spherical object due to a single current-carrying wire is explored numerically in two ways. First, by putting

realistic numbers to the general 2D analytical solution of this case we can come up with an accepted baseline. Second, COMSOL is used to model the same system in three dimensions. The Magnetic and Electric Fields interface is employed to model the system as this is the physics interface suggested by COMSOL documentation. This interface is used for further, more complicated electromagnet designs, and thus is the focus of the characterization.

A.2.1 Objective

The objective of this work is to determine the validity of COMSOL simulations done with the Magnetic and Electric Fields physics interface by determining the how closely the COMSOL results in 3D match those of the well-known analytical 2D case of a single, current-carrying wire in air. The analytical model is, of course, also an approximation.

A.2.2 Factors, Levels, Response

A simple measure (response) of the performance of this physics interface is to measure/calculate the force on a small, magnetizable spherical object at some distance from the current-carrying wire. This is a representation of the magnetic bead that will be used in Lab-on-a-chip (LOC) sample preparation (SP) work. The force terms in three dimensions can be generally described as follows:

$$\vec{F}_x = \frac{V\chi_v}{\mu_0}\left[\left(B_x\frac{\partial B_x}{\partial_x} + B_y\frac{\partial B_x}{\partial_y} + B_z\frac{\partial B_x}{\partial_z}\right)\vec{a}_x\right]$$
$$\vec{F}_y = \frac{V\chi_v}{\mu_0}\left[\left(B_x\frac{\partial B_y}{\partial_x} + B_y\frac{\partial B_y}{\partial_y} + B_z\frac{\partial B_y}{\partial_z}\right)\vec{a}_y\right]$$
$$\vec{F}_z = \frac{V\chi_v}{\mu_0}\left[\left(B_x\frac{\partial B_z}{\partial_x} + B_y\frac{\partial B_z}{\partial_y} + B_z\frac{\partial B_z}{\partial_z}\right)\vec{a}_y\right]$$

The magnitude of these three terms can be summarized as:

$$\vec{F_m} = \frac{V\chi_v}{\mu_0}(\vec{B}\cdot\nabla)\vec{B}$$

Where V is the volume of a magnetizable sphere, χ_v is the volume magnetic susceptibility of that sphere, μ_0 is the permeability of free space, and $\vec{B}$ is the magnetic flux density in the region of interest. The force terms listed above are useful response quantities to measure, since they take into

account both field and gradient values.

It has been noted that the non-zero conductivity of air required by this physics interface can cause variations in the results. Thus, this parameter should be included in the experiment as a factor of interest. The levels chosen for the air conductivity factor are 1, 10 and $100\,\mathrm{S\,m^{-1}}$.

A.2.3 Experimental Design

The magnetic field due to a current-carrying wire is solved analytically and relevant numbers are put to the variables in MATLAB. See appendix C for the code associated with the derivations and numerical analysis. Table A.1 lists important model parameters.

Table A.1: Important model parameters.

Parameter	**Value**
Current, I	$1\,\mathrm{A}$
Permeability of free space, μ_0	$4\pi \times 10^{-7}\,\mathrm{m\,kg\,s^{-2}\,A^{-2}}$
Magnetic bead radius, r	$0.5\,\mu\mathrm{m}$
Volume magnetic susceptibility of magnetic bead, χ_v	$0.5\,[\text{dimensionless}]$

It is defined that the current-carrying wire is along the z-axis, the y-axis is referred to as being the superior-inferior axis. The force values are "measured" along a line parallel to the x-axis and (arbitrarily) $100\,\mu\mathrm{m}$ above (along y-axis) the current-carrying wire. Plots for a subset of the fields, gradients and forces along the line of interest are shown. Peak values of the force terms are listed.

A.3 Results

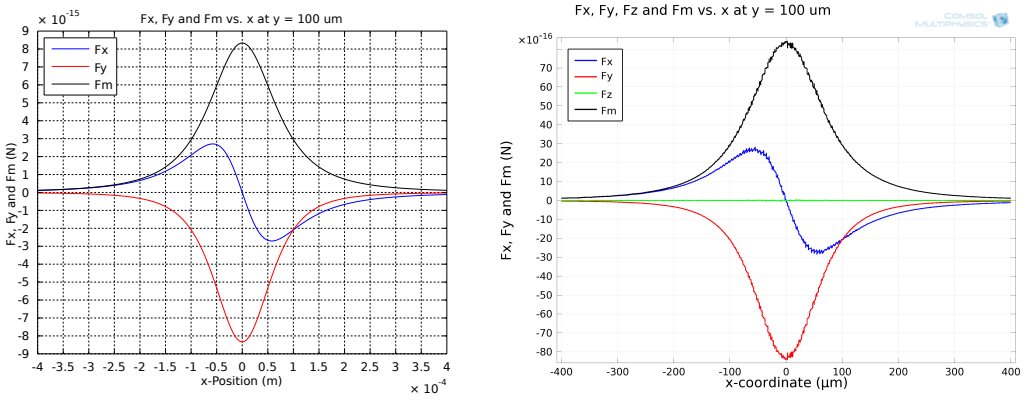

(a) (b)

Figure A.1: $\vec{F}_x$, $\vec{F}_y$, $\vec{F}_z$ and $\vec{F}_m$ along x at a height of $y = 100\,\mu\text{m}$ above the current-carrying wire. (a) Analytical solution, (b) COMSOL results. Axes are identical between (a) and (b).

Table A.2: Percent difference between COMSOL simulation peak values and analytical solution. See table A.3 in section Appendix A.6 for the actual values.

Air Conductivity (S m^{-1})	$\vec{F}_x$	$\vec{F}_y$	$\vec{F}_m$
$\sigma_{air} = 1\,\text{S m}^{-1}$	4.49%	1.08%	1.10%
$\sigma_{air} = 10\,\text{S m}^{-1}$	4.34%	1.14%	1.15%
$\sigma_{air} = 100\,\text{S m}^{-1}$	4.40%	1.11%	1.12%
$\sigma_{air} = 1000\,\text{S m}^{-1}$	4.39%	1.08%	1.09%

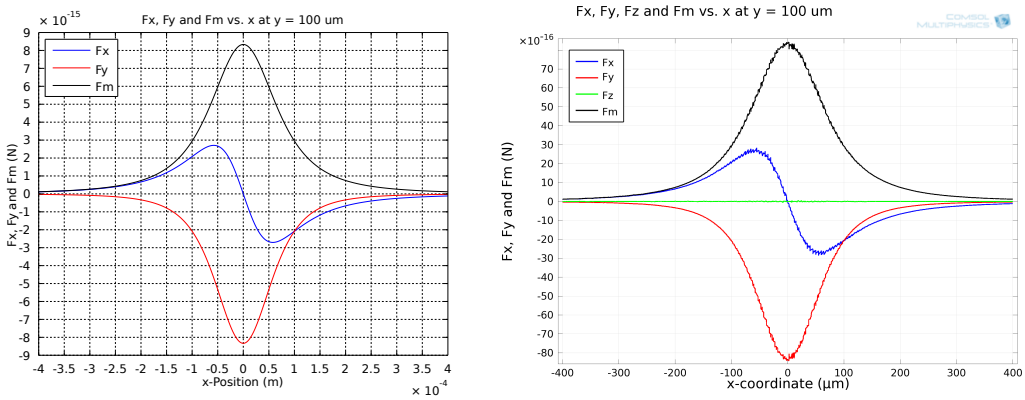

(a) Analytical Solution

(b) Air Conductivity = 1 S/m

(c) Air Conductivity = 10 S/m

(d) Air Conductivity = 100 S/m

Figure A.2: $\vec{F}_x$**,** $\vec{F}_y$**,** $\vec{F}_z$ and $\vec{F}_m$ along x at a height of $y = 100\,\mu\text{m}$ above the current-carrying wire. (a) Analytical solution, (b) $\sigma_{air} = 1\,\text{S}\,\text{m}^{-1}$, (c) $\sigma_{air} = 10\,\text{S}\,\text{m}^{-1}$, (d) $\sigma_{air} = 100\,\text{S}\,\text{m}^{-1}$.

A.4 Discussion

As is clearly demonstrated by the plots of the magnetic field, gradients (see appendix A.6) and force terms (figure A.1), the COMSOL simulations using the Magnetic and Electric Fields interface match very closely with the analytical solution (less than 5% difference from analytical). These results validate the interface used for further, more complicated simulations, used to optimize electromagnet designs for doing on-chip magnetic bead-based sample preparation. More specifically, these results support the use of this physics interface with some recommendations:

1. The conductivity of air is of value $1\,\mathrm{S\,m^{-1}}$ or lower.

2. The air box surrounding the electromagnet large in comparison to the electromagnet dimensions. In this case, it was approximately three orders of magnitude.

3. The relative tolerance (in error) set to 0.001.

4. The solver used is the FGMRES iterative solver, default settings. The FGMRES (Flexible Generalized Minimum RESidual) iterative method is the most robust (and computationally intensive) method of the iterative solvers.

One secondary issue that can be troubling with this particular physics interface is the fact that the user is required to give air a non-zero value for conductivity. This is established in COMSOL tutorial documentation [96]: "Setting the conductivity to zero in the air would lead to a numerically singular problem. You can avoid this problem by using a small non-zero value. As 1 S/m is much less than the electric conductivity in the inductor, the fields will only be marginally affected."

In this set of simulation experiments there is very little difference in the results due to changes in the conductivity of air, as shown by the results in table A.3 and the plots in figure A.2. However, it should be noted that some disturbing changes have been seen in other simulations using this interface when the conductivity of air was increased to $1000\,\mathrm{S\,m^{-1}}$. An example of this is shown in figure A.5, in section A.6. It appears, then, that there is some interaction between the air box size relative to the magnetic field source (current-carrying wire) and the simulated result. Topology of the magnetic source may play a role as well.

A.5 Conclusion

The Magnetic and Electric Fields interface in COMSOL Multiphysics simulation software was validated against a well-known analytical model of a current-carrying wire in free space. While the COMSOL results match very closely to the analytical values (within 5% for $\vec{F}_x$ and about 1% for $\vec{F}_m$), the issue of giving air a non-zero value for conductivity is an issue that should be watched carefully, especially since it has been previously noted to cause issues in simulated results before.

A.6 Additional Figures and Tables

Table A.3: $\vec{F}_x$, $\vec{F}_y$, $\vec{F}_z$ and $\vec{F}_m$ peak values on a line in x at a height of $y = 100\,\mu\text{m}$ above the current-carrying wire for all solution cases. Note the lack of a substantial difference in values among the difference σ_{air} values.

Force Values for Each Case	$\vec{F}_x\,(\text{N})$	$\vec{F}_y\,(\text{N})$	$\vec{F}_z\,(\text{N})$	$\vec{F}_m\,(\text{N})$
Analytical Solution	2.71×10^{-15}	-8.333×10^{-15}	N/A	8.333×10^{-15}
COMSOL $\sigma_{air} = 1\,\text{S}\,\text{m}^{-1}$	2.830×10^{-15}	-8.424×10^{-15}	5.011×10^{-17}	8.425×10^{-15}
COMSOL $\sigma_{air} = 10\,\text{S}\,\text{m}^{-1}$	2.826×10^{-15}	-8.429×10^{-15}	4.834×10^{-17}	8.430×10^{-15}
COMSOL $\sigma_{air} = 100\,\text{S}\,\text{m}^{-1}$	2.828×10^{-15}	-8.426×10^{-15}	4.882×10^{-17}	8.427×10^{-15}
COMSOL $\sigma_{air} = 1000\,\text{S}\,\text{m}^{-1}$	2.831×10^{-15}	-8.424×10^{-15}	5.011×10^{-17}	8.425×10^{-15}

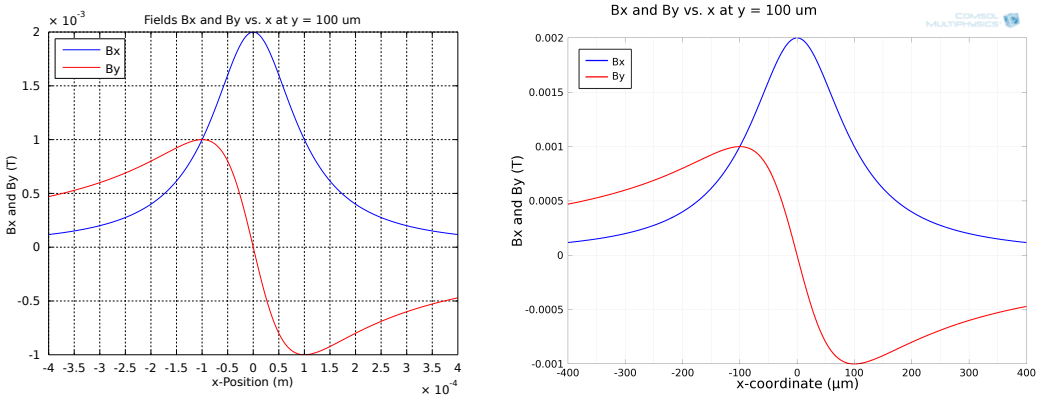

(a) (b)

Figure A.3: $\vec{B}_x$ and $\vec{B}_y$ along x at a height of $y = 100\,\mu\text{m}$ above the current-carrying wire. (a) Analytical solution, (b) COMSOL results.

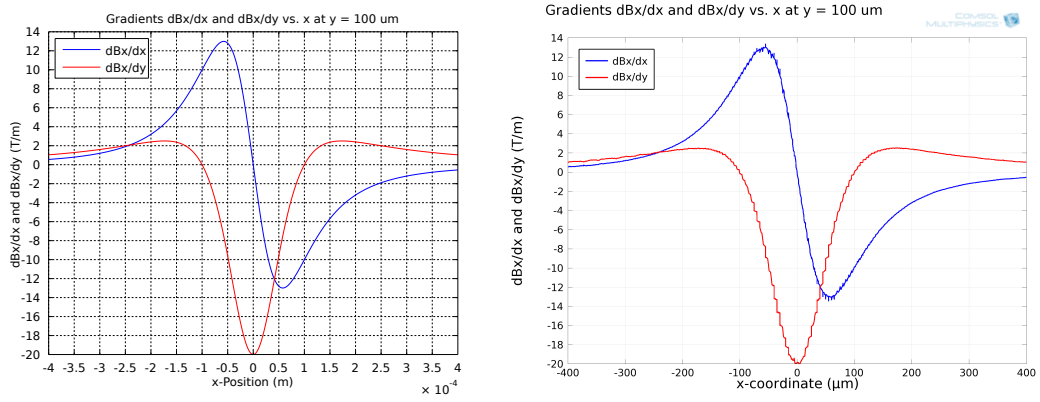

(a) (b)

Figure A.4: $\frac{\partial B_x}{\partial_x}$ and $\frac{\partial B_x}{\partial_y}$ along x at a height of $y = 100\,\mu\text{m}$ above the current-carrying wire. (a) Analytical solution, (b) COMSOL results.

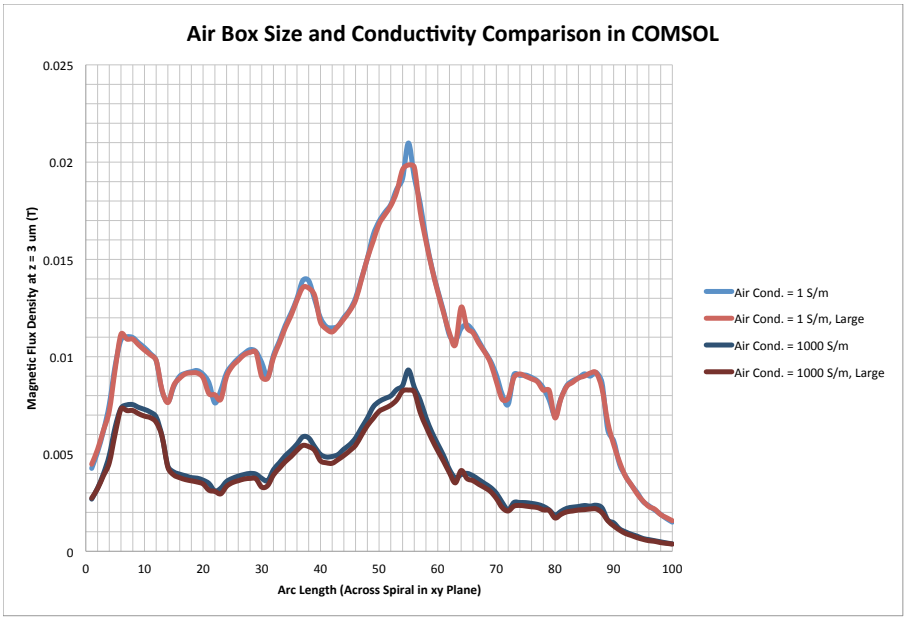

Figure A.5: Comparison of the effect of changing the air box size and conductivity value in a COMSOL simulation (Magnetic and Electric Fields interface) of a square spiral inductor. Note the significant difference in simulated field with respect to air conductivity.

APPENDIX B

COMSOL MODELING

This appendix summarizes the key modeling concepts for the electromagnetic simulations that made up chapter 3 of this work. COMSOL Version 4.3a was used for the simulations in this thesis. The organization of the "2D" and "3D" sections of this chapter matches the tree in COMSOL's Model Builder (the pane on the left-hand side of COMSOL's graphical user interface). For more information, please refer to COMSOL's extensive documentation (user guides, example models, community resources and message boards) available on their website.

B.1 2D Simulations

Some geometries of interest lend themselves to 2D modeling. A serpentine electromagnet, for example, can be modeled as a cross section as long as the designer is considering the quantities far from the edges of the electromagnet that contain the U-turns of the serpentine.

B.1.1 Global Definitions

The PCB serpentine electromagnet will be used for the purpose of communicating modeling parameters in this section.

B.1.1.1 Parameters

Parameters for the PCB serpentine are presented in table B.1. It is useful to note that the designer can (and should) use equations in COMSOL's parameter entry table to avoid arithmetic errors. Total values are included in the descriptions as a check.

Table B.1: Parameters for the PCB serpentine simulation (2D).

Parameter	Value	Description
w_trace	177.8 µm	1 Oz Cu min width.
h_trace	35.56 µm	1 Oz Cu thickness.
w_lam	67 mm	Credit card width.
l_lam	60 mm	Credit card length.
h_lam	0.5 mm	Minimum laminate thickness for 1 Oz Cu.
h_uv	h_trace + 14 µm	49.56 mm - Thickness of UV-cure acrylic.
r_air	0.5 m	Radius of infinite elements domain.
I	1 A	Current in PCB trace.
J	I / (w_trace*h_trace)	1.58×10^9 A m^{-2} - Current density in PCB trace.

B.1.2 Model

The "model" portion of the COMSOL simulation is made up of the definitions, geometry, materials, and the physics interfaces of interest.

B.1.2.1 Definitions

For 2D electromagnetic simulations, an *Infinite Elements Domain* domain must be defined to model the unbounded air domain that surrounds the geometry of interest (the serpentine electromagnet in the PCB). This *Infinite Elements Domain* must be defined in this section, but it cannot be added until after the geometry is constructed.

B.1.2.2 Geometry

In this 2D simulation, the designer models the cross section of the serpentine traces. COMSOL's geometry builder offers a simple interface to construct the geometry of interest. In this case, the geometry is made up of the components listed in table B.1. In addition to the metal traces, the PCB platform and the UV-cure acrylic regions, an air volume must be constructed around the PCB.

In addition to the air volume that surrounds the PCB, an artificial boundary must be constructed as an *Infinite Elements Domain* as described in section B.1.2.1 above. This boundary can be constructed as an additional circular region around the air domain, and can also be made up of air as the material. Once constructed as a geometry, the domain can be selected and defined as an *Infinite Elements Domain* in the Definitions header of the Model Builder pane.

B.1.2.3 Materials

Materials can be selected from a pre-installed COMSOL library. The designer can also construct their own materials to use in their models. Once materials are chosen for the model, the user then selects which domains are associated with each of those materials.

In the case of the PCB electromagnet, pre-installed materials were used, including: *Air*, *FR4 (Circuit Board)*, *Copper*, *Water-liquid*, and *Acrylic plastic*.

B.1.2.4 Physics Interface - Magnetic Fields (mf)

Once the geometry is constructed and the materials are assigned to the applicable domains, the user adds physics interfaces to perform the calculations of interest. In the 2D case, the designer can use the *Magnetic Fields (mf)* interface. Please refer to the AC/DC Module User's Guide for details on how to correctly apply this physics interface.

One way to implement a flow of electrical current in this 2D simulation is to add *External Current Densities* to the *mf* physics interface. Similar to selecting domains for materials, the designer adds the *External Current Densities* node and then selects the domain on which the physics should be applied. The designer then enters a value for the current density to be applied to that domain, and the direction in which it's applied. Since this is a 2D cross-sectional simulation, the designer would apply the current density into the screen (typically this will be automatically defined as the z-direction). By applying equal-in-magnitude but opposite-in-sign current densities in adjacent traces, a 2D serpentine electromagnet including current is completed.

B.1.2.5 Mesh

COMSOL typically meshes geometries efficiently when left to perform this step automatically. The designer can specify different densities of elements for different domains if that is desirable, or even further the designer can manually mesh all regions. In general, if the constructed geometry has a wide range of dimensions (e.g., very small dimensions for the PCB surrounded by large dimensions associated with the air boundary) then the designer should specify that the smaller domains should be constructed with fine meshes to ensure convergence of the simulation. The order of meshing options from most fine to most coarse are: Extremely fine, Extra Fine, Finer, Fine, Normal, Coarse, Coarser, Extra Coarse and Extremely Coarse.

B.1.3 Study

The Study header of the model builder allows the user to run the simulation and tweak calculation parameters if necessary. Default values for performing the study are sufficient.

B.1.4 Results

Various data sets and plots can be used to probe the results and generate answers to the designer's questions. As discussed in this work, the quantities of interest here were the magnetic field and the magnetic field gradients, which contribute to the force terms defined in section 3.4.2.

B.2 3D Simulations

If a geometry of interest cannot be modeled in 2D, then a 3D model can be constructed. The spiral electromagnet that was implemented in L12 is an example of one such topology, and will be used as the example in this section on 3D modeling. There are a few key differences between modeling magnetic fields in 2D versus 3D, and those differences are highlighted in this section.

B.2.1 Global Definitions

B.2.1.1 Parameters

Parameters for the CMOS spiral are presented in table B.2.

Table B.2: Parameters for the planar spiral simulation (3D).

Parameter	Value	Description
W	15 µm	CMOS wire width.
H	1 µm	CMOS wire thickness.
J0	$2 \times 10^{10}\,\mathrm{A\,m^{-2}}$	Current density.
p	1.8 µm	Spacing between CMOS wires.
Rbead	0.5 µm	Magnetic bead radius.

B.2.2 Model

B.2.2.1 Geometry

The easiest way to construct 3D planar topologies in COMSOL is to design them first in 2D *Work Planes* and then apply *Extrusions* to implement the thickness of the component. Similar to the 2D modeling case, an air volume surrounding the current-carrying conductors is necessary. Since the current must be applied to an external boundary, the air surrounding the conductor is most easily implemented as a box. This allows current densities to be applied to the external boundaries of the spiral leads.

B.2.2.2 Materials

As in the 2D model, pre-installed materials were used. Only two were necessary to estimate the magnetic performance of the module: *Air*, and *Aluminum*.

B.2.2.3 Physics Interface - Magnetic and Electric Fields (mef)

Similar to the 2D model, *External Current Density* nodes are added to the *mef* physics to apply the current to the electromagnet leads. Here, however, is where this 3D model makes a significant departure from the 2D case. A brief explanation of why the physics is performed in this manner is described here; for more information, please refer to the AC/DC Module User's Guide and [97] for details on how to correctly apply this physics interface in the most recent version of COMSOL.

In COMSOL, computing and plotting the gradients of magnetic fields in 3D electromagnetic simulations is not immediately straightforward. COMSOL uses vector elements to calculate magnetic fields induced by currents specified by the user in the model via the *mef* interface. The magnetic vector potential $\mathbf{A}$ is calculated in these instances, but COMSOL is only able to differentiate this quantity once in the *mef* physics interface. Since the magnetic flux density is defined as $\mathbf{B} = \nabla \times \mathbf{A}$, then the first differentiation of $\mathbf{A}$ is used in this initial computation of $\mathbf{B}$. To calculate the gradients of the magnetic flux density, $\mathbf{B}$ must be mapped to additional variables using Lagrange elements via the *Coefficient Form PDE* physics interface.

B.2.2.4 Physics Interface - Coefficient Form PDEs

Three partial differential equation (*PDE*) nodes should be added as physics interfaces to the model. The user can then set the *Initial Values* variable *u* to one of the magnetic flux density values that will be calculated by the *mef* interface (*i.e.*, *mef.Bx*, *mef.By*, or *mef.Bz*). This maps the first derivative of the vector element (derivative of the magnetic vector potential **A**) to a Lagrange element which can then be differentiated further.

The above is repeated twice more to map *mef.By* to *u*2 and *mef.Bz* to *u*3, and the user is left with four physics interfaces as shown in figure B.1.

B.2.3 Study - *mef*

Since the *Coefficient Form PDEs* use results from the *mef* physics interface as inputs, two studies must be performed to generate all the necessary results. The first study solves the *mef* physics. To enable this computational order, the user must disable the *PDE* interfaces for the first *Study* as shown in figure B.2.

B.2.4 Study - *PDEs*

The second study performs the mapping and differentiation to extract magnetic flux gradient values. In this case, the user will disable the *mef* interface and solve the three *PDE* nodes as shown in figure B.3.

B.2.5 Results

Again similar to the 2D modeling case, various data sets and plots can be used to probe the results and generate answers to the designer's questions. The quantities of interest here were the magnetic field and the magnetic field gradients, which contribute to the force terms defined in section 3.4.2.

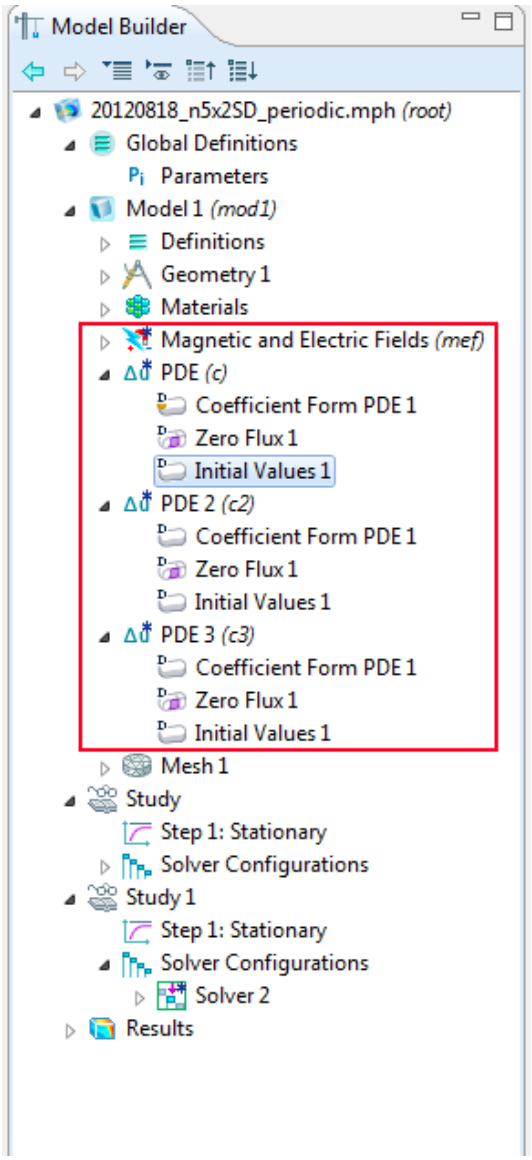

Figure B.1: COMSOL physics interfaces for performing 3D electromagnetic simulations.

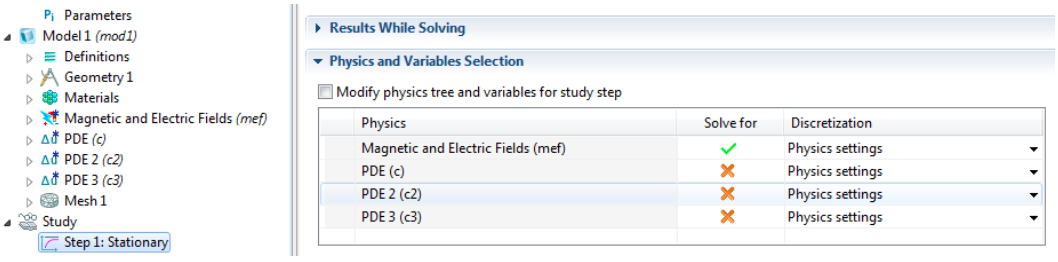

Figure B.2: The first of two studies necessary to generate the magnetic flux density components of the force term equations. The *PDE* physics interfaces are disabled since they require results from the *mef* physics interface as inputs.

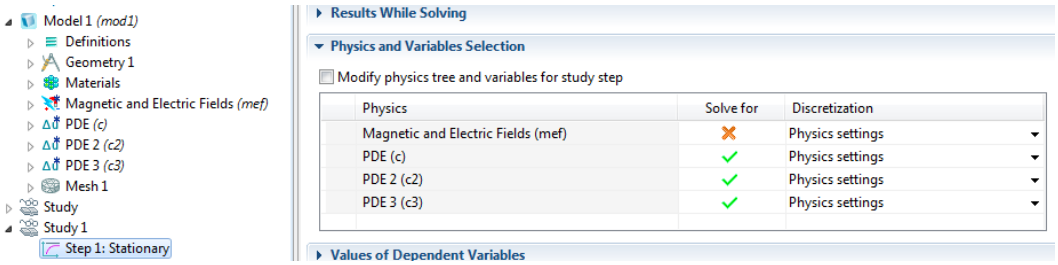

Figure B.3: The second of two studies necessary to generate the magnetic flux density components of the force term equations. The *mef* physics interface is disabled since it should have been performed prior to this step. Results from the *mef* physics are used as inputs to the *PDE* nodes.

B.3 Force Equations

The force equations presented in section 3.4.2 are implemented in 2D and 3D slightly differently due to the difference in simulation process as described above.

B.3.1 2D Force Equations

The following equations are entered in COMSOL result probes (exactly as they appear here) to generate plots.

```
Fx = (5.2360e-019[m^3]*0.5/(pi*4e-7[m*kg*s^(-2)*A^(-2)]))*(Azy*
     Azyx+(-Azx)*(Azyy))
Fy = (5.2360e-019[m^3]*0.5/(pi*4e-7[m*kg*s^(-2)*A^(-2)]))*((-Azx)
     *(-Azxy)+Azy*(-Azxx))
Fm = sqrt(((5.2360e-019[m^3]*0.5/(pi*4e-7[m*kg*s^(-2)*A^(-2)]))*(
     Azy*Azyx+(-Azx)*(Azyy)))^2+((5.2360e-019[m^3]*0.5/(pi*4e-7[m*
     kg*s^(-2)*A^(-2)]))*((-Azx)*(-Azxy)+Azy*(-Azxx)))^2)
```

Where:

Azy = $\vec{B}_x$, Azyx = $\frac{\partial B_x}{\partial_x}$, Azyy = $\frac{\partial B_x}{\partial_y}$

-Azx = $\vec{B}_y$, -Azxy = $\frac{\partial B_y}{\partial_y}$, -Azxx = $\frac{\partial B_y}{\partial_x}$

B.3.2 3D Force Equations

The following equations are entered in COMSOL result probes (exactly as they appear here) to generate plots.

```
Fx = (5.2360e-019[m^3]*0.5/(pi*4e-7[m*kg*s^(-2)*A^(-2)]))*(u*ux +
    u2*uy + u3*uz)[T^2/m]
Fy = (5.2360e-019[m^3]*0.5/(pi*4e-7[m*kg*s^(-2)*A^(-2)]))*(u*u2x +
     u2*u2y + u3*u2z)[T^2/m]
Fz = (5.2360e-019[m^3]*0.5/(pi*4e-7[m*kg*s^(-2)*A^(-2)]))*(u*u3x +
     u2*u3y + u3*u3z)[T^2/m]
Fm = (5.2360e-019[m^3]*0.5/(pi*4e-7[m*kg*s^(-2)*A^(-2)]))*sqrt((u*
    ux + u2*uy + u3*uz)^2+(u*u2x + u2*u2y + u3*u2z)^2+(u*u3x + u2*
    u3y + u3*u3z)^2)[T^2/m]
```

Where:

u = $\vec{B}_x$

u2 = $\vec{B}_y$

u3 = $\vec{B}_z$

APPENDIX C

MATLAB CODE

```
% Validation of COMSOL simulations by comparison with analytical
    model.
% Single, long, current carrying wire produces the magnetic field
    and
% gradients. Arbitrary values will be defined and used. Fx, Fy and
     Fmag
% will be calculated. The model will be implemented in 2D and 3D
    in COMSOL
% and compared to the results here. The wire will be made as thin
    as
% possible in COMSOL to make the results comparable. Make location
     of
% interest (bead location radius) 3 orders of magnitude greater
    than the
% wire dimension. Here, the location of interest is a cutline
    along X,
% 100 um above the wire (in Y).

% Equations are derived in  "b_field_symbolic.m"

clear all;
clc;
```

```
% Constants and parameters
[X,Y] = meshgrid(-0.0004:0.0000001:0.0004, 100e-6);
I = -1;                    % Current is 1 [A]
u0 = pi*4e-7;              % Permeability of free space
V = 4/3*pi*(0.5e-6)^3;  % Volume of 1 um spherical bead
Xv = 0.5;                % Magnetic susceptibility of iron (III) oxide

% Magnetic Fields Bx and By
Bx = -1/2*u0*I/pi./(X.^2+Y.^2).*Y;
By = 1/2*u0*I/pi./(X.^2+Y.^2).*X;

% Gradients of Bx and By wrt x and y
dBx_dx = u0*I/pi./(X.^2+Y.^2).^2.*Y.*X;
dBx_dy = -1/2*u0*I.*(X.^2-Y.^2)./pi./(X.^2+Y.^2).^2;

dBy_dx = -1/2*u0*I.*(X.^2-Y.^2)./pi./(X.^2+Y.^2).^2;
dBy_dy = -u0*I/pi./(X.^2+Y.^2).^2.*X.*Y;

% Forces in x and y due to the magnetic field and gradients
Fx = (V*Xv/u0).*(Bx.*dBx_dx + By.*dBx_dy);
Fy = (V*Xv/u0).*(By.*dBy_dy + Bx.*dBy_dx);

% Magnitude of force on magnetic bead
Fm = sqrt(Fx.^2 + Fy.^2);

% Plots
figure(1);
%subplot(2,2,1)
plot(X,Bx,'b'), xlabel('x-Position (m)'), ylabel('Bx and By (T)'),
    title('Magnetic fields Bx and By vs. x-position at a y-
```

```
    location␣of␣100␣um'), hold on;
plot(X,By,'r'), legend('Bx','By',2), grid on, axis([-4e-4 4e-4
    -0.001 0.002]), set(gca,'XTick',-4e-4:50e-6:4e-4,'YTick'
    ,-0.001:0.0005:0.002), hold off;

figure(2);
%subplot(2,2,2)
plot(X,dBx_dx,'b'), xlabel('x-Position␣(m)'), ylabel('dBx/dx␣and␣
    dBx/dy␣(T/m)'), title('Magnetic␣field␣gradients␣dBx/dx␣and␣dBx
    /dy␣vs.␣x-position␣at␣a␣y-location␣of␣100␣um'), hold on;
plot(X,dBx_dy,'r'), legend('dBx/dx','dBx/dy',2), grid on, axis([-4
    e-4 4e-4 -20 14]), set(gca,'XTick',-4e-4:50e-6:4e-4,'YTick'
    ,-20:2:14), hold off;

figure(3);
%subplot(2,2,3)
plot(X,dBy_dy,'b'), xlabel('x-Position␣(m)'), ylabel('dBy/dy␣and␣
    dBy/dx␣(T/m)'), title('Magnetic␣field␣gradients␣dBy/dy␣and␣dBy
    /dx␣vs.␣x-position␣at␣a␣y-location␣of␣100␣um'), hold on;
plot(X,dBy_dx,'r'), legend('dBy/dy','dBy/dx',2), grid on, axis([-4
    e-4 4e-4 -20 14]), set(gca,'XTick',-4e-4:50e-6:4e-4,'YTick'
    ,-20:2:14), hold off;

figure(4);
%subplot(2,2,4)
plot(X,Fx,'b'), xlabel('x-Position␣(m)'), ylabel('Fx,␣Fy␣and␣Fm␣(N
    )'), title('Fx,␣Fy␣and␣Fm␣vs.␣x-position␣at␣a␣y-location␣of␣
    100␣um'), hold on;
plot(X,Fy,'r'), plot(X,Fm,'k'), legend('Fx','Fy','Fm',2), grid on,
     axis([-4e-4 4e-4 -90E-16 90E-16]), set(gca,'XTick',-4e-4:50e
    -6:4e-4,'YTick',-90E-16:10E-16:90E-16), hold off;
```